The role of heteroatoms during graphitisation: First principle calculations

Submitted by

Jean-Joseph Adjizian

to the University of Sussex
as a thesis for the degree of
Doctor of Philosophy in Chemistry
in the School of Life Sciences

September 2012

I certify that all the material in this thesis which is not my own work has been identified and that no material is included for which a degree has previously been conferred on me.

Acknowledgements

First, I would like to thank EDF Energy for funding my DPhil.

I also would like to thank my supervisor Prof. Malcolm Heggie for his generosity and his time. He helped me throughout these four years and I would not be where I am now without him.

A special thanks to Dr Christopher Latham for answering every question I asked during all these years and also for correcting my Scottish. Thanks to all former members of the Heggie group: Gemma, Jens and Calvin, but also to current members of the group James, Glen, Tom for the good chats at coffee time. Many thanks to the AIMPRO community and particularly Chris Ewels, Jon Goss and Patrick Briddon.

Je voudrais maintenant remercier une personne qui m'est très chère, et sans qui tout cela ne serait arrivé, mon père, Jean-Claude. Il a su me transmettre sa détermination et son envie au fur et à mesure de mes années passées en Ecosse et en Angleterre. Je dedie aussi ma thèse à ma maman, Laurence, qui j'éspère garde un oeil sur moi de là où elle est. Merci aussi à mes soeurs, Mélanie et Elodie, qui m'ont toujours considerées comme le petit prince. Merci aussi à mes amis d'enfance: Jean-Charles, Damien, Julien H., Jérome, Rémy et Clément mais aussi à mes amis très proche d'Ecosse: Julien P., Fluff, Stuart, Tim and Robert.

Je voudrais aussi remercier 'lovely sis' pour avoir pris le temps de m'aider à travers quelque uns de ces chapitres. Mes dernier remerciements vont en direction de Juman, avec qui mes quatre années à Brighton ont été merveilleuses et à qui je dois beaucoup.

Abstract

Graphite is widely used in modern industry, particularly in nuclear power generation in the UK. Understanding its formation is important for economical and safety reasons. The process to turn carbon materials into graphite by heat treatment is called the graphitisation process. It is the transformation of amorphous carbon, through a 2D turbostratic carbon intermediate, into 3D ordered layers of graphite. While many manufacturing processes have been established and many authors have contributed to understanding the important stages of graphitisation, the chemistry involved is not fully understood. It appears that impurities found in precursors can have a direct impact on the final graphite obtained.

The following work is an investigation of the role played by these heteroatoms during the graphitisation process. Using density functional theory (DFT), calculations on possible mechanisms involved in the graphitisation process are investigated. However, the initial stages contain complex and poorly defined chemistry, so we have chosen to avoid this area, even though factors such as the C:H:O ratios are clearly important. Instead, this work is focussed on the latter stages of graphitisation in order to better understand the ordering processes to obtain graphite (and their inverse disordering, insofar as it is relevant to radiation damage). In this way it is still possible to invoke standard concepts in the physics and chemistry of defects in crystals. If there is too much disorder, and the system is close to amorphous in nature, complexity would overwhelm the project. The descriptions of an amorphous material with a little extra order would be much more difficult than the descriptions of a crystal with some disorder. For this reason, we have focussed on the heteroatoms which endure until the later stages of graphitisation, boron and sulphur, and also on turbostratic graphite, where calculations of interlayer separation as a function of relative rotation of a layer

and of its neighbours are described.

We find for sulphur that it can open up folds in graphite, forming very stable sulphur decorated edges. In dislocation terms, this could be the beginning of the dissociation of a perfect prismatic edge dislocation. An edge dislocation is described as an added half plane. If the plane is a bilayer graphene terminating in a fold, the dislocation is perfect. If the plane is a single graphene the dislocation is 'partial'. Importantly two partial dislocations have lower elastic energy than the perfect, so dissociation is important in stabilising the structure.

For boron, we show how it can pin twist boundaries, preventing slip and suggest that radiation damage can achieve the same effect through vacancies. The mechanism does not appear to involve cross-linking bonds and provides a good explanation for the variations in C_{44} between different graphites and different methods of measurement. Furthermore, we show that B can aid in the removal of twist boundaries by pushing up their formation energy with respect to AB graphite.

List of publications and oral presentations

Publications

S F J Cox, J S Lord, I McKenzie, J-J Adjizian, M I Heggie, U A Jayasooriya, R Grinter and I D Reid, *Muonium chemistry and spin dynamics in sulphur, modelling interstitial hydrogen*, J. Phys.: Condens. Matter, 23, 315801 (2011)

J-J Adjizian, M I Heggie, C D Latham, S Oberg, P R Briddon, *Sulfur: A promoter for graphitization?*, Carbon, submitted (2013).

J-J Adjizian, M I Heggie, C D Latham, *The effect of boron on* C_{44}, in preparation.

Oral presentations

1–AIMPRO-08, Institut des materiaux Jean Rouxel, December 2008, Nantes, France.

2–British carbon group meeting, University of Manchester, April 2009, Manchester, UK.

3–Carbon-09, Casino de Biarritz, June 2009, Biarritz, France.

4–Diamond-09, University of Warwick, July 2009, Coventry, UK.

5–AIMPRO-10, University of Nottingham, April 2010, Nottingham, UK.

6–Carbon-10, Clemessy university, June 2010, Greenville, USA.

7–EDS-10, University of Sussex, September 2010, Brighton, UK.

8–NanoteC-10, Corpus Christi College Oxford, September2010, Oxford, UK.

9–NanoteC-11, Institut des materiaux Jean Rouxel, September 2011, Nantes, France.

9–INGSM-13, SGL group, September 2012, Augsburg, Germany.

Contents

Chapter 1

Introduction

1.1 Physical and chemical definition of Graphite

Carbon is an important element on earth and is recorded to be present in close to 20 million molecules, however, it is not necessarily the most abundant (~0.20% in weight). Its ability to form many compounds is due to its versatility to react with atoms such as nitrogen, sulphur, oxygen, chlorine and others. Carbon's properties have been studied for decades and it remains one of the main topics in research due to the discovery of new forms of carbon [1, 2]. In the modern periodic table, carbon is found in the second row, fourteenth column, and it has an atomic number of six. The main forms of carbon are ^{12}C (98.98%) and one of its isotope ^{13}C (1.1%), which gives an atomic weight of 12.0107 $g\,mol^{-1}$ [3]. Its $1s^2 2s^2 2p^2$ electron configuration means it can form four covalent bonds with its available electrons. Carbon atoms hybridise as sp^3, sp^2 and sp, thus it can form single, double and even triple bonds [4]. The different hybridisations give different carbon allotropes with diverse properties, with the best known being graphite and diamond. Some of the allotropic forms are described in table 1.1.

Spatial Dimension and coordination number (n)	Bond properties			Allotrope name
	Hybridisation	Length (Å)	Energy ($eV\,mol^{-1}$)	
3D (n=4)	sp^3-sp^3	1.54	15	Diamonds
3D (n=3)	sp^2-sp^2	1.41	25	Graphites
2D (n=3)	sp^2-sp^2	1.33	26.5	Fullerenes
1D (n=2)	sp-sp	1.21	35	Carbynes

Table 1.1: Classifications of different forms of carbon with their bond properties, taken from [5]

In the present work, we are focusing on the allotrope graphite. The word graphite means 'to write' in Greek. It is a soft black carbon based mineral naturally occurring, but it can also be manufactured. Studies with x-ray diffraction techniques, first from Hull (1917) and then Bernal (1924), indicated that the normal structure of graphite is hexagonal [6, 7]. In graphite, one of the 2*s* electrons hybridises with two of the 2*p* electrons to give three sp^2 orbitals at 120° to each other in a plane, with the remaining orbital having a p_z configuration perpendicular to this plane. The sp^2 orbitals form the strong σ bonds between carbon atoms in the graphite planes. Condensed hexagonal rings form atomic sheets called graphene with an in plane nearest C-C bond distance of 1.415 Å. Graphite is the stacking of the graphene sheets in a translational ABAB sequence with a perpendicular inter-plane distance of 3.351 Å as illustrated in figure 1.1. Therefore, the third layer is similarly placed with respect to the c-axis as the first layer, and so on.

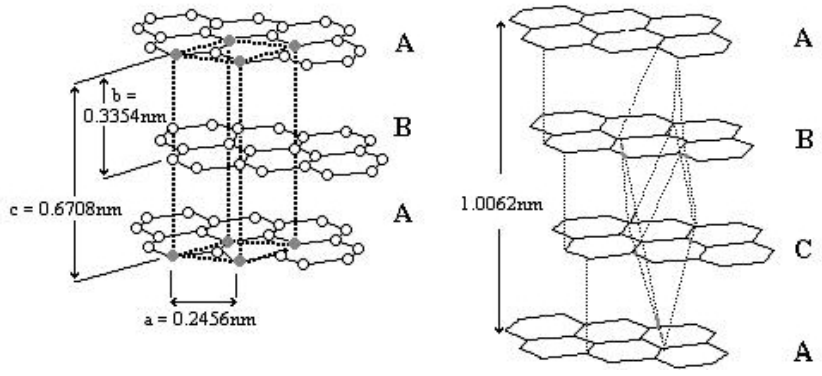

Figure 1.1: Schematic representation of the graphite layers: in a AB sequence (left) and in a ABC sequence (right), the AB graphite is also called Bernal graphite.

This stacking of the layers in an AB sequence is not the only form of graphite. Other studies, with x-ray spectra, electron diffraction and transmission electron microscopy, have shown the existence of rhombohedral graphite [8]. In this structure, the third layer has the same order to the second, as the second to the first, and ABC stacking is formed with respect to the c-axis. By heating to 3000 °C, the rhombohedral stacking is transformed to the more stable AB stacking [9]. A carbon atom of a particular layer is designated as α if it has an atom just above and below itself in the nearest neighbouring layers and as β if it does not. Weak disorder can lead to stacking faults and if the ideal translation is changed, a small increase in the graphite inter-layer distance occurs [10]. It is often called turbostratic graphite and is discussed in chapter 6. The association of

σ and π-bonds make graphite a high anisotropic material. Van der Waals interactions were first identified as weak inter-layer bonds but it has now been shown that the bonding comes mainly through a covalent band-structure term associated with overlap in the delocalised π-electron system of each carbon layer [11].

1.2 Graphite's properties and its industrial use

The final properties of manufactured graphite mainly depend on the precursors used. Precursors are discussed in chapter 4 section 4.2. The bulk density for perfect graphite is around 2.26 $g\,cm^{-3}$ but the density for synthetic graphite can be considerably less due to porosity. Some of its properties are listed below:

- High resistance to thermal shock.
- High compressive strength.
- Low friction and self-lubrication.
- High resistance to chemical attack.
- Low coefficient of thermal expansion (CTE).
- Good electrical conductivity.

Applications which use graphite can also differ depending on whether it comes from a natural or synthetic source. Some of them are reviewed in the following paragraph.

Graphite is used as a lubricant for machinery. Its lubricating properties are believed to arise from the loose interactions between sheets in the structure. Graphite is also used as electrodes to carry the electricity in electric furnaces in metallurgy. It can conduct electricity within the planes of the layers due to some of the free moving valence electrons. It can also be used as anodes in lithium batteries. Graphite is also used as a starting material for synthetic diamond. Finally, graphite is used as a reactor moderator which is further discussed in the next section. It is also the main reason for my research in the present work.

1.2.1 Use in Nuclear reactors

Graphite is used as a moderator in nuclear power reactors [12]. A slow neutron collides with an atom of enriched uranium-235 and it turns briefly into an uranium-236 nucleus. It then splits into fast-moving lighter elements (fission products) and releases free fast neutrons [13]. In order to keep a chain reaction going, fast neutrons have to be slowed down and graphite moderates (decreases) the speed of these neutrons before they are absorbed by another uranium atom. Electricity was generated for the first time by a nuclear reactor in 1951 [12]. Graphite was used in this first reactor due to its moderating properties from its low neutron cross section, and also because it was easily available and cheap [14]. Pure Graphite had a neutron cross-section of $0.0032 \pm 0.0002 \times 10^{-24}\ cm^2$. Manufactured graphite can reach a cross-section of $0.0035 \times 10^{-24}\ cm^2$ [15]. The bulk density for nuclear graphite can be between $1.8 - 2.2\ g\,cm^{-3}$ [16]. In the United Kingdom, it is considered that the graphite used has an average of 20% porosity (table 1.2). Taking this value into account, the bulk neutron absorption coefficient is $0.00033\ cm^{-1}$, which means a slow neutron may travel 33 meters in graphite without capture, however its moderating ability arises from its low atomic weight. The carbon scattering cross-section is $4.69 \times 10^{-24}\ cm^2$, this means that a neutron could travel a few centimetres before it collides with a carbon atom [17]. With this information, Evans reported that graphite has a slowing down power of $0.0625\ cm^{-1}$ resulting in a fast neutron losing 6.25% of its energy per cm inside the graphite bulk [18]. The moderating ratio, used to compare moderator materials, which is calculated from the slowing-down power and the bulk absorption, is 202 for graphite. It is the second best moderator after heavy water [14].

A lower porosity in nuclear graphites is necessary to take into account the dimensional change induced by the neutrons' irradiation inside the graphite bulk [19]. An introduction to the graphitisation process for nuclear graphite is described in chapter 4. Further information on the effect of irradiation in graphite is discussed in section 1.3. Also, not every synthetic graphite is used inside a nuclear reactor and certain requirements are necessary. The material must be semi-isotropic, sufficient density, high thermal conductivity, high purity and a dimensional stability under irradiation, associated with high coefficient of thermal expension (CTE). Some of the properties

Property	Pile grade A		Gilsocarbon
	Parallel	Perpendicular	
Density $[g\,cm^{-3}]$	1.74	1.74	1.81
Coefficient of thermal expansion (20 – 120°C) $10^{-6}K^{-1}$	0.9	2.8	4.3
Thermal conductivity (20°C) $W\,m^{-1}\,K^{-1}$	200	109	131
Young Modulus GPa	11.7	5.4	10.85
Tensile Strength MPa	11	11	17.5

Table 1.2: Typical virgin properties of pile grade A (PGA) and gilsocarbon nuclear graphite [16]

for the UK pile grade A (PGA) and gilsocarbon graphite are presented in table 1.2. PGA was used in Magnox reactors, whereas gilsocarbon was developed for advanced gas reactors (AGRs) due to its more robust properties [16].

1.3 Ordered and disordered graphite

This section tries to show the possible link between graphitisation and radiation damage. Graphitisation begins with a disordered structure to end with a well ordered one, while radiation damage begins with well ordered structure to end with a disordered one.

In radiation damage, a fast neutron collides with a carbon atom, the latter is displaced from its original position. A cascade reaction follows with more carbon atoms being displaced. Depending on how far these atoms are from their original positions, they either go back into the plane or not. When they do not, they become interstitial atoms, and these can move and aggregate with other interstitial atoms. Thus the formation of loops in irradiated graphite [20]. They are often referred to as dislocations loops. Homogeneous nucleation over an irradiation temperature range of 150°C to 650°C has been observed [21]. If it is near a region of high defect density, they can regroup to form loops. Once in place, they start growing by capturing further displaced atoms [21].

In the late stages of graphitisation, basal structural units (BSUs), which are described in 4, can join edge to edge into distorted aromatic layers. These BSUs could be compared to dislocation loops. At even higher temperatures, the remaining interstitial atoms are wiped off to give rise to more or less perfect layers.

The following questions can be asked: Is radiation damage the reverse of graphitisation? Is there any evidence that these two processes show similar features?

The first question cannot be answered just yet. However when experimental works on graphitisation and radiation damage are compared, it can become difficult to tell which process the results come from. A first example comes from transmission electron microscopy (TEM) images. Figure 1.2 illustrates two images taken from a graphitising carbon and from an irradiated graphite. Both images show distorted layers and disordered structures.

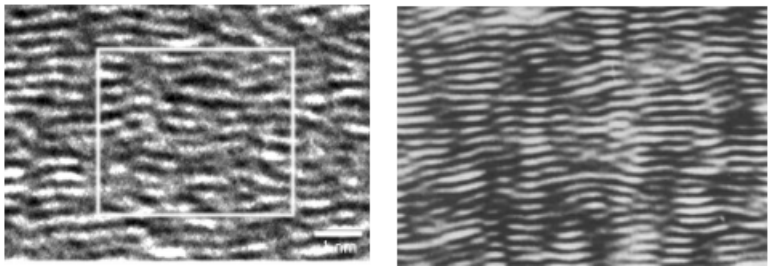

Figure 1.2: TEM images of a graphitising carbon [22] (left) and of an irradiated carbon [23] (right)

Another example comes from x-ray diffraction patterns. Figure 1.3 illustrates two images showing the same characteristics. It is interesting to see two almost identical diffraction pattern images for two different processes.

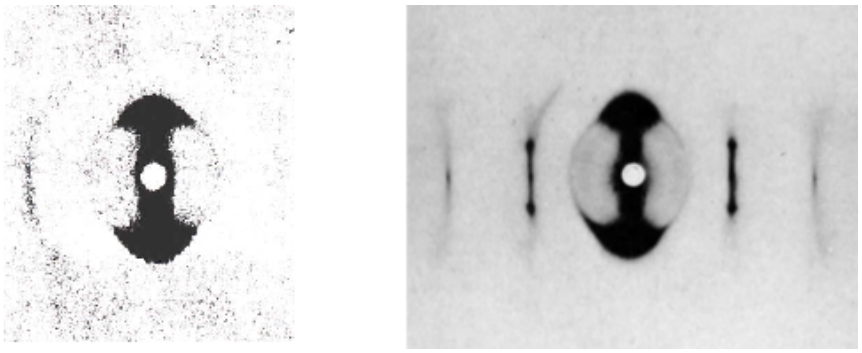

Figure 1.3: Diffraction pattern from a graphitising carbon (left) and from an irradiated carbon [24]

The last example is a comparison of the measured interlayer spacing values. Graphitisation shows a decrease in d_{002} in the late stages of the process while there is a growth in the *c*-direction of the crystal in radiation damage. This is illustrated by the two graphs in figure 1.4.

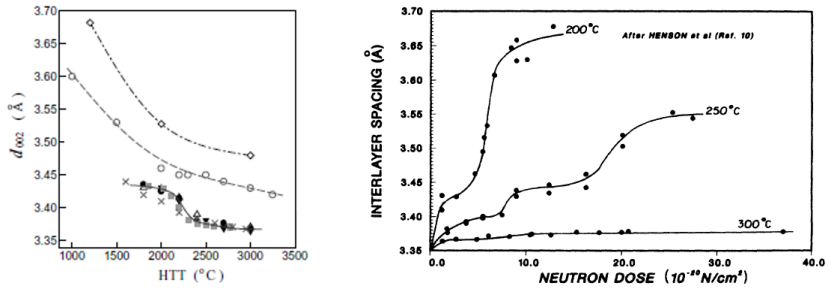

Figure 1.4: Left: Measured interlayer spacing, d_{002}, throughout the late stage of graphitisation [25]; Right: Growth of the crystal in the *c*-direction of graphite at different temperature and different irradiation dose [26].

Understanding graphitisation at an atomic level could greatly improve our knowledge of radiation damage as both processes show similar characteristics at certain stages.

Chapter 2

Theoretical background

This chapter is a review of the fundamental aspects of the many-body problem model; the initial problem is exposed and the methods adopted to solve it are described. This section starts with the Schrödinger equation, followed by the Hartree-Fock theory (HFT) and the density functional theory (DFT). The two main exchange-correlation energy functions inside DFT, the local density approximation (LDA) and the conjugate gradient approximation (GGA), are also explained. Finally, the pseudopotentials, a simplification allowing to speed up the theory is presented. More detailed informations can also be found in these reference [27, 28, 29].

2.1 The Schrödinger equation

The simplest form of the non-relativistic time-independent Schrödinger equation, for a system consisting of N_e electrons and N_n nuclei, is:

$$H\Psi = E\Psi. \tag{2.1}$$

with the wave function, Ψ, containing all the information known about the quantum system. E is the numerical value of the total energy of the state described by Ψ. H

is the Hamiltonian operator, it can be expanded to a more general form:

$$\begin{aligned} H &= T_e + T_i + V_{i-e} + V_{e-e} + V_{i-i} \\ &= -\frac{1}{2}\sum_{i=1}^{N_e}\nabla_i^2 - \frac{1}{2}\sum_{A=1}^{N_n}\frac{1}{M_A}\nabla_A^2 - \sum_{i=1}^{N_e}\sum_{A=1}^{N_n}\frac{Z_A}{r_{iA}} \\ &\quad + \sum_{i=1}^{N_e}\sum_{j>i}^{N_e}\frac{1}{r_{ij}} + \sum_{A=1}^{N_n}\sum_{B>A}^{N_n}\frac{Z_A Z_B}{R_{AB}} \end{aligned} \tag{2.2}$$

where A and B represent the nuclei, i and j denote the electrons in the system. The first two terms, T_e and T_i respectively, represent the kinetic energy of both the electrons and the nuclei. The Laplacian operator ∇, summarizes the sum of differential operators. M_A is the mass of nucleus A. The last three terms represent, in order, the attractive interaction between the nuclei and the electrons, the electron-electron repulsive potential and the nucleus-nucleus interaction. The equation 2.2 is expressed in atomic units, so that Planck's constant, $\hbar$, the permittivity of the vacuum $4\pi\varepsilon_0$, the mass of electron (m_e) and the electronic charge (e) are equal to one and not shown. To solve equation 2.2, decoupling the motion of the electrons and ions components of the many-body wavefunctions must be achieved.

2.2 The Born-Oppenheimer Approximation

The Schrödinger equation can be simplified because of the important mass difference between the nuclei and the electrons. A light atom like hydrogen, has a nucleus 1,800 times heavier than an electron. For an element like carbon, it is above 20,000 times, so the electrons move much faster than the nuclei. From this, the electrons are considered to be moving in the fields of fixed nuclei, this is the Born-Oppenheimer (or clamped nuclei) approximation. If the nucleus is fixed then its kinetic energy is zero and the potential energy due to nucleus-nucleus repulsion becomes constant. Thus the second and the last term of equation 2.2 are unnecessary. The Hamiltonian is now called the electronic Hamiltonian, H_{elec}:

$$H_{elec} = -\frac{1}{2}\sum_{i=1}^{N_e}\nabla_i^2 - \sum_{i=1}^{N_e}\sum_{A=1}^{N_n}\frac{Z_A}{r_{iA}} + \sum_{i=1}^{N_e}\sum_{j>i}^{N_e}\frac{1}{r_{ij}}$$

Now equation 2.1 can be rewritten with the electronic wave function Ψ_{elec} and the electronic energy E_{elec} as:

$$H_{elec}\Psi_{elec} = E_{elec}\Psi_{elec} \tag{2.3}$$

The total energy, E_{tot}, is the sum of E_{elec} and the constant nuclear repulsion term E_{nuc}:

$$E_{tot} = E_{elec} + E_{nuc} = E_{elec} + \sum_{A=1}^{N_n}\sum_{B>A}^{N_n}\frac{Z_A Z_B}{R_{AB}}$$

Despite this simplification, solving the Ψ term from equation 2.1 is a difficult task because of the nature of the electrons. Further approximations must be made.

2.3 The Hartree Approximation

To deal with the many-particle problem, it can be assumed that each electron can be considered separately. All of them are treated as if they were moving in a mean field potential V_r. The one-electron equation has the form :

$$(-\frac{1}{2}\nabla^2 + V_r)\psi_i = \epsilon_i\psi_i$$

with the constant ϵ_i a Lagrange multiplier introduced to take into account the normalization of the single particle state ψ_i. The Hartree approximation starts from the one-electron equation. From equation 2.3, the electrons are assumed to be non-interacting, and so the N-electron wavefunction Ψ_i (Ψ_{elec} in equation 2.3) is just the product of the one-electron wavefunction ψ_i.

$$\Psi_i(r_i) = \psi_1(r_1)\psi_2(r_2)...\psi_N(r_N)$$

In this approximation, V_r models the mean electrostatic potential of all the electrons too [30]. V_r is now equal to:

$$V_r = V_{ion} + \int \frac{n(r')}{|r - r'|} dr',$$
$$n(r) = \sum_{i=1}^{N} |\Psi_i(r)|^2$$

with V_{ion} the ions' potential contribution. The second term is the remaining electrons potential contribution. The total many-body wavefunction is then formed as the product of these one-electron spin orbitals. However if two electrons of the same spin interchange positions, Ψ must change sign, this is known as the exchange energy following Pauli's exclusion principle.

$$\Psi(r_1 s_1, r_2 s_2, ..., r_N s_N) = -\Psi(r_1 s_2, r_2 s_1, ..., r_N s_N)$$

Moreover, each electron is affected by the motion of the other electrons in the system, defined as the correlation energy. The Hartree equation, being a good approximation, still has something missing: the electronic exchange.

2.4 Hartree-Fock (HF) Approximation

The next step is to incorporate the exchange properties of the electron in the many-body wavefunction $\Psi(r_i s_i)$. An anti-symmetrised wavefunction with the Hartree wavefunction is thus chosen: the Hartree-Fock approximation. To overcome the problem of the same spin interchange positions, a determinant, first introduced by Slater, is used [31].

$$\Psi(r_1 s_1, r_2 s_2, \ldots, r_N s_N) = \frac{1}{\sqrt{N!}} \begin{vmatrix} \psi_1(r_1 s_1) & \psi_1(r_2 s_2) & \cdots & \psi_1(r_N s_N) \\ \psi_2(r_1 s_1) & \psi_2(r_2 s_2) & \cdots & \psi_2(r_N s_N) \\ \vdots & \vdots & & \vdots \\ \psi_N(r_1 s_1) & \psi_N(r_2 s_2) & \cdots & \psi_N(r_N s_N) \end{vmatrix}$$

The determinant would change sign if two columns are altered/swapped. It is equivalent to interchanging the position of two electrons. Using a simpler notation,

the equation above becomes:

$$\Psi(r) = \frac{1}{\sqrt{N!}} \det\left|\psi_N(r_N)\right|$$

where the one-electron function $\psi_N(r_N)$ introduces electron spin via a spatial orbital ψ_j(r) and a spin function $\sigma(s)$, which can have the notation either $\alpha(s)$ or $\beta(s)$:

$$\psi_\lambda(r) = \psi_j(r)\sigma(s)$$

The spin functions are orthonormal ($\alpha\alpha$=$\beta\beta$=1 and $\alpha\beta$=0) and satisfy the equations:

$$\sum_s \sigma_\alpha^*(s)\sigma_\beta(s) = \delta_{\alpha\beta}$$

$$\int \psi_i^*(r)\psi_j(r) = \delta_{ij}$$

where the Kronecker delta symbol, δ, is used.

It is important to find the most suitable Slater's determinant, which would give the lowest energy. The only flexibility in the determinant comes from the spin orbitals. In the Hartree-Fock method, the spin orbitals, σ_i, are varied so the energy obtained from the determinant is minimal while the spin orbitals remain orthonormal using the Lagrange multiplier $E_{\lambda\mu}$. The Hartree-Fock equation is for each orbital λ:

$$\left\{-\frac{1}{2}\nabla^2 + V_{i-e}(r) + V_H(r) + V_\lambda^x(r) - E_\lambda\right\}\psi_\lambda(r) = \sum_{\mu\neq\lambda} E_{\lambda\mu}\psi_\mu(r) \tag{2.4}$$

where the first and second terms are the kinetic and potential energies, i.e. the one-electron energy. The third and fourth term ($V_H(r)\psi_\lambda(r)$ and $V_\lambda^x(r)\psi_\lambda(r)$) are the Hartree and exchange potential respectively:

$$V_H(r)\psi_\lambda(r) = \frac{\delta E_H}{\delta\psi_\lambda^*} = \int \frac{n(r_1)\psi_\lambda(r)}{|r-r_1|}dr_1,$$

$$V_\lambda^x(r)\psi_\lambda(r) = \frac{\delta E_x}{\delta\psi_\lambda^*} = -\sum_{\mu s_1} \frac{\psi_\mu^*(r_1)\psi_\lambda(r_1)\psi_\mu(r)}{|r_1-r|}dr_1$$

Equation 2.4 can be simplified by removing $E_{\lambda\mu}$ with diagonalisation so the right hand side becomes zero. In order to find E_{tot}, the total energy, the equation is multiplied by $\psi_\lambda{}^*(r)$ integrated over r and summed over s and λ to give:

$$-\sum_{\lambda,s}\int \psi_\lambda{}^*(r)\frac{1}{2}\nabla^2\psi_\lambda(r)dr \quad - \quad \sum_{\lambda,s}\int \psi_\lambda{}^*(r)V_{i-e}(r)\psi_\lambda(r)dr$$

$$+\sum_{\lambda,s}\int \psi_\lambda{}^*(r)V_H(r)\psi_\lambda(r)dr \quad + \quad \sum_{\lambda,s}\int \psi_\lambda{}^*(r)V^x_\psi\lambda(r)dr - \sum_{\lambda,s}E_\lambda(r) = 0 \qquad (2.5)$$

The Hartree and exchange potentials are equal to twice the Hartree and exchange energies respectively. Therefore, equation 2.5 is rewritten:

$$T_e + E_{e-i} + 2E_H + 2E_x - \sum_\lambda E_\lambda = 0$$

The total energy can be calculated by removing the double counting and adding the ion-ion energy term:

$$E_{tot} = \sum_\lambda E_\lambda - E_H - E_x + E_{i-i}$$

The Hartree-Fock equation is solved by predicting the spin orbital $\psi_\lambda(r)$ and calculating the Hartree and exchange potentials. The new potentials are then used to determine $\psi_\lambda(r)$. The process is repeated many times until the difference between the input potential and the output potential is minimal. This is called a self-consistency method. This early computational method gives relatively good optimised structures and vibrational modes for small molecules but is not accurate enough for bond lengths or frequencies. The lack of electron correlation is a problem for metallic compounds where the band gap is often over-predicted. Different approaches exist to tackle this weakness, collectively called post-Hartree-Fock methods (e.g. Møller-Plesset perturbation theory (MP) [32]). Hartree-Fock is very useful for small molecules but becomes time consuming when the number of atoms, hence the number of electrons, is increased due to the complicated N-electron wavefunction with its dependence on 3N spatial plus N spin variables (4N dependency) for every electron.

2.5 Density-Functional Theory (DFT)

Molecules in chemistry, biology and other areas usually involve many electrons, so any wavefunction based calculation will reach an 'unquantified' size. The HF method shows its limits. Another approach needs to be used for larger systems. This method works to simplify the many-body problem by working with the electronic charge density, $n(r)$, as fundamental variable rather than the wavefunction. Thus evolved density functional theory. The idea is that the 4N dependency for every electron described in the Hartree-Fock approximation is now defined by the charge density which is a function of only three spatial variables and spin. It was first introduced by the Thomas-Fermi model in 1927. This model is not discussed further and is more of an historical interest as it was the first form of DFT. Density functional theory, as used today, was introduced in 1964 by Hohenberg and Kohn (HK) and then by Kohn and Sham (KS) in 1965 [33, 34]. Their paper shows that there is a one-to-one correspondence between a non-degenerate, non-polarised ground state wavefunction, Ψ(r) and the electron density n(r) defined by:

$$n(r_1) = \sum_{\mu} \int \delta(r_1 - r_\mu)|\Psi(r)|^2 dr$$

Using the electron Hamiltonian equation, HK demonstrated, that:

$$H = T_e + V_{i-e} + V_{i-i}$$

the external potential V_{i-e} is a unique functional of $n(r)$, and since V_{i-e} fixes $\hat{H}$, the full, many-particle ground state is a unique functional of $n(r)$. Moreover, the total energy E is also related to the charge density,

$$E[n] = T[n] + E_{i-e}[n] + E_{i-i}[n] + E_H[n] + E_{xc}[n]$$

including the Coulomb energy (E_{i-e}[n]),

$$E_{i-e}[n] = -\int n(r) \sum_A \frac{Z_A}{|r - R_A|} dr$$

the ion-ion interaction (E_{i-i}[n]),

$$E_{i-i}[n] = \frac{1}{2}\sum_{A\neq B}\frac{Z_A Z_B}{|R_A - R_B|}$$

the Hartree energy (E_H[n]),

$$E_H[n] = \frac{1}{2}\int \frac{n(r_1)n(r_2)}{|r_1 - r_2|}dr_1 dr_2$$

the kinetic energy of the set of non-interacting particles:

$$T[n] = -\frac{1}{2}\sum_i \int \psi_i^* \nabla^2 \psi_i(r) dr$$

Finally, the exchange correlation energy (E_{xc}[n]) includes all the terms due to interactions within the gas. It is the only term with no explicit form and is the big unknown. By guessing an initial charge density, E_{xc}[n] is obtained and used afterwards to obtain the new charge density and so on until it converged. It can also be noted that if the exact form of E_{xc} was known, the KS approach would lead to the exact energy, and subsequently the exact Hamiltonian operator of the Schrödinger equation.

2.6 Local Density Approximation (LDA)

The Kohn-Sham method is still subject to a better approximation to determine the exchange-correlation energy. An early approximation is the local density approximation. All approximate exchange-correlation functionals are based on this system. LDA states that for any small region in the system, the exchange-correlation is the same as for the uniform electron gas with the same electron density. This model is far from the situation in molecules, because the densities vary rapidly, but it is the only system where its exchange-correlation energy functional is known with high accuracy. In this case we write E_{xc}:

$$E_{xc} = \int n(r)\varepsilon_{xc}(n)dr \tag{2.6}$$

where ε_{xc} can be split in two values:

$$\varepsilon_{xc}[n(r)] = \varepsilon_x[n(r)] + \varepsilon_c[n(r)]$$

with the exchange part, ε_x, which represents the exchange energy of an electron in a uniform electron gas of a particular density and is written:

$$\varepsilon_x = -\frac{3}{4}\sqrt[3]{\frac{3n(r)}{\pi}}$$

No such explicit version is known for the correlation part, ε_c, but accurate quantum Monte-Carlo simulation of the homogeneous electron gas from Ceperley's and Alder's work is available [35]. The equation 2.6 is for a spin average energy density. There is also a spin polarised variation called the local spin density approximation (LSDA) which introduces the energy density for a polarised homogeneous electron gas. Even though results can be better or at least comparable to HF approximation, the LDA approximation, unfortunately, has disadvantages: it under-predicts atomic ground state energies and ionisation energies, while also over-predicting binding energies. In general this method is not fully accurate for small molecules but improves with larger systems.

Analytical expressions of ε_c

The work done by Ceperley and Alder resulted in other groups presenting analytical expressions of ε_c. One of the first was developed by Vosko, Wilk and Nusair in 1980 [36]. These were later parametrised by Perdew and Zunger in 1981 and improvements were later added by Perdew and Wang [37, 38]. The AIMPRO code uses the latter, this is further explained in section 3.2.2. The correlation energy per electron, ε_c, the spin-polarisation parameter ζ and Wigner-Seitz radius of each electron r_s are defined as:

$$E_c = \Omega n \varepsilon_c(n, \zeta), \qquad \zeta = \frac{n_\uparrow - n_\downarrow}{n}, \qquad r_s = \sqrt[3]{\frac{4\pi n}{3}},$$

where ζ attains values from 0 (spin compensated) to 1 (fully spin polarised). ε_c is given by [38]:

$$\varepsilon_c(r_s,\zeta) = \varepsilon_c(r_s,0) + \alpha_c(r_s)\frac{f(\zeta)}{f''(0)}(1-\zeta^4) + [\varepsilon_c(r_s,1) - \varepsilon_c(r_s,0)]f(\zeta)\zeta^4,$$

$$f(\zeta) = \frac{[1+\zeta]^{4/3} + [1-\zeta]^{4/3} - 2}{2^{4/3} - 2}$$

It is possible to simplify these expressions and AIMPRO uses such simplifications. More information and details about the parameter values can be found in Perdew's paper which also states: "We recommend the use of these formulas in density-functional and other calculations..." [38]. In DFT, this exchange correlation function has the short notation PW92. It is one of the latest approximations and it is regarded as one of the most efficient.

2.7 Generalised Gradient Approximation (GGA)

This is not used in the calculations presented later as GGA has been shown to give inaccurate interlayer spacing in graphite [39] but it is valuable to acknowledge another form of approximation, especially when it is an extension to LDA. For the disadvantages mentioned in the previous paragraph, other exchange correlation forms were found to move beyond the LDA notably through the addition of gradient corrections ∇_n to account for the non-homogeneity of the electron density.

$$E_{xc}[n_\uparrow, n_\downarrow] = \int n(r)\varepsilon_{xc}(n_\uparrow, n_\downarrow)dr + \sum_{\sigma,\sigma'}\int C_{xc}^{\sigma,\sigma'}(n_\uparrow, n_\downarrow)\frac{\nabla_{n_\sigma}}{n_\sigma^{2/3}}\frac{\nabla_{n'_\sigma}}{n'^{2/3}_\sigma}dr + ...$$

This form of functional is called the *gradient expansion approximation*. Unfortunately, it does not improve the accuracy and can give worse results due to the missing exchange-correlation hole properties, present in LDA [40]. Functionals that include the gradient of the charge density and where the hole constraints have been restored

are called *generalized gradient approximations* (GGA). It is usually written:

$$E_{xc}^{GGA} = E_x^{GGA} + E_c^{GGA},$$

$$E_x^{GGA} = E_x^{LDA} - \sum_\sigma \int F(s_\sigma) n_\sigma^4 / 3 dr$$

where F is the enhancement factor that directly modifies the LDA energy density for a spin σ. s_σ is usually interpreted as a local inhomogeneity of small densities. The function can be complicated and will not be further discussed. The gradient-corrected correlation functionals for E_c^{GGA} are also complicated and can be found in papers from Perdew, Perdew and Wang and Lee to just name a few [40, 41, 42]. Although these improvements seem to give better total energies, the optimised structure is often worse and at a greatly increased computational cost. Care should be taken when a choice must be made between LDA and GGA. By introducing Van der Waals forces in the energy functional on an ab initio basis, the interlayer binding energy of graphite using GGA have been found to be similar to experimental values [43].

2.8 Kohn-Sham Orbitals (KS)

By keeping the number of electrons and spins of the system fixed, the KS orbitals can be calculated by minimising the total energy, E, with respect to $n(s)$. To do so, one needs to keep the orbitals ψ_λ orthonormal, and apply the variational principle, including the Lagrange multiplier E_λ.

$$E(n) - \sum_\lambda E_\lambda \left\{ \sum_s \int |\psi_\lambda(r)|^2 dr - 1 \right\}$$

and by differentiating it with $\psi_\lambda^*(r)$, the KS equation becomes:

$$\left\{ -\tfrac{1}{2}\nabla^2 - \sum_A \tfrac{Z_A}{|r-R_A|} + V^H(r) + V_{s\lambda}^{xc}(n_\uparrow, n_\downarrow) \right\} \psi_\lambda(r) = E_\lambda \psi_\lambda(r),$$

$$V_s^{xc} = \frac{d(n\varepsilon_{xc})}{dn_s}$$

The self-consistent solution of this determines the ground state charge density of the system. The HF orbitals, due to their lack of correlation effects, are not representing the the real system correctly. Therefore the KS orbitals are recommended for qualitative molecular orbital (MO) calculations although in KS theory, it is not possible to relate the orbital energies to ionisation energies.

Discussion

Many comparisons have been made between DFT and similar methods based on the molecular wavefunction but DFT seems to be a good cost-effective approximation to get a certain level of accuracy [44]. However there are also downsides to this; DFT and molecular orbital theory are different. MO theory optimises a wavefunction and DFT an electron density. As already pointed out previously, the computational efficiency of DFT is N^3, with N the number of basis functions representing the KS orbitals, compared to the N^4 with HF theory or methods with a greater complexity (e.g. MP2, MP3, CISD and others which are not discussed). Most DFT codes use the Kohn-Sham self-consistency field (SCF) approach, but there are limitations to the KS formalism. Its main advantage is to compute the kinetic energy for a single KS determinant but in MO theory, some systems (e.g. transitions metals) are not always well described with a single Slater determinant. This problem can sometimes be solved by using an unrestricted KS formalism or by allowing the wavefunction to break spin symmetry as in LSDA. A final disadvantage of the theory, as density functionals are approximate for arbitrary molecular systems, is its difficulty to prove its accuracy if there is no other answer for a particular problem. Fortunately, experimental datas exist for many systems which DFT can be compared to. Despite certain failures in the model, DFT, as an *ab initio* theory, is a method of choice and has proven to be accurate for many aspects of different systems (energies, structures ...) [44].

2.9 Pseudopotentials

The use of pseudopotentials is to simplify calculations even further. It was first introduced in 1935 [45]. An atom is constituted of core and valence electrons and the

properties of a material are mainly governed by the valence electrons. Pseudopotentials include all the core states into a bulk nuclear potential, only leaving the valence electrons to be handled separately. For example, in carbon, the 1s electrons are included in the nuclear potential. This approximation can have considerable effects on the results:

- If all the electrons were included in the calculation, the total energy would be very large and negative, and the comparison of two systems could return large errors, resulting from the difference of two large numbers.
- In heavier atoms, the mass of the core electrons can be more significant than the valence electrons.
- Including core electrons explicitly can make the fitting to a Gaussian or plane-wave basis very difficult.

Pseudopotentials take into account the core states that do not take part in bonding and it also deals with the interactions with the valence electrons. The pseudo wavefunction should be reasonably close to the true wavefunction and few parameters should be set while constructing a new pseudopotential:

- The real and pseudo valence eigenvalue fro the atom have to be equal.
- Beyond the core radius r_c, the real and pseudo wavefunctions have to be identical.
- Beyond r_c, the real and pseudo first energy derivatives agree.

The construction of pseudopotentials is not an easy task. Fortunately, for their influence in DFT, different pseudopotentials have been made available. Bachelet *et al.*, for example, studied the pseudopotentials from hydrogen to plutonium [46]. It was first used with the AIMPRO package. In the new AIMPRO versions, the pseudopotentials developed by C. Hartwigsen, S. Goedecker and J. Hutter are chosen [47].

Chapter 3

The Ab Initio Modelling PROgram (AIMPRO) package

The AIMPRO code was first written by Professor R. Jones (Exeter University) and was extended and rewritten several times by his former PhD student Doctor R. Briddon (Newcastle University). It is a self-consistent density functional code. This chapter provides details of AIMPRO theoretical approaches and the principal types of calculation available in it. The package has many other tools available which are not necessarily described here, more information is available elsewhere [48], with further theoretical background in [49].

3.1 General AIMPRO

3.1.1 Self-consistency

A set of parameters are provided, by the user inside an input file, to meet a desirable accuracy for the calculation. The position of each individual atom, using x, y and z coordinates, is also given. From the types of atoms specified in this file, a starting charge density can be guessed from a sum of the charge density of these neutral atoms. The code uses a self-consistent method with an iterative approach. The Kohn-Sham

equations have to be solved:

$$\sum_j (H_{ij} - E_\lambda S_{ij}) c_j^\lambda = 0$$

After optimisation, new wavefunction expansion coefficients c_j^λ are found. H_{ij} and S_{ij} are matrix elements of the Hamiltonian and the overlap respectively. These are used to calculate the new charge density. Each iteration gives a minimised total energy. If the new charge density does not equal the previous one or is not equal within the tolerance specified in the input files, then the new charge density is fed into the equation again and the process is repeated, it is called a self-consistent cycle. When the conditions are fulfilled the cycle ends and a minimum energy is given for the current set of atomic positions. The final convergence can sometimes be difficult or fail for various reasons. If this happens, AIMPRO gives the possibility to change a few parameters such as the type of occupancy smearing to be used in populating the Kohn-Sham levels -in our calculations we used Methfessel-Paxton [50]- or to give the energy equivalent for an effective electronic temperature, kT (in eV) of the electronic system.

3.1.2 Basis Set

AIMPRO uses charge density as the fundamental variable to its advantage. In order to solve the Kohn-Sham equations, the Kohn-Sham spin orbitals need to be expanded in a basis function. It is usually written:

$$\psi_{\lambda s}(r) = \sum_{i=1}^{N} c_i^{\lambda s} \phi_i(r)$$

where c_i is the expansion coefficient. The number of functions N used and the choice of the functions $\phi_i(r)$ limit the accuracy of this approach. There are two common choices of basis function: plane waves and Gaussian type orbitals. A majority of codes would use plane waves as they easily match periodic boundary conditions. The function is written:

$$\phi_i(r) = exp[i\underline{G} \cdot \underline{r}]$$

where $\underline{r}$ is the position vector and $\underline{G}$ is the propagation vector. Their use is equivalent to making a Fourier transform of the wavefunction. There are many other advantages of using a plane wave basis set but one of the main disadvantages is the large number of functions needed even for a light atom. This increases even more when heavier atoms or combinations of different species are studied in the same unit cell. The consequence is a large memory usage and an increase in the time needed for each iteration. AIMPRO uses the other approach, where the function ϕ_i is a localised Cartesian Gaussian function written:

$$\phi_i(r) = (x - R_{ix})^{n_1}(y - R_{iy})^{n_2}(z - R_{iz})^{n_3} e^{-\alpha_i(r-R_i)^2}$$

where n_1, n_2 and n_3 are non-negative integers. Linear combinations of these Cartesian Gaussian functions can be chosen to form other functions. These new functions can be labelled as $s-$, $p-$ or $d-$type. For example, if the sum of n_1, n_2 and n_3 is zero then the function is a $s-$type orbital. $p-$orbitals correspond to one of these integers being one and the others zero.

This method is very efficient and can result in a calculation four or five times less resource demanding than plane waves for an identical unit cell. In order to treat difficult elements, such as transition metals, higher angular momentum functions need to be placed on that atom without changing the basis sets for other elements. Another advantage of localised orbitals is, even if the size of the system increases, the Hamiltonian matrix does not become harder to solve, it becomes sparser and amenable to linear scaling methodologies. Unfortunately, using a Gaussian basis with a high number of functions requires fiddling with many parameters (exponents, number of functions and location of the function centres), numerical noise can appear and an 'over-complete' basis set can be produced. Another disadvantage of this method compared to calculations using a plane-wave basis, is a fully converged total energy of the system cannot be easily obtained. However, when energy differences between two systems are compared, AIMPRO gives reliable results through cancellation of errors. In a Gaussian basis, the coefficients of the functions and their exponents are the two parameters to be specified for an individual atom. AIMPRO allows the users to optimise basis sets. The package provides an optimal coefficient for an atom but

the exponents α_i have to be first guessed, then optimised a few times by the user to minimise the energy. Most of the atoms in the first few rows of the periodic table and their well-known molecules (e.g. Carbon dioxide, benzene and graphite) have already been optimised and verified by former users of the code. The new users just have to carefully choose the right basis set and only optimise a new one when it is necessary.

3.1.3 Structural Optimisation

When approaching a new system, one of the first tasks, is to find the lowest energy state from the unoptimised atomic positions. The easiest way is to calculate the forces acting on each atom. They are individually moved to find a lower energy state and a new structure is obtained. Once the energy has been minimised with regards to the charge density, the eigenstates are known and the forces acting on each atom can be determined. The forces are given by the Hellmann-Feynman theorem and can be simply written [51, 52]:

$$F_A = -\frac{\delta E}{\delta R_{Al}}$$

where F_A is the force, R_{Al} is the coordinate of the atom A and E is the energy. To achieve the lowest energy state, a conjugate gradient method is used [53]. Each atom is moved in the direction of the forces in the first iteration. Subsequent iterations have the requirement that the new direction has to be orthogonal to all previous directions. By using a mathematical function for the energy along the new direction, the distance of the displacement is chosen to arrive at the position with a minimum energy. Shewchuk wrote a detailed introduction on the conjugate gradient method [54].

One of the drawbacks of this approach is that the geometry optimisation can be stopped in a local minimum (figure 3.1) which is different from the global minimum. To avoid or to verify if a structure is not located in a local minimum, is not easy to do rigorously but a practical method is to start with a slightly different initial structure. It is often understood that a structural optimisation is a rearrangement of the atom only but AIMPRO allows, like many other programs, the optimisation

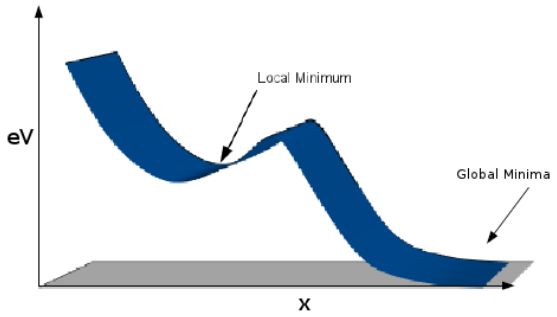

Figure 3.1: Scheme representing a local minimum

of the lattice parameters giving a zero pressure simulation. The choice can either be to optimise the atom positions and the lattice parameters together or separately. Figure 3.2 illustrates the route used by AIMPRO for a structural optimisation.

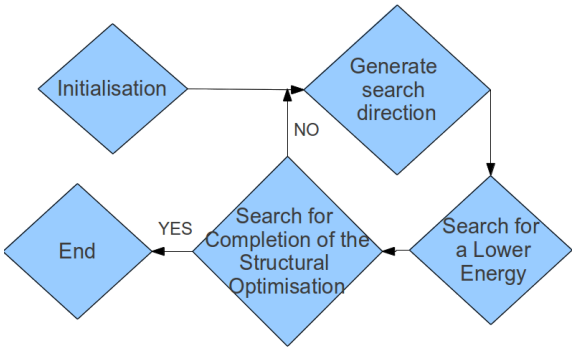

Figure 3.2: Schematic AIMPRO optimisation

3.1.4 Calculating Diffusion Barriers

Calculating diffusion barriers requires finding a saddle-point, similar to a local minimum, between an initial and a final structure. In figure 3.1, there is an energy barrier between the local minimum and the global minimum (i.e. lowest energy). This method gives an accurate energy for the barrier to go from one structure to the other. There are four available techniques in AIMPRO. The more appropriate technique chosen in the later calculations is called Nudged Elastic Band (NEB) [55, 56]. The coordinates of the initial and final structures are given by the user, an additional structure of the transition state can be given too. From these, a series of images is built by creating a path by linear interpolation, the more images the better the

approximation so as to avoid abrupt changes in bonding which could represent a poor approximation. The atomic positions are optimised for each image created using forces modified to ensure an uphill energy direction. Additional forces are included between adjacent images as though the images were connected by elastic bands. NEB calculation should be run with care because it is easy to use large amounts of CPU, often to no great effect and the saddle point can be missed in the linear interpolation. When a calculation is finished, AIMPRO gives the possibility to restart from the latest coordinates, to implement more images between the ones from the previous run and to also find the structures of the saddle point, confirming that the Hessian has one and only one imaginary eigenvalue.

3.1.5 Band structure (BS)

When studying solids, it is quite often important to look at the energy levels. For Bloch functions, this yields a band structure $E(\underline{k})$ (see later equation 3.1). The occupation limit is given by the Fermi level. The wavevector $\underline{k}$ takes on values within the Brillouin zone (BZ) corresponding to the crystal lattice. The BZ is the region where every eigenstate of an electron can be represented. Its shape is connected to the symmetry of the crystal and its irreducible representation is the zone reduced by all the symmetries in the point group of the lattice. More information can be found in the appendix A. It is always defined with known points, usually labelled by $\Gamma, \Delta, \Lambda, \Sigma$ and others. Another program, called AIMVIEW, allows visualisation of any molecular orbital or Bloch function; to analyse its composition in the system (see picture 3.3)(e.g. p_x, p_y or p_z orbitals).

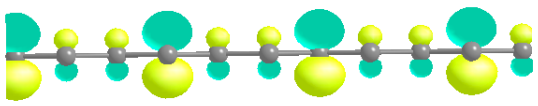

Figure 3.3: Side view of a Bloch function from a graphene band

3.1.6 Other type of job

Another possibility is to run a Mulliken analysis [57]. One of the useful properties of a molecule or a solid is its charge or spin density distribution. This analysis estimates the valence electron population associated with each atom. The sum of the Mulliken charges is equal to the total number of electrons in the system and the Mulliken spin density is calculated from the difference of the Mulliken charges of spin-up and spin-down electrons. Its sum equals the total spin of the system.

The second derivative energy of a system can be computed to find the vibrational modes of individual atoms. An atom a is moved by a distance $\pm d$ along the cartesian vector m, the charge density is then recalculated giving the forces, $f^{\pm}(l,a)$, on each atom in each direction, l. The double derivative D is written:

$$D = \frac{f^{+}(l,a) - f^{-}(l,a)}{2d} = \frac{\delta^2 E}{\delta r_l \delta r_m}$$

3.2 Cluster or Supercell

AIMPRO gives the possibility to choose between a cluster or a supercell mode. A cluster run is designed for the simulation of an isolated, finite atomic assemblage and a supercell run is used to simulate an infinite, crystalline material by exploiting periodic boundary conditions.

3.2.1 Cluster

The cluster mode was the only one available in the first versions of AIMPRO. It is mainly used for molecules which cannot be described as a crystal. It can also simulate parts of a crystal but each edge of the cell must be terminated with atoms of hydrogen to saturate the dangling bonds. There are some issues using this method. Hydrogen atoms tend to give an overestimate for the band gap compared to experimental values and also increase the computational time. There are few advantages of using the cluster mode, but one is the speed. Another is if the symmetry of a system is not supported in a supercell run since only 2, 3, 4 and 6 fold symmetries are possible.

So a molecule with a C_5 axis cannot, in theory, be optimised in a supercell without compromising its symmetry. Another advantage, and not the least, is the ability to give a charge to a molecule whereas in a supercell, charge must be compensated with an opposite charge spread over the whole lattice. A distinct disadvantage is the default functional, which is a *Padé* approximation to the PW 92 functional [48]. GGA calculations cannot be performed under a cluster run.

3.2.2 Supercell

The supercell method is the most widely used in the calculations presented later and is more convenient for studying bulk systems. It can model a crystal by repeating one unit cell in the three lattice vectors directions indefinitely. To make it more efficient a primitive unit cell, i.e. the smallest possible cell to be repeated to form a crystal should be used. When using periodic boundary conditions, Bloch's theorem should be applied [58]. It states that the wave function, $\psi_k(r)$, is a product of plane waves $e^{i\underline{\mathrm{k}}.\underline{\mathrm{r}}}$ and a periodic function of the lattice $\upsilon_k(r)$ that has the same periodicity as the potential:

$$\psi_k(r) = e^{i\underline{\mathrm{k}}.\underline{\mathrm{r}}}\upsilon_k(r) \tag{3.1}$$

In AIMPRO, the plane waves are used for the charge density and an expansion in the Gaussian basis set is used for generating wave functions. AIMPRO uses the functional PW92 (LDA) as default in supercell mode and if GGA is required it must be specified in the input file. The GGA functional is PBE96 [59]. One option is to use the real space build for the Hamiltonian matrices [60]. Using this parameter typically results in considerable speed gain when the lattice vectors are orthogonal. And if they are orthogonal then the real-space build is effective for even quite small systems, but for other lattice types, more atoms are required to obtain an advantage. The disadvantage of this technique is that it requires the usage of more memory.

Should I run cluster or supercell mode?

The question must be asked depending on the computer resources available and the accuracy needed for a certain job. But nowadays, even desktop machines are powerful enough to run supercell mode. Also, when simulating molecules and clusters, it may still be best to use the supercell modes, introducing vacuum between each repeated cell. It is often referred to as the 'cluster in box'. The vacuum (fictitious environment) between 'repeated' cells must be sufficiently large that no significant interaction is present. This method allows to simulate molecular systems using the GGA-PBE functional.

3.2.2.1 *k*-points sampling mesh

A supercell run invokes the Kohn-Sham equations to be solved in reciprocal space, also called *k*-space. *k*-space is a Fourier transform of real space. The real space, with lattice vectors $\vec{a}_1$, $\vec{a}_2$ and $\vec{a}_3$, has a reciprocal space, with lattice vectors $\vec{b}_1$, $\vec{b}_2$ and $\vec{b}_3$. One can be calculated from the other using the equation:

$$\vec{a}_i \bullet \vec{b}_j = 2\pi\delta_{ij}$$

where δ_{ij} is a Kronecker delta function. From the equation 3.1 of Bloch's theorem, the value of $\vec{k}$ gives the periodicity of the wavefunction $\psi_k(r)$ and its whole range of wave vectors defines the *k*-space. The energy of a free electron $E(\vec{k})$ is directly related to $\vec{k}$:

$$E(\vec{k}) \propto |\vec{k}|^2$$

To summarise, each point *k* in the *k*-space has a wavefunction ψ_k, with an eigenvalue E_k, and it provides a solution of the Kohn-Sham equations. In DFT, a solution of the Kohn-Sham equations is given for each $\vec{k}$ in the BZ. The sampling of every *k*-point would result in 'infinite' job, and it is not required for a good approximation of the BZ. AIMPRO uses a method developed by Monkhorst and Pack [61]. It chooses a set of 'special' *k*-points for sampling the BZ. A product M_xxM_yxM_z of integers, often

called a grid and chosen by the user, represents three different, usually orthogonal, directions of *k*-points and it allows to cover the whole BZ. In order to get the lowest energy state and a good accuracy, a high number of *k*-points is required although more computational time is needed. The table below shows the convergence of the total energy for the primitive unit cell of graphite (4 atoms) with respect to *k*-point density and computational time. A good balance must be found between decent convergence and the number of *k*-points.

k-points grid	*k*-point mesh density	Total energy (Ha/unit cell)	Time per iteration (s)
2x2x2	2	-22.89826	0.20
8x8x4	40	-22.84591	0.84
12x12x6	126	-22.84600	2.38
16x16x6	216	-22.84595	3.89
24x24x6	468	-22.84595	8.27

Table 3.1: Convergence of a four atom unit cell with respect to the *k*-point mesh and the time required per iteration

The reason why the sampling, in graphite, in the *c* direction is not as important as the other direction is because the lattice parameter is bigger, hence a smaller reciprocal lattice vector in this direction. On the contrary, in the hexagonal basal directions, the reciprocal lattice vectors are bigger, requiring more *k*-points in this direction to broadly maintain the same *k*-point density in reciprocal space.

3.2.2.2 Size effects in Supercell

As mentioned earlier, it is preferable to run a supercell calculation. But the size of the unit cell is important when certain defects are introduced in the solid in order to avoid undesirable interaction between the repeated cells. An easy way to realise if there is an interaction is to increase the size of cell and compare the energies. It would obviously be simple to just use a huge unit cell but the computational cost would largely increase. Another reason why the size of the cell is important is because the concentration must be as close as possible to a real system. If an impurity is less than 1% in a crystal, a unit cell of at least a 100 atoms is necessary. Another group has looked at the effects of unit cell size in well known materials [62]. It was found that a certain size was sufficient enough for a converged geometry optimisation and formation energy, but a much bigger cell was required for calculation of ionisation

levels. Typically in this work, cell of 20–300 atoms have been used.

Chapter 4

Graphitisation

The chapter will essentially focus on the graphitisation process itself and the mechanisms involved instead of the techniques used to describe them. These will be discussed in a later chapter (see chapter 5). Research on the formation of graphite has been an ongoing subject for almost a century and several questions remain to be answered. Many scientists have contributed to understand the chemistry and physics of such a complex reaction and a vast array of information is available. A subset paper related to the work will be introduced here. The figure 4.1 is a simple representation of the high temperature process.

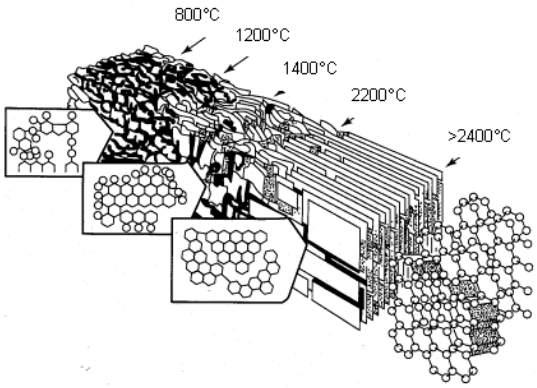

Figure 4.1: Marsh-Griffith Model for the graphitisation process, taken from [63]

4.1 Important definitions

To avoid confusion between the very similar terms used in graphitisation, their definitions are introduced here. They were validated and published by the International Union of Pure and Applied Chemistry [64]:

4.1.1 Graphitic Carbon

"All varieties of substances consisting of the element carbon in the allotropic form of graphite irrespective of the presence of structural defects. The use of this term is justified if three-dimensional hexagonal crystalline long-range order can be detected in the material by diffraction methods, independent of the volume fraction and the homogeneity of distribution of such crystalline domains. Otherwise, the term non-graphitic carbon should be used."

4.1.2 Non-graphitic Carbon

"All varieties of solids consisting mainly of the element carbon with two-dimensional long-range order of the carbon atoms in planar hexagonal networks, but without any measurable crystallographic order in the third direction (c-direction) apart from more or less parallel stacking. Some varieties of non-graphitic carbon convert on heat treatment to graphitic carbon (graphitisable carbon) but some others do not (non-graphitisable carbon)."

4.1.3 Graphitisable and non-graphitisable carbon

"Graphitisable carbon is a non-graphitic carbon which upon graphitisation heat treatment converts into graphitic carbon. Non-graphitisable carbon is a non-graphitic carbon which cannot be transformed into graphitic carbon solely by high-temperature treatment up to 3300K under atmospheric pressure or lower pressure." These terms were introduced by Franklin and were then used by every author [65].

4.1.4 Graphitisation

"It is a solid-state transformation of thermodynamically unstable non-graphitic carbon into graphite by means of heat treatment. Graphitisation is also used for the transformation of metastable diamond into graphite by heat treatment, as well as in metallurgy for the formation of graphite from thermodynamically unstable carbides by thermal decomposition at high temperatures. Such uses of the term graphitisation are in line with the above definition. The use of the term graphitisation to indicate a process of thermal treatment of carbon materials at T>2500K regardless of any resultant crystallinity is incorrect." Note: The first line of this definition describes the process studied here.

4.1.5 Carbonisation

"It is a process by which solid residues with increasing content of the element carbon are formed from organic material usually by pyrolysis in an inert atmosphere. Carbonisation is a complex process in which many reactions take place concurrently such as dehydrogenation, condensation, hydrogen transfer and isomerisation. It differs from coalification in that its reaction rate is faster by many orders of magnitude. The final pyrolysis temperature applied controls the degree of carbonisation and the residual content of foreign elements."

4.1.6 Catalytic graphitisation

"It refers to a transformation of non-graphitic carbon into graphite by heat treatment in the presence of certain metals or minerals. Catalytic graphitisation gives a fixed degree of graphitisation at lower temperature and/or for a shorter heat treatment time than in the absence of the catalytic additives (or a higher degree of graphitisation at fixed heat treatment conditions). Often it involves dissolution of carbon and precipitation of graphite at the catalyst particles so that non-graphitising carbons can be graphitised by this procedure."

4.2 How to make graphite

The process of making graphite was discovered around 50 years before its crystal structure. It was first synthesised by Edward Goodrich Acheson by heating silicon carbide (SiC) to high temperature. The range of carbon based materials, used as starting materials to form graphite or partially graphitised carbon under high temperature is wide. However the initial product used should be relative to the final product required. Some materials are contaminated with impurities and they can have undesired effects during the process. To produce blocks of graphite for nuclear reactors, coke particles, derived from petroleum (figure 4.2) and coal tar pitches, are often used as fillers. They are used to avoid volatiles, which can introduce the formation of distortions or cracks. Pitch is used as a binder because it gives a residue similar to cokes after carbonisation. The controls of the particle size of the filler and the mixing ratio of the filler to the binder are of great importance depending on the material application. However let us not forget that not every graphitisation is intended for nuclear purpose and many experiments use other starting materials. Over decades, researchers have looked at different materials to understand the process. They tried to investigate why certain materials can graphitise and others cannot. Some questions are still unanswered but it is well understood that the precursors used predetermine the characteristics of primary carbonisation and the later processes. In the following, the different graphitisation precursors and their behaviour are discussed with reference to key publications in the development of this science.

Figure 4.2: Picture of a petroleum pitch coke

4.3 Graphitisable carbons versus non-graphitisable carbons

From the definition in 4.1.3, we understand that temperature is not the only factor that allows a material to graphitise. Different precursors show different properties at the same temperature (figure 4.3). They tend to be divided into two categories after they undergo pyrolysis. Only some materials will be discussed with a clarification on why they have the capability to graphitise or not. The pioneer in this field was R.E. Franklin and a summary of her studies on graphitisation can be found in her paper for the Proceedings of the Royal Society, published in 1951 [66].

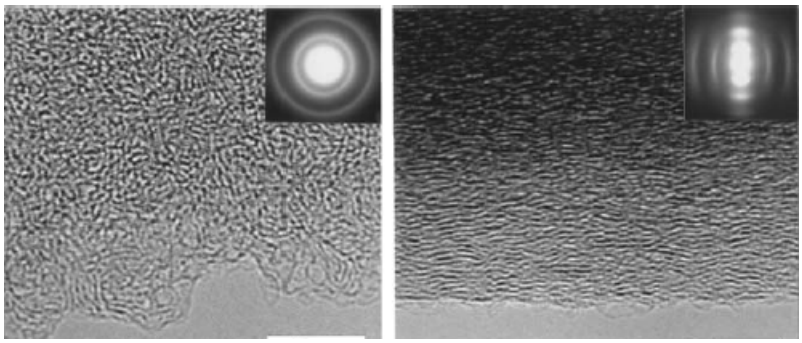

Figure 4.3: High resolution transmission electron microscopy (HRTEM) image and their selected area diffraction (SAD) patterns of two different carbons heated to the same temperature: left) sucrose, right) anthracene, taken from [67].

4.3.1 The different precursors

Coal had a big impact on Britain's economy during the second world war and a lot of work was attributed to it. It is a solid but brittle carbonaceous black sedimentary rock but it can also be synthesised. It contains mostly carbon but has impurities such as hydrogen, oxygen, nitrogen and sulphur. All coals are porous to different extents and many of their properties depend on it. In 1949, experiments demonstrated that coal was acting like a molecular "sieve" [68]. Franklin *et al.* calculated that the density of a coal of zero hydrogen would be 1.85 g/cm^3 and arrived at the conclusion that coals cannot be graphitic in nature. The different types of natural coal are shown in table 4.1. Anthracite is the hardest with high carbon content.

Not all coals are graphitisable and this usually depends on their carbon concentration. Anthracite, for example, is used as a precursor for nuclear purposes. Petroleum is a

Types of coal	Carbon %
Lignite	25-35%
Sub-bituminous	35-45%
Bituminous	45-85%
Anthracite	85-95%

Table 4.1: The four types of Coal [69]

natural complex mixture of various hydrocarbons with a vast number of impurities. It has a carbon concentration between 80–90%, hydrogen between 10–20%, oxygen, nitrogen and sulphur are usually <2% but sulphur can sometimes be higher. It is used in many industrial applications such as fuels, lubricants and other. Asphalt, also known as bitumen, is a form of petroleum which is used to form the pitch for the binder. These forms of carbon are considered graphitisable carbon. They are precursors used for nuclear graphite but many other materials can graphitise. A short list of graphitising and non-graphitising carbon is shown in table 4.2.

Graphitisable	Non-graphitisable
Petroleum Coke	Most Resin
PVC (polyvinylchloride)	Saran (polyvinylidenechloride)
Pitch coke	Cellulose
Coal Tar pitch	Coal (83.1% C)
...	...

Table 4.2: Classification of the graphitising and non-graphitising carbons according to references in this chapter.

Most resins, from plants (e.g. trees), are declared as non-graphitising carbon but they can be used to make pitches, thus indicating that not all pitches are graphitisable and confirming the importance of the precursors.

4.3.2 Pyrolysis

Pyrolysis is a thermolysis of organic materials. In other words, it is a chemical decomposition caused by heat. The process is irreversible and usually produces gas and liquid, leaving solid residues richer in carbon content, char or coke. Carbonisation is the result of high temperature pyrolysis with carbon residue above 90 wt.% at 1400 °C and ~ 99 wt.% at 1800 °C. Char is a solid decomposition product of an organic material -synthetic or natural- resulting from a precursor which has not passed through a fluid stage. The shape of the char would be similar to the shape of the precursor but smaller

in size. It cannot be transformed into crystalline graphite even at temperatures around 3000 °C. For example, sugar melts and then polymerises to produce chars. Charcoal is the term used for char obtained from wood, peat or coal. Coke, in contrast, is a solid product which has passed through a liquid or liquid crystalline state during pyrolysis (or carbonisation). It is in a non-graphitic state which has the ability to graphitise around 2200 °C. The term coke can sometimes be used to describe a graphitisable carbon before the beginning of graphitisation. This indicates that the result of a pyrolysis from organic materials is the first stage that will indicate if a precursor is a graphitising carbon or a non-graphitising carbon. Pitch is also a residue from pyrolysis which is solid at room temperature and is mainly made up of aromatic hydrocarbons and heterocyclic compounds. It originates from different treatment of different precursors. They have a broad softening range (600–900 °C) depending on their compositions, and when cooled, they solidify without crystallization. For example, petroleum pitches are obtained by treating the residues of refinery distillation. Tar is a by-product from the coke production and can be obtained from either coal or petroleum. Tar is sometimes confused with pitch although tar is more liquid and pitches can be made from tar (e.g. coal-tar pitches).

4.3.3 Structure of non-graphitising carbon

Franklin gave her understanding of why such products could be classified into two categories. She started by stating that non-graphitising carbons contained a lower concentration of hydrogen and a higher concentration of oxygen. During the process this class develops, at low temperature, cross-linkers between small crystallites which prevent them to move and to rearrange themselves at a later stage. The final structure is hard, shows a high amount of large porosity and no sign of large crystallite structure (usually coherence lengths no more than ~ 70 Å) even when the temperature has exceed 3000 °C. In contrast, the concentration of hydrogen is more important in graphitising carbons. The cross-linkers formed at the early stages are weak and do not interfere in the mobility of the small crystallites. The porosity is minimal and large crystallite structures are already visible at around 2000 °C. Her conclusion is that crystallite growth depends on the rearrangement of whole layers together

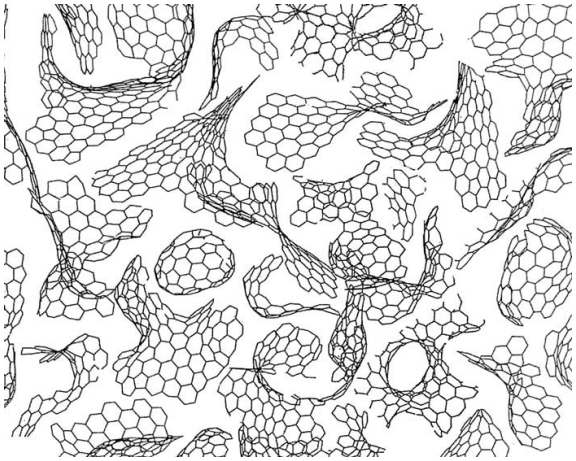

Figure 4.4: Harris's proposed structure for non graphitising carbons, taken from [72]

and not by isolated atoms or small group of atoms. The theory of the existence of small crystallites containing a few layer planes which are joined together by cross-links was also described by Oberlin [70]. Although the process cannot be refuted, the theory is weakened by the unspecified nature of the cross-linkers. Some work, using lattice-imaging electron microscopy, proposed structures constructed from curved sheets of graphite made of hexagonal rings enclosing voids [71]. This proposed structure was also rejected, due to their ability to fold strongly together in order to reduce surface energy at higher temperature [72]. The presence of sp^3 carbons was rejected due to their propensity to become sp^2 at temperatures around 1700 °C (transformation of diamond to graphite). Another theory had to be found. The discovery of fullerenes in 1985 and the new improvement in transmission electron microscopy (TEM) opened new perspectives for the structure of non-graphitising carbon.

Using high resolution TEM, Harris *et al.* showed the presence of closed structures (hollow nanoparticles) in non-graphitising carbon heated up to 2300 °C [73]. They believed that non-graphitizing carbons contain pentagonal carbon rings (in high concentration), as well as other non-six-membered rings, forming lots of fragments instead of continuous sheets. The conclusion of his paper suggests that fullerene-like structures (as shown in figure 4.4) are the reason some carbons can graphitise and others cannot. Zhang *et al.* used electron energy loss spectroscopy to show the presence of curved layers containing fullerene-like bonds, which are critical for the formation of closed porosity within the structure and find agreement with the structural model

for non-graphitising carbons proposed by Harris *et al.* [74]. The broad overview given above, of the possible structures established for non-graphitising carbon, can be summarised with general rules. Apart from few exceptions (e.g. anthracites) non-graphitising carbons tend to be:

- Hard
- Low density materials
- Microporous structures
- High in Oxygen/Sulfur (cross-linkers)

They are of great interest due to their ability to produce activated carbon. These types of carbon are used in water purification, metal extraction, medicine and many other applications [75].

4.4 The first and second carbonisation

In the previous sections, the result of pyrolysis on different organic materials was reviewed and it was shown that pyrolysis is a major step for the rest of the graphitisation process. In fact, the degradation of organic materials correspond to the formation of aromatic molecules and a release of volatiles while the carbon content of the residue increases. The chemistry and the molecule/crystallite shapes involved from 300 °C up to 2000 °C is discussed here. For lower temperature, an extensive review written by Richter and Howard on the formation of polycyclic aromatic hydrocarbon (PAH) could be an attempt to describe the process [76]. Even though the optical anisotropy of coke was first described around 1930, it is only later that Brooks and Taylor recognized the development of mosaic structures during this stage [77]. They reported the appearance and growth of spherical bodies in the plastic carbonaceous material. The spheres have an initial size of ~0.1 μm and can expand to 2 mm with further heating (figure 4.5). They are mainly made of aromatic compounds. The same group later found that every graphitising carbon from different precursors form similar mosaic structures composed of these spherical bodies, but their nature and their growth modes are different.

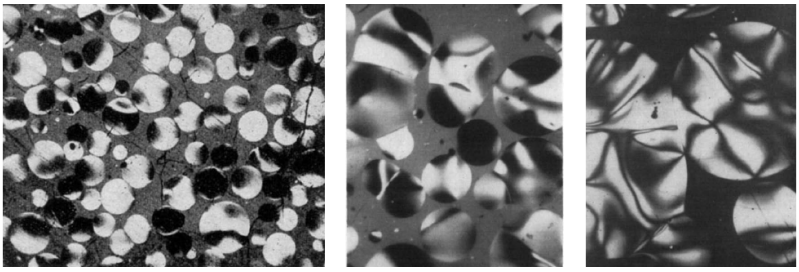

Figure 4.5: Spherical bodies during the mesophase, taken from [77, 78]

In order to understand what happens, it is crucial to remember that the molecules in the precursors are constituted of aromatic rings. The growth of the spheres begins at a temperature where the materials are in the liquid phase or in the mesophase (transition between liquid and solid phase). A general path is that mesophase spheres appear at the temperature for which viscosity is at a minimum, but still in a plastic phase. They merge and form a bulk mesophase (right picture in figure 4.5). The aromatic hydrocarbons in a typical coal tar pitch vary in molecular size and shape. They can have alkyl side chains and contain heteroatoms such as nitrogen and sulphur. Edstrom and Lewis studied a large number of polynuclear aromatics and stated that the steric conformation and planarity of the starting material influenced the structure of the final carbon and graphite [79]. Other experiments showed that these properties only apply to a limited group of intermediate molecules or to free radicals when they reach the size of several rings [80]. To elucidate the process, researchers concentrated their effort on the polymerisation process. It seemed obvious to them that small aromatic structures are polymerised to produce bigger ones which ultimately achieve the three dimensional order of graphite. Lewis explained that the polymerisation process goes through stages which may or may not be simultaneous: C-H and C-C bond cleavage to form reactive free radicals, molecular rearrangement, thermal polymerization, aromatic condensation and elimination of side chains [81]. The number of polymerisation sites in an aromatic molecule makes the carbonisation process really complex to understand. Some experiments give an idea of the possible mechanisms for the polymerisation process of anthracene, one of the many PAH compounds [82]. Experiment on the spheres before their coalescence, using dark field (DF) TEM, showed that aromatic molecules stack together and can have a range of interlayer spacings of around 3.44 Å in soft carbons. These values can be considerably

increased when a char is studied [83, 84]. From the DF images, it was calculated that the aromatic molecules' mean diameter and thickness are about 8 Å. This means the molecules at this stage have less than 10 aromatic rings (e.g. ovalene) and form no more than three layers before the semi-coke stage. This was called the Basic Structural Unit (BSU) by the authors and the term BSU is now widely used. It should be noted that the semi-coke stage still contains volatiles and is just the result of an incomplete carbonisation. The polymerisation process described above carries on. A computational study was performed for polynuclear aromatic hydrocarbon molecules in pitches such as ovalene and coronene using molecular mechanics [85]. They looked at possible configurations for BSU. It was found that homogeneous and heterogeneous dimer or trimer clusters have a strong preference for face-to-face orientation. They form a parallel stack with layers shifted with respect to each other like in normal graphite. The interlayer spacing between layers is 3.4 Å on average. Interestingly, if a fourth layer is added, it will prefer to orient perpendicular to the stack such that its face is against the edge of the stack.

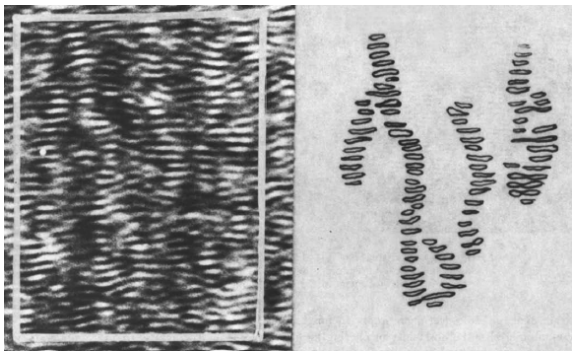

Figure 4.6: Lattice fringes after spheres coalescence (left) and LMO columns (right), taken from [86]

When the BSUs coalesce, it is found that a structural disorder suddenly happens so the peculiar short range order is destroyed and replaced by a nematic order before it gets restored [87]. The bulk mesophase is thus made of BSUs orientated nearly parallel. They begin to form columns which are not coherent with each other and the distorted piles of molecules are in complete disorder, this is called the local molecular orientation (LMO). The two pictures, figure 4.6, show the appearance of LMOs. The bulk mesophase remains viscous to around 1000 °C until, with loss of more volatiles, it forms green coke, which is the first solid product of the carbonisation. This is the

end of the first carbonisation and the beginning of the second carbonisation starts. All the light molecules have disappeared but the BSUs are not free of edge groups. The second carbonisation is expected to end at around 2000 °C. This stage can be described as a growth of the layer diameter which can be determined by either the size, the shape, the crystalline order or the arrangement in space. It is often seen as two distinct steps: the formation of small columns of fringes which trap a single disorientated BSU between them (up to 1500°C) and the formation of stacks of distorted layers in a zigzag shape after BSUs disappear. Different techniques are used and each of them provides different information regarding the crystallites (see chapter 5). Many measurements on many different graphitisable carbons were studied and they all show a similar behaviour. Emmerich studied the evolution of the crystallinity in carbons with heat treatment [88]. He showed that the growth of the size of the crystal happens by a small in-plane growth of crystallite, followed by the plane coalescing along the *c*-axis and finally by the coalescence of crystallites along the *a*-axis. The latter can often happen in the final stage (see section 4.5). Figures 4.7 shows lattice fringe TEM images and represent the growth of the layer in the *a* direction and the stacking ordering. The evolution with HTT of the number of crystallites and the total volume occupied by the crystallites was determined. From an atomistic point of view, it starts with the release of heteroatoms and makes the lattice vulnerable to impurity effects [89]. The formation of dangling bonds is expected and only then BSUs can start to rearrange together and form distorted layers. These distorted layers can form pores and these pores can often trap molecules. With higher temperatures, the distorted layers become more and more flattened. Some remaining defects are removed. The process ends when most of the physical properties change/appear. The materials go from brittle to ductile. Finally, the second carbonisation stage is sometimes seen as if each layer is similar to a crumpled sheet of paper which then partially or totally becomes flat (non-crumpled). So the carbonisation process cannot be described without taking into account the progressive association of more and more neighbouring elementary domains for the crystal growth.

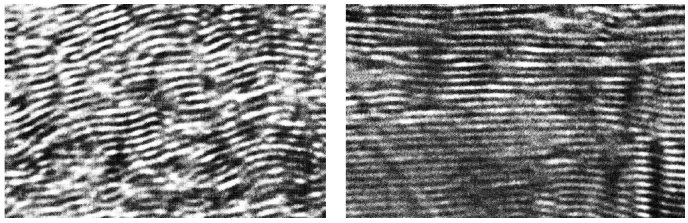

Figure 4.7: TEM image of: left) the distorted layers, right) Almost perfect flat sheet, end of second carbonisation, taken from [83]

4.5 The final step: Graphitisation

The final ordering of the planes occurs in the stage called 'final graphitisation'. Depending on the material and the method of graphitisation used, this stage might not be necessary. It can reach temperatures of up to 3500 °C if required. If there are any twist boundaries between the layers, the final high temperature treatment would reorientate the boundaries (figure 4.8) and allow the interlayer spacing, d_{002}, to decrease from 3.44 Å to 3.37 Å. In the graph of figure 4.9, there is an inflection point near 2100°C representing the polygonisation and sudden perfection of graphite sheets. It should be pointed out that the natural graphite value, 3.354 Å is never obtained. Quite often this stage shows an important growth in the plane direction.

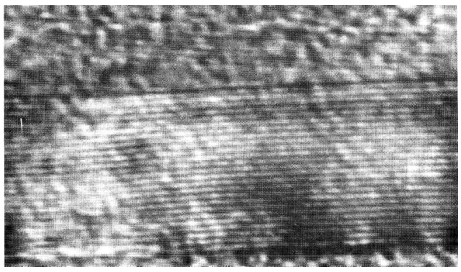

Figure 4.8: Graphitised carbon at 2900 °C, taken from [83]

For further detail the reader is directed to an excellent review of the carbonisations and the final graphitisation written by Oberlin [22]. The interlayer spacing is often used to establish the completion of the graphitisation and authors use different mathematical relationships to express their results.

4.5.1 The graphitisation order

After Franklin's discovery, a lot of effort was put into finding a relationship between the experimental value of the interlayer spacing d_{002} and the "ordering parameters". Several authors have introduced different terms to correlate them and the most common ones are reviewed:

1) p = the probability that two neighbouring layer planes are disorientated with respect to each other is deduced from the equation:

$$d_{002}(\text{Å}) = 3.440 - 0.086(1-p^2)$$

where 3.440 Å is the interlayer spacing for non-graphitic graphitising carbon. The idea is that the average value d_{002} lies between 3.354 Å (highly crystallized graphite) and 3.440 Å. An intermediate spacing value of 3.397 Å for disorientated layers sandwiched between orientated layers is also considered. The 0.086 coefficient is just the subtraction of the two extreme values [65].

2) P_1 = the probability that the graphite orientation is between two neighbouring layers planes. Here, each pair of nearest neighbour layer planes reorders separately from others neighbouring layers [90]. P_1 is calculated using the equation:

$$d_{002}(\text{Å}) = P_1 a_3 + (1-P_1)a'_3$$

where a_3=3.354 Å and $a'_3=a_3(1+Z_1)$ (where Z_1 is the distortion in a_3 produced by the presence of distorted layers planes, this equation can become:

$$d_{002}(\text{Å}) = 3.440 - 0.086P_1$$

if a_3=3.354 Å and a'_3=3.440 Å [90]. P_1 should be measured by hk band modulations. The table 4.9 below is taken from reference [25] and shows the experimental correlation between d_{002} and the probability P_1 for different starting materials.

3) g = the degree of graphitisation, a coefficient measuring the fraction of carbon layers modified by the graphitisation process with a spacing of 3.354 Å [91]. A partially graphitised carbon consists of graphitised and non-graphitised layers. Thus the idea of the graphitisation of the stacks of layers is replaced by the idea of graphitisation of the elementary layers. The coefficient g measures the fraction of carbon layers modified

by the graphitisation process and having a spacing of 3.354 Å. This coefficient is deduced from a measurement of d_{002} [91].

$$d_{002}(\text{Å}) = 3.440 - 0.086g$$

Maire and Mering, from an x-ray investigation of polyvinyl chloride char, suggested that the probability P_1 is related to g by the relation $P_1=g^2$. It was shown later this equation is only valid for PVC. Thrower suggested that g should not be used as it is just confusing and another way to describe the other definitions [92]. If the first two methods are compared, it is obvious that a problem arises. Their definitions mean that $P_1=1-p$, whereas their equations suggest that $P_1=1-p^2$. One difference between the two equations is that Franklin introduces a third possible spacing (non-linear relationship) while Houska uses only two (linear relationship) [65, 90]. It should also be considered how these parameters are obtained, either from the modulation of the *hk* bands or from the mean interlayer spacing.

4.6 Induced graphitisation

4.6.1 Catalytic graphitisation

Quite often, catalytic graphitisation tends to have a consequential amount of residual catalytic material which is not convenient for industrial purposes. Nevertheless,

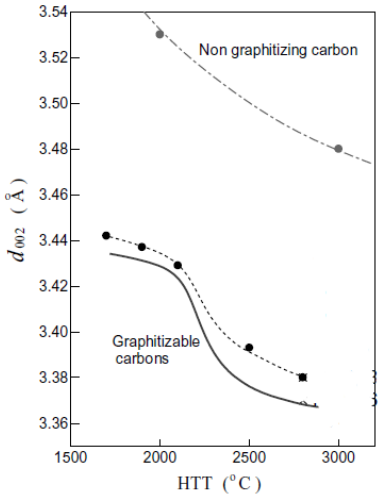

Sample [Ref]	d_{002} min., Å	P_1 max.
Saccharose-based	3.43	0
R 15769 (Asphalt)	3.43	0
Athabasca 2 IC_7	3.42	0
Athabasca 1 IC_7	3.42	0
Boscan IC_7	3.41	0
Orenoque IC_7	3.41	0.1
R 31500 IC_6	3.40	0.2
Athabasca IC_7	3.39	0.2
Emeraude IC_7	3.39	0.3
Anguille IC_7	3.39	0.4
Batiraman IC_7	3.38	0.5
Mandgi IC_7	3.38	0.6
Safaniya IC_7	3.38	0.6
Lacq Sup IC_7	3.37	0.6
Grenade IC_7	3.37	0.7
Minas IC_7	3.37	0.7
Safaniya IC_5	3.37	0.7
Light Arabian IC_7	3.37	0.8

Figure 4.9: Left: The d_{002} decrease in the final graphitisation, right: the degree of graphitisation of some carbon materials, taken from [25]

if the graphitisation temperature can be decreased, or a more perfect polycrystal can be manufactured with help of a catalyst, it can certainly have a great impact. The additional metals are not the only parameters to influence the process and other experimental conditions such as the type of carbon (graphitisable or non-graphitisable), the particle size, the catalyst concentration as well as its structure (i.e. the element or one of its compounds) and the temperature treatment should always be considered. The aim here is not to discuss every possible metal catalyst: one of the first reviews [93] and another later [94] give a broad overview of those. Instead, we will summarize their catalytic effects. Oya and Marsh divided them into four different categories but we will regroup them in three [95].

- The G-effect:

  A d_{002}-spacing of approximately 335.4 pm and a crystallite height L_c above 50 nm inside a usually non-graphitising carbon can be obtained. One of the principal catalysts is iron.

- The T_S effect:

  A turbostratic carbon is obtained here with a d_{002}-spacing around 340.0pm and L_c approaches a few nanometres. The structure is not changed even with further heating. One of the metals is nickel.

- The A effect and the T_N effect:

  A more homogeneous crystal with various values of d_{002} is obtained. The in-plane defects within the crystallites hinder the growth. The catalyst (e.g. boron) reacts with these defects and allows some rearrangement in the A effect. In the T_N effect, the catalyst (e.g. calcium and magnesium) react with cross-linkers between layers.

4.6.2 Graphitisation under pressure

Man-made graphites are always less crystallised than natural graphite because natural single crystal graphite undergoes a preliminary strain in carbonaceous rock by tectonic stresses. It is produced at temperatures between 300 °C and 500 °C and pressures of

400 to 500 MPa [96]. Experiments under pressure or/and stress have been carried out in order to reproduce the natural environment. It was first reported that graphitisation under reduced pressure or in vacuum increases the temperature for the rearrangement of the layers and also the interlayer spacing [97]. The same authors then showed that high pressure accelerate the process. Pressure of 1 GPa lowers the graphitisation temperature, remarkable changes appear around 1500 °C and even a non-graphitising carbon reaches its 'graphitised' structure at a temperature lowered by 1000 °C compared to normal [98]. In another experiment and under a different pressure (500 MPa), non-graphitising carbons showed an intermediate phase (turbostratic) at 1100 °C with an increase of these structures until 1600 °C [99]. When heat-treated under the same pressure but at higher temperature, this phase is suddenly transformed into graphite.

4.7 Manufacturing Process for nuclear purpose

Here the steps involved in graphite manufacture are reviewed, with a nuclear graphite used as an example. The raw materials and pitch binders are combined together to form a homogeneous mix, usually at a temperature up to 150 °C. The raw coke is then calcined to 1300 °C for a few hours. Some impurities are removed and the material develops a small crystal structure. By crushing the mixture, a range of particle sizes are formed and fine 'flour' grains are mixed with larger grains and coal-tar pitch at temperatures up to 170 °C. Different methods are used to extrude the new mixture. This process introduces a preferred orientation in the product. This is due to the anisotropy of the graphite lattice. One of the longest steps (~ 4 weeks) is the baking process which goes up to 1000 °C in order to convert the binder pitch to coke. Some of the gaseous volatiles are removed. The resulting carbon block is mostly amorphous carbon (~ 1.55 $g\,cm^{-3}$ density with porosity of about 25%) [100]. Baking is followed by pitch impregnation. It can often be rebaked in order to improve some properties, notably density. The next step is the final graphitisation. The material is heated in an Acheson type furnace. It requires electrical heating in the absence of air to temperatures in the range of 2600–3000 °C for approximately four weeks, followed by slow cooling over several days. The final step is the purification either by chemical

or thermal purification. Chemical purification involves heating the graphite blocks in a halogen atmosphere. This removes impurities such as rare-earth metals, vanadium, and boron to less than 20 ppm. The figure 4.10 represents the process in a simplistic way.

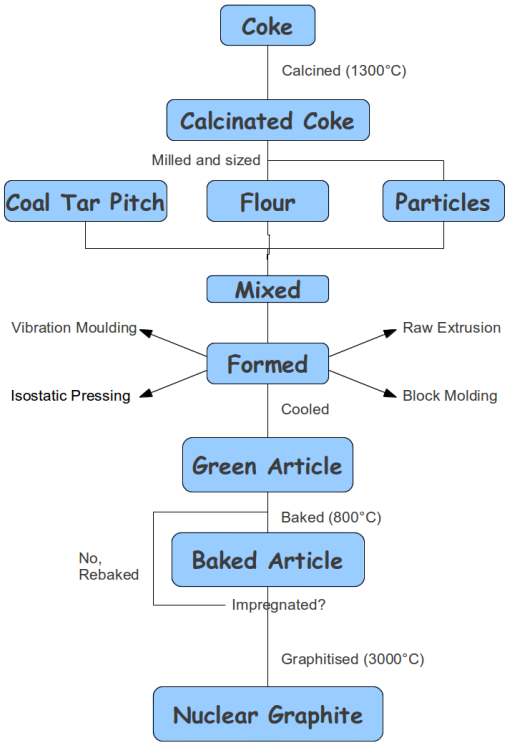

Figure 4.10: Manufacturing process

Chapter 5

Experimental techniques to evaluate graphite crystals

Structures of carbon materials have been characterized by many different experimental techniques. Throughout the graphitisation process, graphite has been studied via x-ray diffraction (XRD), transmission electron microscopy (TEM) and Raman spectroscopy. Some other techniques such as infra-red (IR) and electron spin resonance (esr) were also used but only for specific stages of the process. Much information on the structure and evolution of the materials can deduced from these techniques. They give access to important parameters which reveal how perfect, or not, a graphite crystal can be. The aim of this chapter is to summarise some of the main techniques, discussing their pros and cons and by relating them to some of the experimental works.

5.1 Diffraction

Wide angle x-ray diffraction is one of the quickest, easiest techniques and also the most applied technique to characterise the crystal structure. It is a simple way to measure the interlayer spacing d_{002} and the coherence lengths L_c and L_a. To obtain these, an x-ray diffraction pattern of graphitic carbons gives distinct reflections of the (00l) and (hk) bands, but unfortunately non-negligible final value errors -up to 20%- can result if approximations are made or careful measurements are not carried out.

Historically, it all started when a group of workers passed beams of x-rays through crystals. They discovered a pattern of dark spots on a photographic plate placed behind a small crystal [101]. A theoretical approach to these patterns was introduced by the Bragg's equation [102]:

$$2d \sin\theta = n\lambda$$

where d is the interplanar distance, θ is the scattering angle, n an integer and λ the wavelength. This equation is still used nowadays. Later, Scherrer studied the effect of crystallite size on the width of x-ray diffraction peaks [103]. He postulated the equation:

$$L = \frac{K\lambda}{B\cos\theta}$$

where L is the crystallite size, it is usually referred to the direction perpendicular to the lattice planes (i.e. L_c for the 002 peak), K is a numerical factor frequently referred to as the crystallite-shape factor (~ 0.9 when calculating L_c), λ is the wavelength of the x-rays (usually CuKα_{1+2}=154.18 pm is used), B is the full width at half-maximum intensity of the x-ray diffraction peak and θ is the Bragg diffraction angle. The measurement of the peak is taken from the lines (002) and (004) therefore L_c must be written following the Miller indices (i.e. L_c(002) and L_c(004)). It should be pointed out that Scherrer's equation can only be applied for average sizes of 100 nm, because diffraction-peak broadening decreases with increasing crystallite size, and the difficulty arises from separating the peak broadening due to crystallite size from the broadening caused by to other factors [104].

Diffraction study can be divided into two categories: single-crystal and poly-crystals. All the references cited later are for experiments carried on powder (poly-crystals).

Warren made a big contribution in the carbon field with x-ray diffraction. He demonstrated the distribution of atoms can be determined directly from the experimental scattering curve using Fourier integral analysis and recognised the existence of aromatic layers in carbon black [105, 106]. In 1941, in a study of random

layers lattice structure and using Scherrer's equation above, he was able to find an equation for the size of the two-dimensional layer:

$$L_a = \frac{1.84\lambda}{B\cos\theta}$$

The (100) and (110) lines are used to determine the L_a parameter. And the following year, Biscoe and Warren looked at the diffraction pattern of a coke heat-treated at 1000 °C. The pattern showed a broad (002) peak and the appearance of a small 004 peak. They introduced the term 'turbostratic carbon' for graphitic carbons. From the paper they define turbostratic as: "*each group consisting of a number of graphite layers stacked together roughly parallel and equidistant, but with each layer having a completely random orientation about the layer normal*" [10]. The broadening of the diffraction lines is due to the small size of crystallites, but can also come from strain and defects of the lattice. Warren's equation was confirmed and proved to be valid for layers with a diameter as small as 16 Å [107].

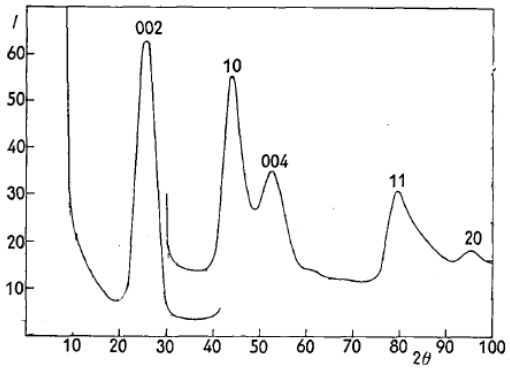

Figure 5.1: Computed diffraction pattern for the parallel-layer group size L_a=20 and L_c=13.8 Å, taken from [108]

Other methods of calculating the integral breadths of Debye-Scherrer lines was subject to some research [109] and Bacon used these variants to explain that if the carbon layers are assumed to be of infinite horizontal extension; it can be shown that the line widths B are given by [110]:

$$B = \frac{\lambda \sin\alpha}{L\cos\theta}$$

where α is the inclination to the horizontal of the normal to the (hkl) planes, all other terms are the same as above. He correlated the value of d_{002} with the thickness of

the crystal. It should be noted the Stokes' method used by Bacon requires careful evaluation of the tails of the peak and the background.

Finally, Houska and Warren explain that if there are modulations (i.e. not a single peak) in the (*hk*) bands, the value obtained for L_a cannot be considered as accurate and a certain correction must often be applied [90, 111, 112]. They also suggested that layer thickness L_c cannot be obtained from the (00*l*) peaks without first correcting for the distortion broadening due to the existence of two different layer spacings corresponding to ordered and disordered pairs. Following Houska's work, Bouraoui *et al.* showed that L_a was related to the index of the (*hk*) band [113]. They consider L_H as the length of an (*hk*) band such that $H = h^2 + k^2 + (hk)^{1/2}$. The figure 5.2 from Bourauoi's paper is an example of their method.

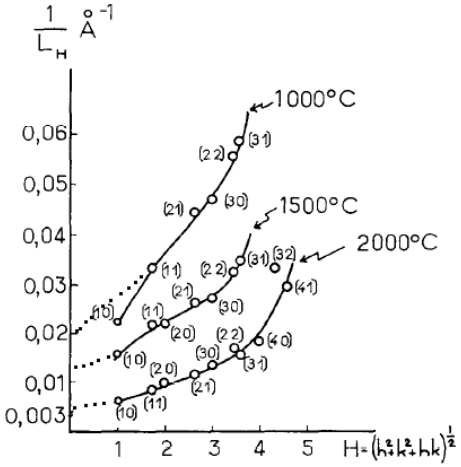

Figure 5.2: Determination of L_a with Bouraoui's method, taken from [114]

X-ray diffraction techniques are also used to find the graphitisation order presented earlier (see section 4.5.1).

5.2 Spectroscopy

5.2.1 Raman

Raman Spectroscopy is another method used to look at graphite crystal structure. The technique was discovered a few years after x-ray diffraction but the lasers available were not suitable for black materials. One of the first pieces of experimental work was carried out in 1970 and it was reported that graphite single crystals show one

single line at 1575 cm^{-1}, which is linked to the E_{2g} vibrational mode [115]. For polycrystalline graphites, another line appears at 1355 cm^{-1} which is attributed to defects in the crystal and is named the D mode. The intensity ratio of these two peaks is directly connected to the size of the crystal and it allows the measurement of L_a in a thin surface layer of any carbon sample. Raman spectroscopy can be divided into two different orders, the first and second order. Tuinstra calculations were only first order [115].

The second-order Raman spectra results from double-resonant Raman scattering by two phonons instead of a phonon and a defect [116]. Later, another group showed that second order Raman spectra exhibit an anomalously sharp feature at an energy higher than twice the energy of the first order Raman line [117]. The same group related the first- and second-order Raman features of graphite [118]. There is a strong sharp feature at 1581 cm^{-1} as the high-frequency E_{2g} first-order mode described before. The low-frequency E_{2g} mode which occurs at 42 cm^{-1} is the interplanar 'rigid-layer shear' mode and is only obtained with special techniques. The continuum scattering from 2200 to 3250 cm^{-1} represents the second-order and exhibits three distinct groups of bands; a dominating band near 2710 cm^{-1} named D* and two weaker features observed at 2450 and 3250 cm^{-1}. It becomes apparent that the D* feature is very close to twice the D mode energy and is due to an overtone. Wang *et al.* gave evidence for the D mode's intensity dependence on any kind of disorder or defects using boron-doped and oxidized highly ordered pyrolytic graphite [119]. When defects/disorder are present, the D^4_{6h} symmetry is broken and it causes all the vibrational modes to contribute to the Raman scattering; hence the appearance of new bands and the broadening of some observed bands [120]. Finally, Vidano found that certain Raman modes' frequencies can depend on the energy of the incoming laser light, while modes for perfect graphite do not vary, the modes for disordered structure can shift [121]. This technique can be applied to graphitising and non-graphitising carbons and correlation with polyaromatic hydrocarbons can be obtained [122]. Another group described a sharp peak at about 464 cm^{-1} and broadened peaks in the range 75–210 cm^{-1} as evidence for the presence of fullerene-like elements in non-graphitising carbon as described earlier in section 4.3.3 [123]. Analysing disordered and amorphous carbon, Ferrari *et al.* accounted the G peak as the relative motion of sp^2 carbon, and the D

peak to the breathing modes of the rings. They classified all the available visible Raman data by defining three stages from perfect graphite to tetrahedral amorphous carbon [124]. Stage 1 is from graphite to nanocrystalline graphite, stage 2 is from nanocrystalline graphite to amorphous carbon and stage 3 is from amorphous carbon to tetrahedral amorphous carbon.

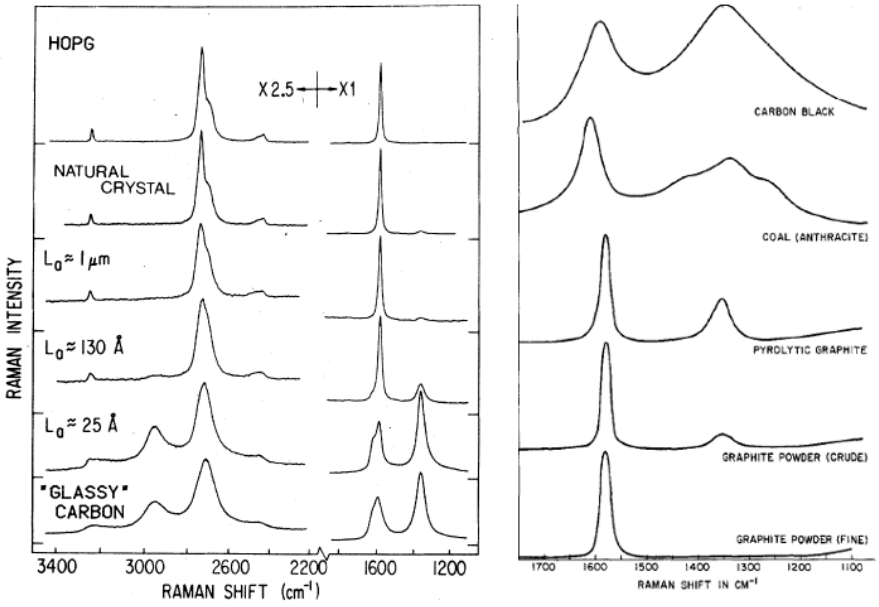

Figure 5.3: Raman spectrum at different L_a, taken from [118]

5.2.2 Infra-red (IR)

Infra-red has never been a predominant technique for studying graphite. Nevertheless, it has been used for just one purpose, which is to present the residual concentration of various chemical groups during the first carbonisation. Rouxhet studied the main chemical modifications taking place in the pyrolysis of kerogens [125]. The process, in this order, is as follows: removal of carboxyl and carbonyl groups, removal of saturated hydrocarbon groups, formation and removal of aromatic CH. IR also gives information on carbons from highly oxygenated precursors which form products with a high concentration of C-OR functions. The evolution of the aromatic CH is an indication of the involvement of free radicals (detected by esr).

Note

There has been a reconsideration of the relationship between the crystallite size L_a of carbons determined by x-ray diffraction and Raman spectroscopy [126]. This concluded that the measurement of the size of a carbon crystallite, L_a<2 nm, using the I_D/I_G form and by applying Tuinstra correlation is incorrect.

Another advantage of these techniques is that they can be associated together. Since materials properties in carbon depend on their microstructures and techniques such as diffraction or spectroscopy do not give enough local detail, being spatial average, other techniques such as microscopy can be used.

5.3 Microscopy

Carbon materials can be poorly organised and microscopy is a powerful tool as an imaging or analytical technique. Its main interest is to study the relation between structure and physicochemical properties. In this section, only transmission electron microscopy (TEM) is discussed as it has been an important technique to interpret graphitisation. To understand TEM imaging, the reciprocal space of each structure should be well understood. Details about the reciprocal space structure are given in the appendix A. This technique has the ability to perform a double Fourier transform from real space to reciprocal space and back to real space again. TEM images can be divided into several categories but only lattice fringes images, dark field images and selected area electron diffraction are reviewed below. The two main (*hkl*) orientations are the (110) and (002).

5.3.1 Lattice Fringe (LF) TEM

From a (002) lattice fringe (LF) micrograph, the length of a set of perfect or distorted fringes and the number of them in a stack can be measured. In order to get relatively accurate measurements, it is necessary to know the value of the parameters involved (e.g. magnification) and for further detail the reader is directed to an excellent review [127]. For graphitic materials, the resolution of the TEM has, until recently,

limited the images to the 002 fringes. The only part of the carbon layer shown on an image is the one which nearly fulfils the (002) Bragg condition (0.29 ° at 120 kV) [70]. If a layer is distorted then the image disappears. Many authors attempted to find a model entirely based on images but the models were found to be unreliable [70]. Lattice fringes images have been presented in figures 4.6 and 4.7 in chapter 4. They are very helpful to see the evolution of the layer stacking throughout graphitisation.

5.3.2 Selected Area electron Diffraction (SAD)

In TEM, there is the possibility to choose another mode: Selected Area electron Diffraction. It allows to select a diffracting area with less than 1 μm in diameter. If the scattering domains are distributed at random in the material, the SAD pattern is similar to an x-ray powder diffraction pattern. Therefore this technique can be used early in the process to detect single BSU and LMO [25]. Three different orientations can be chosen for SAD; the orientation can be parallel (i.e. edge-on, orientation P_1), perpendicular (i.e. face-on, P_2) or oblique (P_3) to the beam. The figure 5.4 shows each orientation in the reciprocal space, each resulting in different patterns. The first two orientations give the chance to measure d_{002}, L_c and L_a as the (00l) and (hk) bands are well separated.

5.3.3 Dark Field (DF) TEM

In a polycrystal, dark field images can light up only parts of the crystals which are Bragg reflecting at a given orientation. The (110) and (002) orientation can be studied with this technique.

5.3.3.1 (002) DF

When the aperture is rotated along the (002) ring (from a SAD pattern), one rotation position would show a set of BSU (e.g. BSU 1), while it is still rotating, the first set of BSU disappears and another group of BSU appears (BSU 2). This leads to different dark field images as shown in the first two pictures 5.5. If a BSU has a diameter of 1 nm, there is a tolerance of a 10° rotation angle to the beam before it disappears

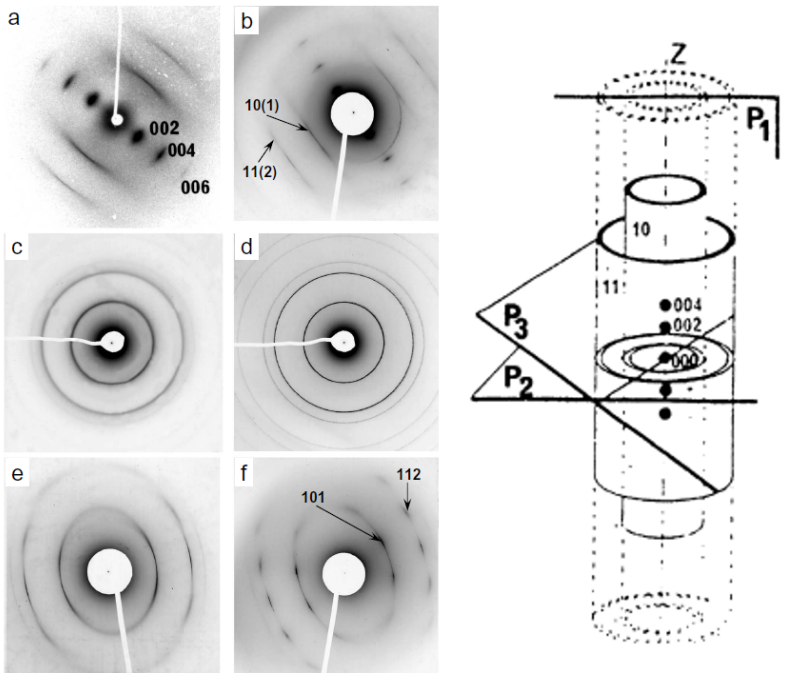

Figure 5.4: Left: SAD images from the different orientation on the right, taken from [128]

in the (002) DF. Knowing the direction of the (002) scattering vector and the image rotation relative to the SAD, the projection of the aromatic layer can be related to the images and the thickness of the BSU can be evaluated. Many TEM images are available in the literature, either for coal, petroleum derivatives or saccharose based carbon, and they all appear to have similar BSU sizes [129, 130, 128].

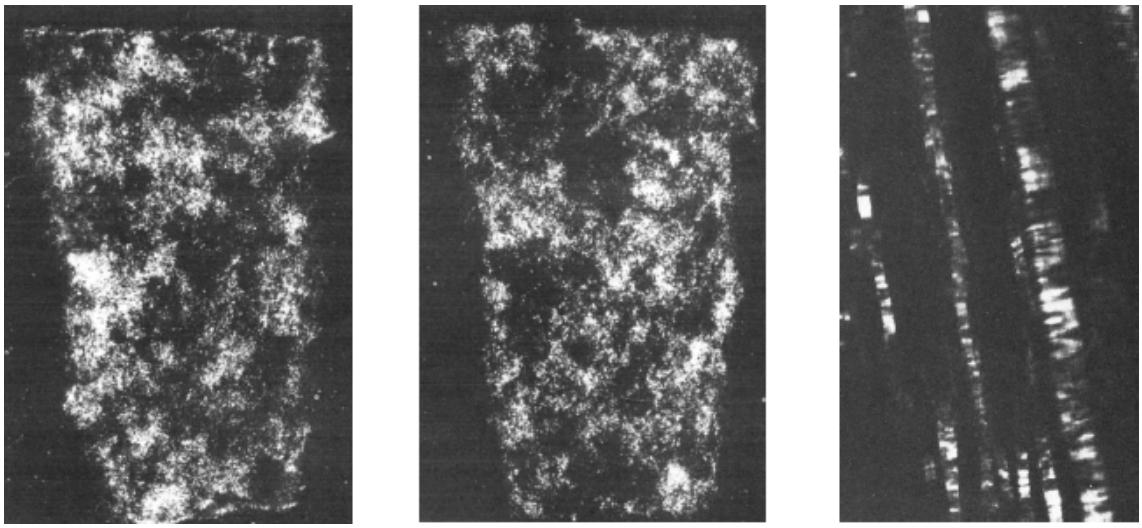

Figure 5.5: The first two images represent BSU 1 and BSU 2 from different rotational angles. The last picture represent a (002) DF image at higher temperature, taken from [131].

Bright dots are formed at low temperature, representing single BSU, but when the

temperature is increased, long and relatively perfect fringes are imaged (see far right picture 5.5).

5.3.3.2 (11) DF

When the layers get a big enough diameter, numerous (*hk*) DF data can be added to the (002) data. Figure 5.6 illustrates (11) DF at two different high temperature stages. Moiré fringes are produced when single aromatic layers are superimposed with slight rotation. Similar Moiré patterns can be observed with (002) bright field, not discussed here. The (*hk*) orientation is a reliable representation of both the orientation and the distortions of the specimen along the planes.

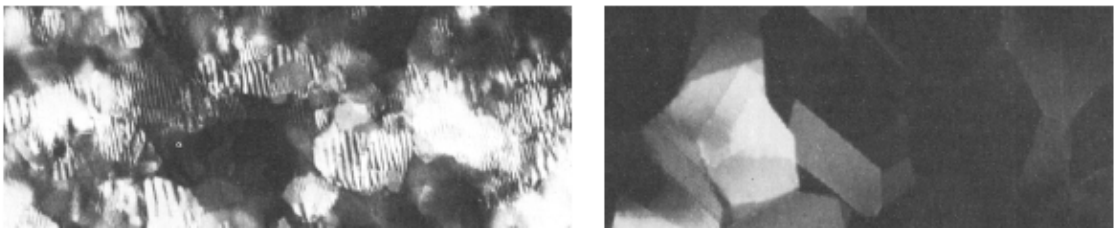

Figure 5.6: (11) DF images of graphitisation carbons at two different high temperatures, taken from [132]

TEM method	What is measured	Description
SAD patterns	L_c(004)	Half width of 004 reflections
	L_a	Half width of 11(0) ring
(002) DF	L_c	Thickness of elementary bright domain (BSU)
	L_a	Length of elementary bright domain
(002) LF	N	Number of fringes in a stack
	$L1$	Length of a perfect fringe
	$L2$	Length of a distorted fringe
(11) DF	L_{tf}	Length of turbostratic Moiré fringes
	L_{cr}	Diameter of a domain showing rotational Moiré fringes

Table 5.1: The different possible measures from TEM

5.3.4 TEM notes

TEM allows the imaging of very small aromatic ring structures present in the low temperature carbonaceous materials. When the small aromatic layers are piled up, an additional (00*l*) scattered beam will appear whereas a single layer alone would only appear in the 10 and 11 asymmetrical bands. If BSUs join together, the area is imaged as a cluster of bright domains and a LMO is defined. Other LMOs, either twisted or tilted, which block the beam, are represented by dark areas. As for the BSUs, in order to get all the LMO, the aperture must be rotated. With an increase of the diameter L_a and the thickness L_c, the (00*l*) nodes and the (*hk*) lines in SAD patterns would become smaller and thinner, this induces a change in the DF images. If the instrument setting can be known with enough accuracy, (002) LF images can be used concurrently with (002) DF. It can be valuable to compare the two images together. Despite the fact that both are based on the Fourier transform of the same (00*l*) scattered beam their uses overlap but they are partly complementary. The table 5.1 summarises the possible measurements available from TEM according to the experiment cited in this chapter.

5.4 Conclusion

Many available techniques were presented in this chapter. It was shown that they all bring valuable information about the evolution of the crystal structure as the temperature increases. They can be used individually but they give a better understanding of the graphitisation when they are put together. Other techniques can be found in the literature but their usage is restricted to few, if not just one, stage of the graphitisation.

Chapter 6

Twist Boundaries in graphite and the effect on d_{002}

One of the later stages of graphitisation is the change from a two dimensional structure (2D) to a three dimentional structure (3D), in other words, from turbostratic to AB graphite. Turbostratic graphite was defined by Biscoe and Warren as layers of graphene stacked upon one another with random relative orientations [10]. Later, it was also acknowledged that experimental work on graphite can also induce a twist in the layers; this can happen when graphite is mixed with an organic solvents [133], or when a metal atom is deposited on the surface [134]. The phenomenon is usually observed near or along grain boundaries, lattice dislocations and defects [135]. When two neighbouring layers are misoriented, Moiré patterns can be observed [136]. The normal periodicity of 246 pm changes, depending on the misorientation angle, to a higher value arising from a superperiodic hexagonal structure. Tubostratic graphite can give rise to an increase of up to 2.7% from the normal AB stacking interlayer spacing value [137]. One of the reasons for this phenomenon has been attributed to the weakening of the binding between layers. Estimates for the interlayer binding energy in graphite vary; 35 meV/atom [138] is typical, however another theoretical work has found 25 meV/atom [139] . In this section, the aim is to review the variation of the interlayer spacing d_{002} with relative orientation angle for turbostratic graphite, including whether AB graphite lies on the same curve, or not.

6.1 Franklin's model

On the basis of x-ray diffraction measurements on different carbons [65], Franklin described the interlayer spacing between two layers to have only two possible values; 334 pm in graphitic carbon and 344 pm in non-graphitic graphitising carbon. Any intermediate values between these two are the result of samples containing both perfect AB and turbostratic regions. Figure 6.1 illustrates the intermediates according to Franklin. The interlayer spacing of graphite with AB stacking is a, while for the normal 'disorientation' (Franklin's terminology) the spacing is b, and the two intermediate spacings are c and d. Thus, c is a reduced distance from disorientated and orientated layers, whereas d is the doubly reduced distance from two orientated layers. The arrows indicate the positions of disorientations.

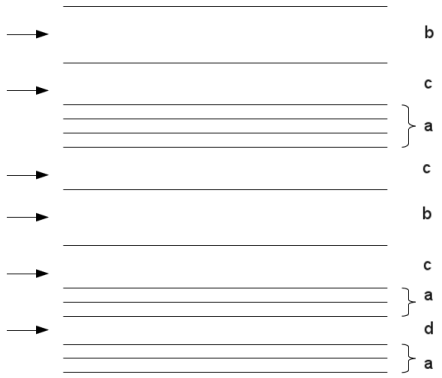

Figure 6.1: Schematic representation of intermediate inter-layer spacings in graphitic carbons described by Franklin [65].

6.1.1 Equations from Franklin's model

Franklin found that a relationship can be written between the measured interlayer spacing d and the probability p that two layers are misorientated. The equation is

$$d_{002}\ (\text{pm}) = 344.0 - k'(1-p) - 2k''p(1-p),$$

where $k' = 8.6$ pm is the reduction in spacing corresponding to the change from a turbostratic structure to an AB graphite, as already introduced in section 4.5.1 of

chapter 4. The quantity k'' is the reduction in spacing of disoriented layers in contact with an orientated group. Franklin found that the best agreement with experiment was given by $k'' = \frac{1}{2}k'$. In this case, it is supposed that the spacing between a disorientated layer and an orientated group lies halfway between the two extreme values, while the spacing at a single disorientation, isolated between two orientated groups, is the same as that within an orientated group. The equation above becomes

$$d_{002}\ (\text{pm}) = 344.0 - 8.6(1 - p^2).$$

This approximation means that Franklin assumed that there are only three inter-layer spacings with an intermediate value of 339 pm. However according to Bacon [140], k'' is different from $\frac{1}{2}k'$, since the the spacing between a disoriented layer and an oriented group is significantly nearer to that of a pure disoriented structure than to that of a pure oriented structure. This lead to a new equation for $p < 0.4$:

$$d_{002}\ (\text{pm}) = 344.0 - 8.6(1 - p) - 6.4p(1 - p). \tag{6.1}$$

Bacon also finds that a better fit to experiment can be found over an increased range of p if an extra term, $0.03p^2(1 - p)$, is appended to 6.1. Thus, Bacon considered four different spacings with two intermediate values of 341 pm and 337 pm, instead of the single value of 339 pm used in Franklin's model.

6.2 Modelling the structures

Model structures of turbostratic structures with different degrees of misorientation are generated by a FORTRAN program [141]. These models contain two graphene sheets that are rotated by equal amounts in opposite directions. The choice of the rotational center, either an α or a β carbon atom, can produce different orientations. The D_{6h} symmetry of the crystal about an axis through α means that neighbouring layers have a range of relative rotation angles θ from 0° to 60°, with respect to each other. When a β site is the centre, the structures have D_{3h} symmetry and are symmetric at 30°, returning to AB stacking at $\theta = 60°$. However, when an α site is the centre, $\theta = 60°$

produces AA stacking.

Specific relative rotation angles give rise to coincident lattice points for the two graphene layers projected on the basal plane. This means some pairs of atoms lie on lines along the prismatic direction. If A and B are described as the graphite lattice vectors, taken in integer multiples of n and m respectively, then V, the superlattice vector of the first layer is given by

$$V = nA + mB.$$

If U is the superlattice vector of the second layer, then in order to find the same superlattice vector length, U must be equal to

$$U = (n + m)A + (-m)B.$$

Figure 6.2 illustrates the superlattice vector V. As an example, if we take $n = 2$ and $m = 2$ in the expression for V, then U must have integers of $n = 4$ and $m = -2$. High integer values of n and small integers value of m for the V superlattice vector produce small relative rotational angles between both layers. The FORTRAN program varies both n and m and calculates every possible angle with the number of atoms required to form a primitive unit cell of two layers. This is illustrated in figure 6.3 when n and m are varied over the range 1–9.

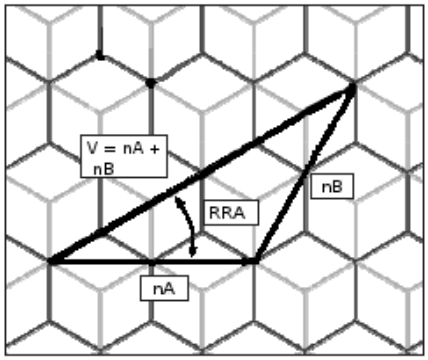

Figure 6.2: Schematic representation of the superlattice vector V.

The red curve in figure 6.3 shows that for relative rotational angles smaller than 8° (and more than 52°), the minimum size of the unit cell grows rapidly. These cells are

too large for DFT calculations to be done for them. The curve also indicates there is a wide range of angles giving cells that contain manageable numbers of atoms. Hence, only some unit cells containing less than 250 atoms are investigated in the following calculations because structures with slightly different relative rotational angle can have unit cells with different numbers of atoms. For instance, a 21.8° structure is obtained with $m = 2$ and $n = 1$ and only 28 atoms, whereas a relatively close structure with an angle of 24.4° is obtained with $m = 7$ and $n = 2$ and 268 atoms.

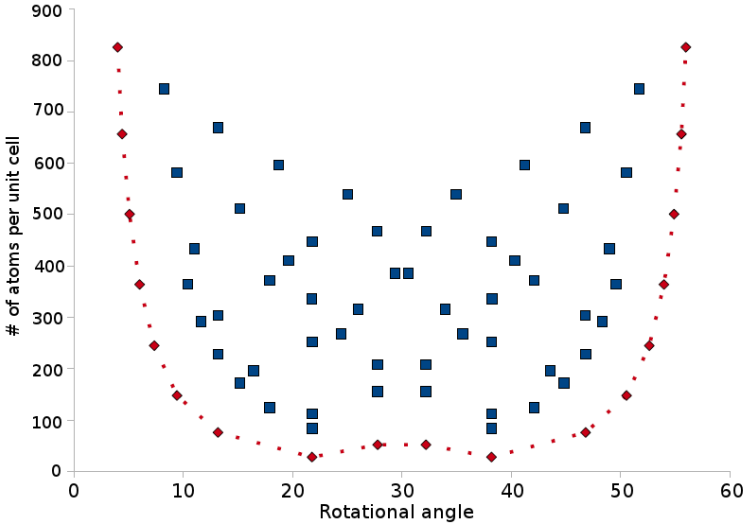

Figure 6.3: Coincidence site lattice point angles

6.3 Energy and interlayer separation optimisation

In this section, the aim is to calculate the interlayer spacing for turbostratic graphites with different rotational angles. The calculations begin with a unit cell containing two layers, and are subsequently extended to four and eight layers.

6.3.1 Computational details and choice of the basis set

In chapter 3 section 3.1.2, the Gaussian basis sets used in AIMPRO were introduced. For graphite, the existing AIMPRO basis set library contains four different, optimised combinations; *pdpp*, *pdddp*, *pppp* and *ddpp*. The first two are considered to be more reliable than the last two, and of these *pdpp* represents a good compromise in terms of size and accuracy. Table 6.1 provides a summary of the structural parameters for

graphite calculated using these basis sets, together with their experimentally observed values. Primitive unit cells of four atoms are used in the following assessment of basis sets. The Brillouin zone is sampled using the Monkhorst and Pack scheme with a $30 \times 30 \times 2$ mesh, and the states are occupied according to the first-order Methfessel-Paxton scheme with $kT = 0.01$ eV.

Basis set	d_{002}	a	Bond Length
pdpp	325	244	141
pdddp	333	244	141
pppp	320	244	142
ddpp	326	244	142
experiment [142]	335.40 ± 0.03	246.12 ± 0.01	142.10

Table 6.1: Structural parameters for an ideal four-atom primitive unit cell of graphite calculated by the AIMPRO method using four different basis sets, and their experimentally observed values. All values are in pm.

It can be seen from these results that the size of d_{002} given by the *pdpp* basis set is 325 pm, which is about 3% smaller than the experimental value 335 pm.

The *pdddp* basis set is chosen for later calculations as it gives an interlayer spacing value of 333 pm for AB stacking, making it within 1% of the observed size. For the following results, Monkhorst-Pack sampling of the Brillouin zone is used, with grids varying from $2 \times 2 \times 2$ to $5 \times 5 \times 2$, depending on the size of the cell. The states are occupied according to the first-order Methfessel-Paxton scheme with $kT = 0.01$ eV.

6.3.2 Two Layers

Seven structures with rotational angles varying from 9.4° to 50.6° have been investigated, with both the atom positions and the lattice parameters optimised. AA stacking is found to have, as expected, the highest d_{002} value of 357 pm, in good agreement with earlier calculations where $d_{002} = 366$ pm [143] given the 1% underestimation using this basis.

For the interlayer separation of the seven rotated structures, the values calculated are shown in table 6.2. A very small change (± 0.002 pm) in the C-C bond length appeared between the AB stacking and the rotated structures. This is due to the break in symmetry in the rotated structures. Figure 6.4 shows how the interlayer separation (blue line) and the interlayer energy (red line) vary with the relative rotational angle.

Angle	m, n	# of atom	d_{002} (pm)
13.2°	7, 1	228	340.7
17.9°	5, 1	124	340.1
21.8°	4, 1	82	340.1
27.8°	3, 1	52	340.1
38.2°	2, 1	28	340.3
46.8°	3, 2	76	340.8
50.6°	4, 3	148	341.6

Table 6.2: Calculated d_{002} with respect to relative rotational angle in a two-layer cell.

The interlayer separation and energy are nearly constant for intermediate relative rotation angles, not including 0° and 60°. There is only a shallow minimum in the curve for the interlayer separation at 30°. The interlayer energy is calculated by comparing the energy of two layers in graphite with two isolated graphene layers. It is found that AB graphite is bound by about 44 meV/atom, which is in fair agreement with earlier work [138]. The difference in binding energy between AB graphite and AA graphite is calculated to be about 11 meV/atom.

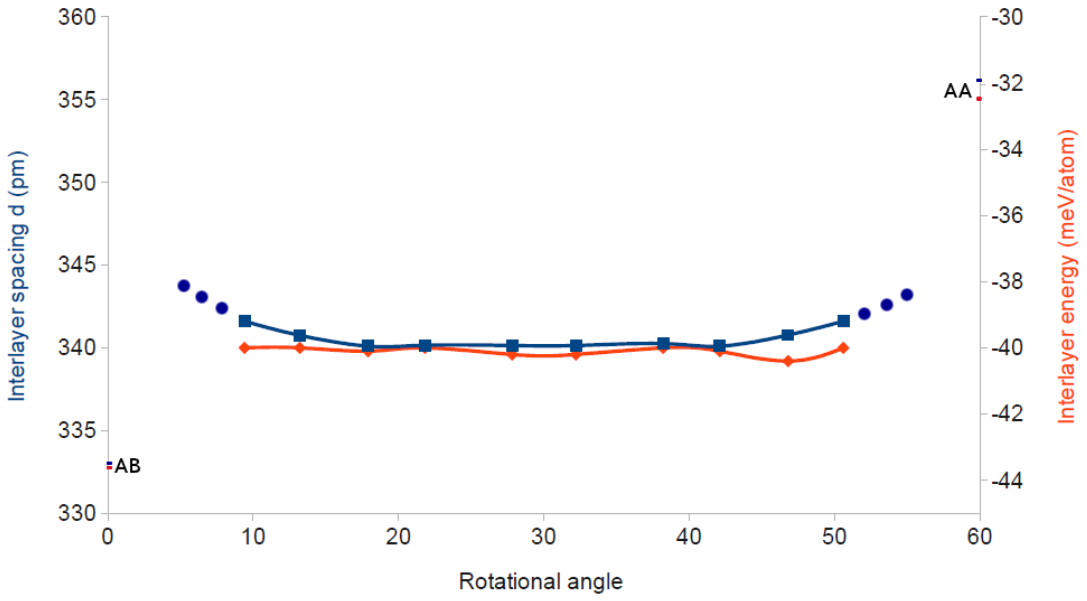

Figure 6.4: Interlayer spacing, d_{002} and interlayer energy of graphitic structures with different rotational angle in a two layer unit cell. A smooth curve is drawn between the points to guide the eye. The dots is an extrapolation of the blue line.

The dotted blue line in figure 6.4 represents an extrapolation of the full blue line excluding the points at 0° and 60°. It appears that there might be a discontinuous change in both d_{002} and in the interlayer energy between a turbostratic structure and both, AB and AA graphite stackings. Similar calculations in earlier work [144] agree

well with the present results.

With a two-layer cell, two of the four interlayer spacings described by Franklin can be calculated. The interlayer spacing a, calculated previously in section 6.3.1 table 6.1, and the pure turbostratic value, b, which is about 340.5 pm if we take the average d_{002} overall the rotated angles calculated (table 6.2). The discrepancy between experiment, 344 pm [66, 140], and our calculations is slightly more than 1%.

6.3.2.1 Remarks on the interlayer spacing

In this section we examine in more detail the reasons for the nearly constant interlayer spacing at all relative rotation angles excluding 0° and 60°. Figure 6.5–a) illustrates the stackings of two layers with a selected angle. It shows that when a layer is rotated with respect to another, there is a mix of three approximate stackings: AA, AB and an intermediate state called SlipBA. Campanera *et al.* wrote a FORTRAN algorithm to calculate the fractions of AA, BA, or SlipBA for angles varying from 0° to 60° [144]. The results of their program is shown in figure 6.5–b).

According to their results, structures with a rotational angle within the range of 0°–15° are characterised as having a higher percentage of AA- and BA-stacked graphite regions than SlipBA-stacked. This situation is reversed in the structures with rotational angle within the range of 15°–30°.

The range used for our calculations, when compared to figure 6.5–b), is in the regime where the system contains mostly the slipBA form. Hence, this could be responsible for the nearly constant interlayer spacing.

6.3.3 Four Layers

In order to estimate the third interlayer spacing d, the same relative rotational angle structures were extended to four layers per cell. We now have four interlayer spacings with only one rotation between two layers. Both the atoms positions and the lattice parameters have been optimised. The calculated value of d_{002} at each of the angles

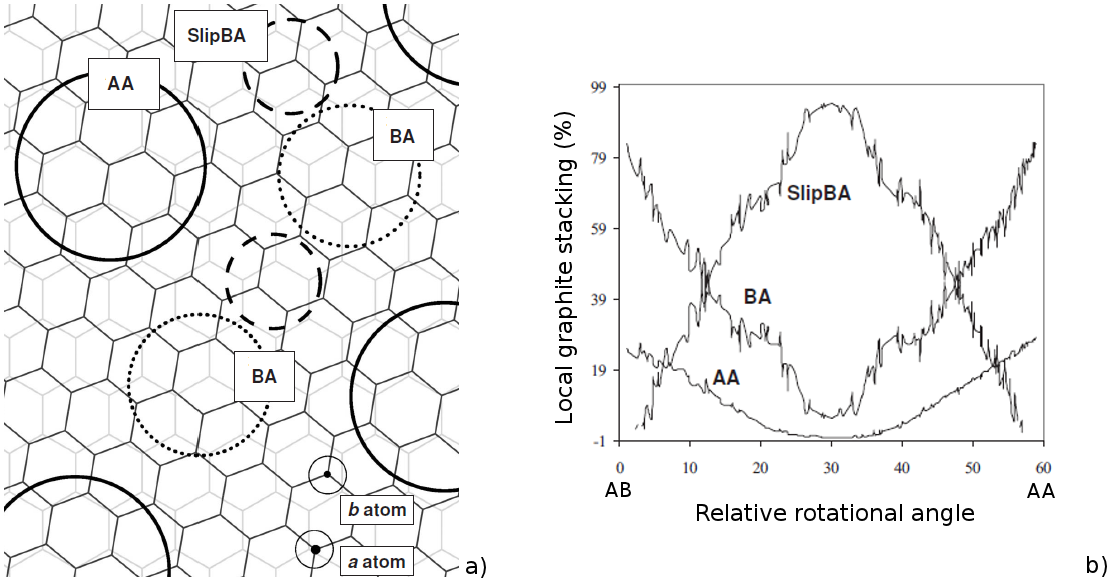

Figure 6.5: a) Illustration of the mix of AB, AA and ABC stacking when two layers are rotated or slipped, b) Fractions of AA, BA, or SlipBA in rotated structures, taken from [144].

in table 6.2 are 336.6, 336.4, 336.5, 336.7, 336.4, 336.4, and 337.0 pm, respectively. Figure 6.4 shows how the interlayer separation (blue line) and the interlayer energy (red line) vary with the relative rotational angle. The interlayer separation now spans a range of 0.6 pm for intermediate relative rotation angles, not including 0° and 60°.

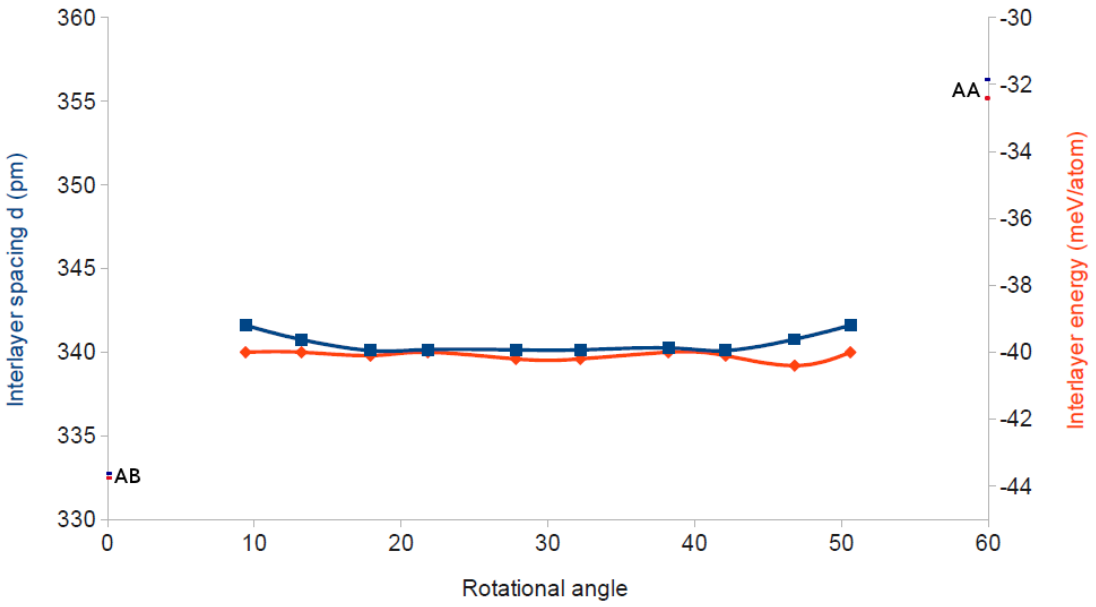

Figure 6.6: Interlayer spacing (blue) and interlayer energy (red) of graphitic structures with different rotational angle of one layer in four-layer unit-cells.

The average value over all the angles (except 0° and 60°) for the third turbostratic distance, d, is about 336.7 pm. The discrepancy between experiment, 341 pm [140], and the present results is slightly less than 1%.

6.3.4 Eight Layers

The interlayer spacing b and d found in the sections above were calculated by taking the average values of all relative rotational angles. However, the number of layers must be extended to eight in order to obtain the final parameter c. Unfortunately, the number of atoms can become very large with some angles, for example a rotational angle of 13.2° has 912 atoms per unit cell. If we take into account that, regardless of the rotational angles, the interlayer spacing is found to differ by 1.6 pm in a two-layer cell and only 0.6 pm in a four-layer cell, as shown in graphs 6.4 and 6.6, respectively, then we can find the c parameters with only few structures. Hence, in order to facilitate the calculations, only the two rotational angles with the lowest number of atoms per cell have been chosen: 21.8° and 27.8°. After optimisation the values found for d_{002} are 333.5 pm and 333.9 pm respectively. The error between experiments, 339 and 337 pm, [66, 140] and our calculations is also slightly less than 1%.

6.4 Experiment versus Theory

This section compares the interlayer spacings calculated with Franklin's and Bacon's equations (see section 6.1.1) with d_{002} calculated by the AIMPRO program package for a wide range of p, the probability to have disorientated layers.

A graph showing interlayer spacing versus the probability p, calculated using both equations described in section 6.1.1, and the AIMPRO method, is shown in figure 6.7.

6.4.1 Introduction of more disordered layers

In order to be able to measure a wide range of different p-values, it is necessary to introduce more than one rotated layer per cell. In the previous calculations

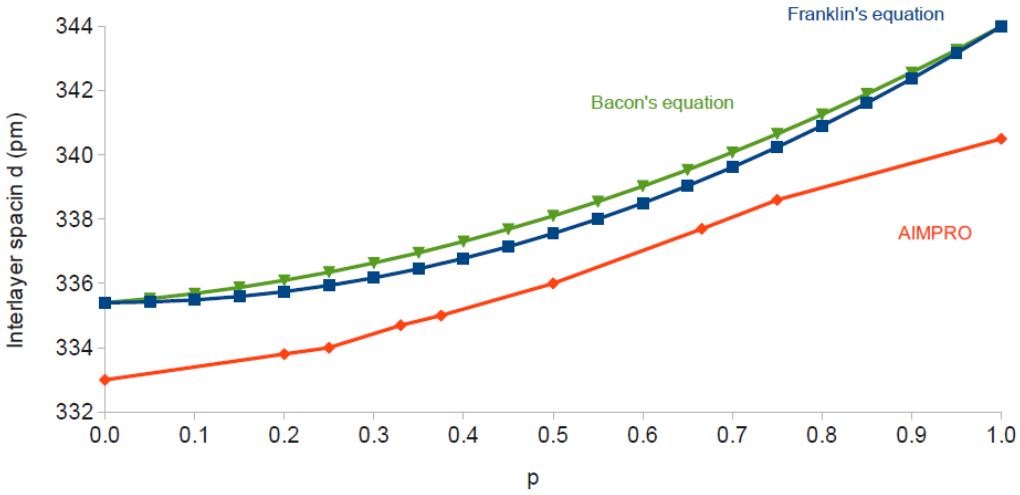

Figure 6.7: Interlayer spacing calculated from Franklin's and Bacon's equations, and by the AIMPRO program package, versus the probability to have disorientated layers, p.

(sections 6.3.2, 6.3.3, and 6.3.4) our structures only determined values for $p = 1, 0.5, 0.25$, respectively. Unfortunately, introducing a second disordered layer by using a second rotational angle is challenging, since the superlattice vectors for both different relative rotational angles must match. For example, the length of the superlattice vector is $a = 892$ pm for a 27.8° angle, while for a 21.8° angle $a = 1120$ pm. In order to match both superlattice vectors, they must be multiplied by four and five respectively to find a similar superlattice vector. In this case the number of atoms becomes too large for DFT calculations. Instead, we have used the following approach. As already explained in section 6.2, the program rotates two layers in opposite directions; thus, it can be considered as two different rotational angles compared with normal AB graphite. Now, the aim is to match the superlattice vector of one rotated angle with the lattice vector used for perfect graphite, i.e. 244 pm. A relative rotational angle of 43.5° has a superlattice vector of 1712 pm, which is 7.01 times the 244 pm used in perfect graphite. This system contains 392 atoms in a four-layer cell.

6.4.2 Calculations

We have applied the 'double-rotation' method for three structures only: one containing four layers, a second with six layers, and a third with eight layers. This allows us to calculate p values equal to 0.75, 0.50, and 0.375, respectively. Other values of p

can be obtained by varying the number of layers with one rotation. Both the atoms' positions and the lattice parameters have been optimised, and the calculated d_{002} for several models are shown in table 6.3.

Structure, # of rotation	p	d_{002}(pm)
2 Layers, AB Stacking	0.000	333.0
10 Layers, 1 rotation	0.200	333.8
8 Layers, 1 rotation	0.250	333.9
6 Layers, 1 rotation	0.333	334.7
8 Layers, 2 rotations	0.375	335.0
4 Layers, 1 rotation	0.500	336.2
6 Layers, 2 rotations	0.500	336.1
3 Layers, 1 rotation	0.666	337.7
4 Layers, 2 rotations	0.750	338.6
2 Layers, 1 rotation	1.000	340.5

Table 6.3: Calculated interlayer spacings for different values of p

The results of these calculations are represented by the red curve in figure 6.7. Compared with Franklin's and Bacon's measurements, the interlayer spacing is slightly underestimated by the AIMPRO calculations, as is typical for the LDA and this basis. However, it can be seen that the form of the curves derived by experiment and theory differ: theory predicts a more nearly linear relationship between d_{002} and p than experiment. Nevertheless, the general trend is similar, and the difference in d_{002} for $p = 0.0$ and $p = 1.0$ is nearly equal. A possible explanation for the difference in curvature between theory and experiment may be related to the difficulty of optimising the large models used by the AIMPRO method. Another possibility is that the form of the variation is indeed incorrect.

6.4.3 Conclusion

After Biscoe introduced the term turbostratic graphite, significant effort was put into numerical relationships to describe the evolution of the interlayer spacing between turbostratic graphite and AB graphite. In this chapter, we have investigated the changes in the interlayer spacing, d_{002} between a 2D structure and a 3D structure. Using a program package, we have been able to construct a wide range of structures with different relative rotational angles, in order to model turbostratic graphite. The two intermediate interlayer spacings between turbostratic graphite and AB graphite, first measured by Franklin and later by Bacon, have been calculated by the AIMPRO

method, and good agreement (± 1%) is found between theory and experiments. We then compared Franklin's and Bacon's equations to different models employing the AIMPRO program package. These results are also found to be in fair agreement with those derived from experimental measurements. Calculations of a similar nature do not appear to have been performed previously. Although, LDA underestimates the interlayer spacing in graphite, DFT has shown to be a good technique to estimate the probability of misorientated layer, p.

Chapter 7

The role of sulphur in graphitisation

In chapter 4 on graphitisation, it was explained that heating precursor materials results in the removal of non-carbonaceous and carbonaceous gases from them. After the first carbonisation, the carbon yield, for most precursors, is above 95 at.%. The remaining fraction is mainly oxygen and other heteroatoms. Two other important impurity atoms are sulphur and nitrogen. Considerable attention was paid to their effects when added to relatively pure carbon compounds, to find evidence for the mechanisms by which microstructures are formed. It was shown that heteroatoms like oxygen, depending on their concentration, can inhibit the aromatic polymerization that promotes mesophase. However, other experiments have studied the addition of heterocyclic compounds, and found that the graphitisability of cokes that originally graphitise poorly is improved [145]. The concentration of 'impurities' (these can be intentional or unintentional) present in coal-tar pitches and petroleum cokes can be high. Sulphur concentration was found to be as high as 13 wt.% [146]. As the temperature increases, heteroatoms (except boron) become increasingly volatile which can have significant effects. Some of them (O and N) are evolved before 1400 °C. However, in certain materials, sulphur continues to evolve for temperatures up to about 2500 °C [147]. This chapter discusses the role of sulphur during graphitisation. It begins with a review of experimental work from the literature, and includes a description of the role that sulphur is believed to play during the process of

graphitisation, along with the properties of elemental sulphur. Our theoretical work is then presented. It aims to verify experimental works and to discover new modes of action for sulphur.

7.1 The history of sulphur in graphitisation

7.1.1 Puffing effect

It might be expected that the removal of impurities from a precursor during the process of graphitisation would result in shrinkage of the material. Nevertheless, some graphitising carbon can often undergo an irreversible expansion during heat treatment between 1400 °C and 1800 °C [64]. This effect is often referred to as 'puffing'. The process is linked to sulphur, and sometimes to nitrogen (e.g. in coal tar-based needle coke), present in the mixture. Experiments have shown that the impurity concentration is not the main factor: the deformation is characterised by the formation of micro pores and cracks, created by the sudden release of hydrogen sulphide, carbon disulphide, and nitrogen gas. This can affect the final properties by reducing the bulk density, strength, and conductivities [148]. Desulphurisation, or the use of low-sulphur feedstocks, are the usual solution to this problem for manufactured graphite nowadays [149]. However, puffing remains a subject of research in order to reduce the number of steps and save time for the process. According to Whittaker, dimensional changes of up to $\Delta l/l \sim 3\%$ in a binder-filler artefact can occur [150]. Cokes respond differently to puffing effects depending on their concentration of volatile impurities (S, N and O): the higher their concentration is, the sooner (lower temperature) that puffing begins.

Table 7.1 shows the evolution of the impurities' concentrations at different temperatures. A review by Fujimoto enumerates the main factors that puffing depends on [151]:

- The extent to which cokes result from the binder or the impregnation pitches.
- The particle size of the filler coke: smaller particles lead to less puffing.
- The coke used: two different cokes with the same concentration of heteroatoms

Heat Treatment temp. (°C)	Coke puffing at 1400 °C (wt.%) S	N_2	O_2	Coke puffing at 1700 °C (wt.%) S	N_2	O_2
Raw Coke	4.90	1.37	0.90	0.80	0.33	0.68
1250	4.72			0.77	0.01	0.05
1400	3.73	< 0.01	0.0	0.74		
1600	0.37			0.75		
1800				0.62		
2000	0.09			0.54		
2400	0.01			0.13		
2600				0.00		

Table 7.1: Volatile impurities in petroleum cokes heated to various temperatures, taken from [150]. The coke with a higher impurity concentration (left column) start puffing at a lower temperature (1400 °C) compared to the coke with a lower impurity concentration (right column) which start puffing at a higher temperature (1700 °C).

can exhibit different puffing.

- Sulphur and nitrogen content: CS_2 can cause puffing more readily than cyanides (CN).

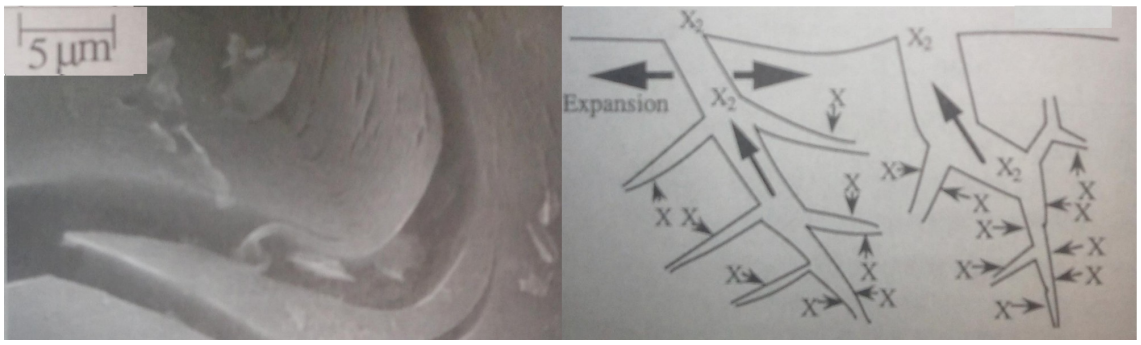

Figure 7.1: Pore creation during the puffing effect, taken from [152]. X represents sulphur or nitrogen. The left picture shows basal cracks and the right picture is a schematic representation of the puffing effect.

Puffing usually occurs during the 'plastic' phase of the graphitisation (i.e. above 1000 °C). Figure 7.1 shows a possible mechanism involving heteroatoms during puffing. The evolving gases (e.g. X_2) push on the pore wall of the coke as they expand and escape from the microfissures. Sulphur (and nitrogen) may travel to its nearest microfissure, and puffing happens when the pressure of the evolving gases exceeds the strength of the pore wall.

Different techniques were found to reduce this effect. Desulphurisation of the cokes during calcination is one that has already been described. Reduction of the rate of temperature increase is another approach. Unfortunately, it does not always provide

a solution since a slow cycle can modify the final graphite properties, and may even degrade it [151]. Additives, called puffing inhibitors, can be used [149, 148, 153]. In petroleum needle coke, puffing is inhibited by adding iron oxide (Fe_2O_3). At 525 °C, approximately 20% of the Fe_2O_3 added could be accounted for by FeS. At 1200 °C, it was calculated that over 95% of the original Fe_2O_3 had been converted to FeS [149]. In coal tar based needle coke, cobalt and nickel oxide reduce puffing [148]. Compounds such as boric acid or disodium hydrogen phosphate (DHP) have also shown signs of puffing reduction [153]. Sometimes catalytic activity for graphitisation may be related to puffing inhibition. Kipling *et al.* studied the effect of sulphur on the pyrolysis of polyvinyl chloride sulphur (PvCS) [154]. They observed an increase in viscosity of the PvCS when the sulphur concentration exceeds about 5 wt.%. This trend continued with increasing concentration of sulphur and was accompanied by changes in the microstructure to glassy carbon at about 9 wt.% S. However, the more viscous the intermediate materials are, the more difficult the reorientation process for obtaining a graphitic carbon becomes. Nevertheless, Kipling concluded that unless the concentration of sulphur is higher than 9 wt.%, no effect is observed on the graphitic structure.

7.1.2 Sulphur as a promoter

Despite the dramatic changes that sulphur may cause during the puffing effect, other experiments have established that it can enhance graphitisation. Christu *et al.* were the first to recognise its 'positive' effect [155]. After heat treatment in the presence of dibenzothiophene, at temperatures above about 1700 °C, they found that a new peak appeared in the x-ray diffraction pattern corresponding to the (002) reflection at 26.7° using CuK_α wavelength, which is consistent with the formation of ordered layers inside the material. To confirm that only sulphur was responsible for the new peak, iron oxide (a puffing inhibitor) was introduced in the initial carbon sample, and the peak disappeared. The same year, another group independent from Christu's group, studied the pressure generated by the puffing effect, and they concluded that pressure enhances the graphitisation process [150]. The sulphur concentration in their materials was around 5 wt.%. The benefits of pressure are also described in chapter 4.

Fitzer and Weisenburger also made x-ray measurements of petroleum and pitch cokes, but with a lower concentration of sulphur (0.4 wt.% to 1.7 wt.%) [156]. They found similar results to Christu, and agreed with the conclusion that there are no possible sources, other than sulphur, for the peak. Fitzer and Weisenburger also observed a contraction of the interlayer distance for temperatures between 1400 ° and 1700 °C in materials containing sulphur, while this contraction usually happens at around 2200 °C in materials free of sulphur. Finally, they found that the activation energy of graphitisation is decreased from 7–10 eV to about 3–4 eV between 1400 ° and 2000 °C in the presence of sulphur. Brandtzaeg and Oye [157] described the promoting steps in a similar way to Whittaker and Grindstaff [150], as being the vapour pressure initiated by sulphur. When pressure exceeds a threshold level, puffing can start, and sulphur is released. The sulphur subsequently reacts with imperfectly located carbon atoms to form CS_2 and CS gas. These leave perfect oriented carbon atoms behind. Bourrat *et al.* [158] found the source of sulphur that is responsible for promoting graphitisation arises from thiophenic sulphur, which does not inhibit the formation of mesophase spheres.

7.1.3 Sulphur classification within graphite

In order to rationalise the many different descriptions for the role of sulphur during graphitisation, Bourrat *et al.* classified them in three types. Type I sulphur is defined as sulphur in a gaseous state, H_2S primarily, that is released during the first carbonisation, and has completely disappeared at the end this stage. The amount of sulphur evaporated as a gas is considered to be half of the initial sulphur concentration. Type II sulphur is described as a modifier, and is present at temperatures between 1300 ° and 1700 °C. They acknowledged this type to be responsible for the puffing effect. It is fully eliminated at about 1700 °C. The final type (III), still present above these temperatures, can only be removed with further heating. Figure 7.2 illustrates how the three different classes of sulphur change as a function of temperature. No experimental works appear to have confirmed this, but according to Bourrat *et al.* it is believed that type III forms cross-links between layers or polyaromatics. However, Kipling *et al.* [154] suggested that these cross-links would appear only when there is

a high concentration of sulphur.

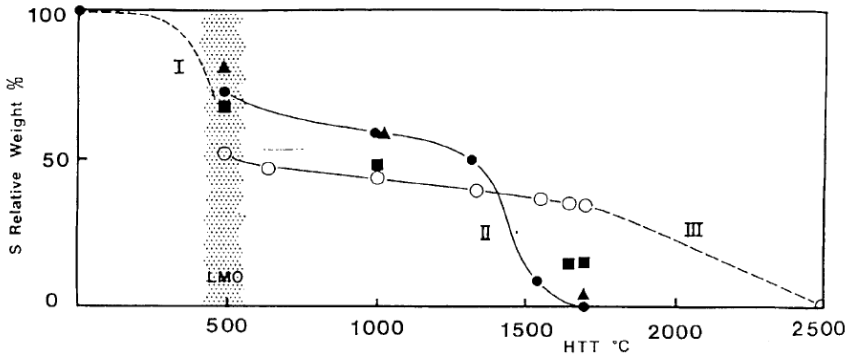

Figure 7.2: The three types of sulphur (I, II and III) versus temperature, taken from [158]. The shaded region at about 500 °C, represents the formation of the distorted piles of molecules in complete disorder (LMO). Weight % is relative to precursor sulphur concentration.

7.2 Review of some of the graphite lattice and sulphur crystal properties

7.2.1 S_8 molecule and orthorhombic α-sulphur

Elemental sulphur comprises different shaped rings of atoms. The best known, and most stable, is the S_8 ring. This is the basic unit of the most stable types of sulphur crystals. It can be described geometrically as a crown-shaped molecular unit, with a point symmmetry group of D_{4d}. The α, β, and γ allotropes of sulphur represent different spatial arrangements of these S_8 units. There are similarities in their structures, but they differ in their bond lengths, bond angles, and torsion angles [159]. The orthorhombic structure, or α allotrope, is based on monoclinic sulphur, β. The α form isomerises into the β form above 95.31 °C [160]. It has a space group of *Fddd* [161].

7.2.2 Point-defects in graphite

One of the features that both graphitisation and radiation damage have in common, is the presence of lattice defects. In radiation damage, fast neutrons collide with carbon

atoms from the graphite lattice, and these atoms may be displayed. Thus, interstitial atoms and vacancies are formed, as already explained in chapter 1.

In this section, only vacancy defects are reviewed. If a carbon atom is removed from one of the planes in graphite, and on either an α or a β site, there is a D_{3h} symmetry with a threefold axis through its centre. This is illustratated in figure 7.3B. This monovacancy defect reconstructs to a more stable structure as described in [39] and the symmetry is changed to C_{2v}.

It is believed that monovacancy on a same sheet can coalesce if they are at a fourth neighbour separation. This is because vacancies become mobile at 200 °C [39]. This allows to reduce the number of broken bonds [162]. If two carbon atoms are removed from one of the planes in graphite, with one on an α site and another on one of its nearest β site, a structure similar to figure 7.3D is obtained. This can reconstruct to a more stable structure described in [39], with an octagon and two pentagons. Many more reconstructed structures are described in this paper depending if the vacancies are second, third or fourth neighbour, and it is also calculated that the nearest-neighbour $\alpha\beta$ divacancy structure is more stable than two isolated monovacancies.

If two carbon atoms are removed, from two neighbouring graphite planes, and both from α sites, a structure similar to figure 7.3C is obtained. Other interplanar models can be formed if β sites are involved. These interplanar divacancy defects can form bound pairs. Two reconstructed structures were first found by Telling *et al.* [163] and another two by Latham *et al.* [39]. In Latham *et al.*'s paper, the four reconstructed structures are reviewed and it is concluded that the stability of multivacancy complexes is controlled by the number of dangling bonds, and their ability to reconstruct.

A few authors have described the possibility of cross-linking between sulphur and graphite [157, 158, 130]. According to Oberlin, cross-linking atoms can bind to BSUs during the self-association stage, which leads to LMOs shorter in size and with lower flexibility [164]. However, this appears to be an early stage phenomenon and this work concerns late stage.

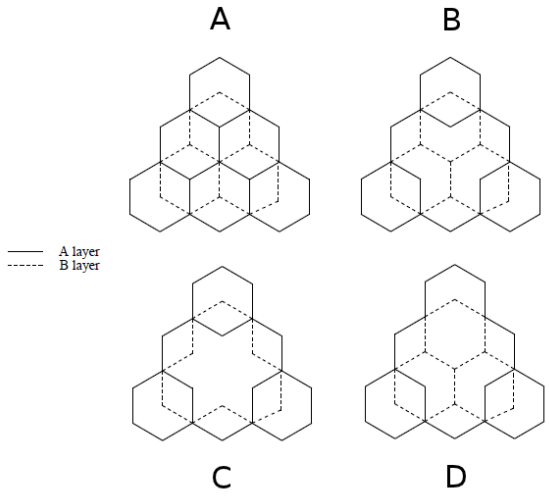

Figure 7.3: Schematic diagram illustrating the construction used for models of cross-linked structures containing sulphur atoms in hexagonal graphite.

7.2.3 Graphite edges and their stability

Graphite is often theoretically represented as a single crystal, meaning there is an infinite number of layers of infinite extent, with AB stacking. However, manufactured graphite is a polycrystalline material. Many individual crystallites with various orientation are joined together to form a solid block at the end of the graphitisation process. Between each crystallite a reconstruction of the bonds occurs in order to minimise the number of broken bonds. This region is called a grain boundary. Impurity atoms also tend to segregate to grain boundaries, where there are opportunities for them to form chemical bonds. During graphitisation, impurity atoms lodged within the grain boundaries may escape. Depending on the local arrangement of atoms, the broken bonds can often further reconstruct to form new bonds with nearby carbon atoms; however, this not always possible.

A single sheet of graphene has two principal low index directions along which it may be cut: armchair and zigzag (also called Fujita edge [165]). A mixed-character edge is produced when a sheet is cut in an intermediate direction. Atoms along an edge can be arranged in various ways. In addition to the low index cuts, other rearrangements including the Klein edge, and the reconstructed zigzag edge [166]. These are illustrated in figure 7.4.

The edges of graphene have been studied widely [167, 168, 166]. Theoretical work

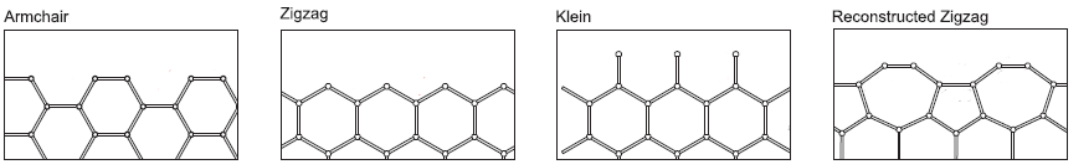

Figure 7.4: Schematic representation of four types of edges found in a graphene sheet, taken from [166].

has shown that edges with a zigzag shape give an extra nonbonding π electron state to the layers [167]. This means that a zigzag edge is higher in energy and less stable than an armchair edge. Radovic *et al.* described the free armchair sites as being similar to o-benzyne (one triple bond on the armchair) while the free zigzag site is carbene-like (one carbon having two unpaired electrons) [168]. These two types of edges can spontaneously recontruct, forming new edge patterns as described by theoretical work [169]. Zobelli *et al.* calculated the formation energy of four types of edges described in figure 7.4 [166]. The armchair and reconstructed zigzag edges have a similar formation energy of 1.10 eV/Å whereas, the zigzag edge is 1.34 eV/Å, and the Klein edge is 2.22 eV/Å.

7.2.4 Folded reconstructions of graphene edges

Folds in graphene have been studied in recent years due to possible new functionalities [170]. The stress induced by a fold can be reduced by the interaction between adjacent layers [138]. Folds have also been produced and observed by scanning tunneling microscopy (STM) in graphitic sheets within HOPG, and can be formed from either one or two layer edges [171]. Indeed, folds inside a graphite crystal (shown in figure 7.5) were observed by TEM more than thirty years ago [132]. During the graphitisation process, the edges of two neighbouring layers can reconstruct in the form of a fold. They are also relatively stable at high temperature and it can be difficult to measure them with x-ray diffraction, since the interlayer spacing c is only slightly modified [72].

Other rearrangements for reconstructed edges have been proposed; three examples are illustrated in figure 7.6. Image A illustrates an edge terminated by a nanotube. Different configurations for the recombination depending on the type of edge and

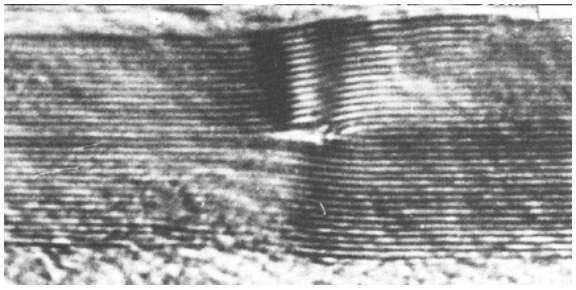

Figure 7.5: A TEM dark field image observed in a (002) lattice fringe of a two-layer fold in graphite, taken from [132].

the type of nanotube have been investigated by Ivanovskaya *et al.* [172]. Image B illustrates the reconstruction of three layers into two folds, where the middle layer has sp^3 carbon atoms along its edge which bind all three layers together. Image C illustrates alternating open and closed edges of graphite distributed over three layers. Other structures are possible; however, they will not be investigated further in the present work.

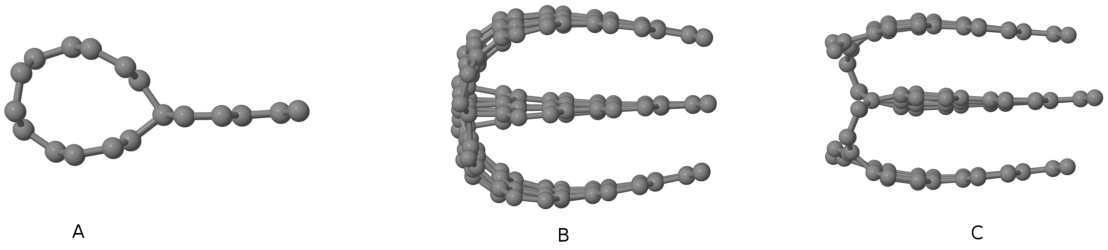

Figure 7.6: Three examples of possible reconstructed edges from graphite layers terminated with a zigzag edge, calculated with DFT: (A) A single layer terminated with a nanotube; (B) A three-layer fold; (C) Alternating open and closed edges.

7.2.5 Prismatic edge dislocation

Prismatic edge dislocations are dislocations for which the line lies in the (0001) plane. Dislocations of this type are formed during the graphitisation process, and can be observed in the crystal [173]. Dawson and Follet are believed to have recorded the earliest image showing an edge dislocation using electron microscopy in synthetic graphite [174]. A schematic representation, in two different configurations is illustrated in the first two images of figure 7.7. The character of the prismatic edge (zigzag or armchair), affects the way in which these dislocations reconstruct. If a prismatic dislocation is terminated by an armchair edge, then there is a reconstruction of the

dangling bond within the layer to form triple bond with *sp*-type carbon atoms. If the prismatic dislocation is terminated by a zigzag edge, then the dangling bonds would interact with one of the neighbouring layers to form new interlayer bonds with sp^3-hybridised carbon atoms. This is illustrated in the last image of figure 7.7.

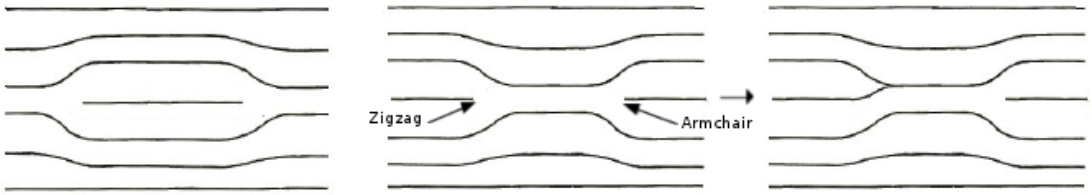

Figure 7.7: Schematic representation of prismatic edge dislocation.

7.2.6 The release of hydrogen sulphide during graphitisation

It is well established that the release of hydrogen sulphide gas occurs mainly during the first carbonisation, and that all of the hydrogen is removed at the end of this stage [158]. Fitzer *et al.* described that an increase in the coke yield in graphitisable carbons can be achieved so long as the H_2S formation is not complete below or at 230° [175]. Another group has shown that sulphur acts as a polymerisation agent for aromatic hydrocarbons [176]. The reactions involved form oligomers containing sulphur, and the polymerisation is effected through the dehydrogenative action of sulphur [176]. The different sulphur compounds, in petroleum sources, have been classified (e.g., sulfur, sulfides (di- and poly-), thiophenes, sulfoxides, etc.) [146]. It is widely believed that the decomposition of organic sulphides account for a large proportion of H_2S gas release at moderate temperature but a non negligible amount of those compounds are still stable at 550° [177].

7.2.7 Remarks

In summary, it is commonly believed that sulphur has a bad influence on the formation of carbon layers, and is responsible for structural defects. However, many authors have described its promoting role at specific stages of the graphitisation process. X-ray diffraction has consistently showed that particular types of materials can have a more

ordered structure at temperatures where it is usually disordered in the absence of sulphur.

7.3 Calculations

7.3.1 S_8 molecule and orthorhombic α-sulphur

Initially, DFT calculations were made on elemental sulphur for validation and as a reference state. The α form is considered in two different ways: (1) as an isolated molecule of eight atoms, and (2) as a crystal. The primitive unit cell of the crystal contains 32 atoms; however, it is more convenient to construct a conventional supercell of 128 atoms, so this was used for the calculations instead. The Brillouin zone was sampled using the Monkhorst and Pack scheme with a sampling of $5 \times 5 \times 3$. The basis set dddd is used for sulphur atoms, and the states are occupied according to the first-order Methfessel-Paxton scheme with $kT = 0.01$ eV. Optimisation of the lattice parameters yielded $a = 9.892$ Å, $b = 12.177$ Å, and $c = 23.471$ Å for their values. These differ from the experimental values by $\sim -5\%$, $\sim -5\%$, and $\sim -4\%$ for a, b, and c, respectively [161]. The observed S-S bond lengths within the S_8 rings are 2.057(4) Å, with an error of less than 0.1% [161]. The difference between theory and experiment is probably accounted for the poor reproduction of weak intermolecular forces, within LDA. Basis set optimisation was only performed for an isolated S_8 molecule, since this procedure is prohibitively time consuming for the crystal unit cell. The new basis set was labelled *pdpp* and contributed to the AIMPRO collection. This yielded both slightly better estimates for the structural parameters of isolated S_8, and lowered the computational cost. The new basis, however, made very little difference to the lattice parameters for the crystal, giving $a = 9.891$ Å, $b = 12.175$ Å and $c = 23.469$ Å. Nevertheless, the calculated S-S bond length of 2.055(2) Å within the S_8 rings is in excellent agreement with the measured interatomic distance. In addition, the calculated bond angle between the sulphur atoms is S-S-S= 108.6°, and the torsion angle is S-S-S-S= 97.3° compared with experimental 108.2° and 98.5° respectively [161].

7.3.2 Notes on the standard heat of formation

The standard heat of formation, or enthalpy of formation, ΔH°, is used to examine the possible sites for sulphur inside a graphite crystal. ΔH° represents the change of enthalpy during a reaction with all substances in their standard states. The example of CS_2 is shown here since its thermodynamics are well documented. The reactants in their standard states, for the formation of a CS_2 molecule, are solid carbon (graphite) and solid sulphur (see paragraph 7.2.1). The reaction is as follows:

$$C(s) + \frac{1}{4}S_8(s) \longrightarrow CS_2(g).$$

ΔH° is calculated by subtracting the sum of the standard enthalpies of formation of the reactants from the sum of the standard enthalpies of formation of the products:

$$\Delta H^\circ = \Delta H_f^\circ(products) - \Delta H_f^\circ(reactants).$$

For the formation of CS_2, the equation becomes,

$$\Delta H^\circ = [\Delta H_f^\circ(CS_2(g))] - [\Delta H_f^\circ(C(s)) + \frac{1}{2}\Delta H_f^\circ(S_8(s))].$$

From AIMPRO, the following energies were obtained:

$$\begin{aligned} \Delta H^\circ &= -26.13755 - (-5.71141 - 20.4727); \\ &= 0.04656 \ Hartrees; \\ &= 1.2666 \ eV. \end{aligned}$$

The measured value from experiment is 116.7 ± 1.0 kJ mol^{-1} [178], i.e. 1.209 eV. The calculated value differs from the measured value by only about 5%. The sign of ΔH° is positive, which means the reaction is endothermic. In order to determine the possible chemical sites for sulphur, the same technique is used on various graphite structures and their ΔH° are compared. It is important to remember that theoretical calculations are at 0 K whereas experimental values are usually at 300 K, hence the difference between the two values. The heat capacity of each molecule at constant

pressure C_p has to be known in order to know the exact difference.

7.3.3 Cross linking and point-defects

In order to investigate the hypothesis that sulphur can act as a cross-linking atom, the following model structures have been constructed in supercells, and optimised using the AIMPRO method. To begin, a single atom of sulphur was placed at several trial locations within the graphite lattice. Next, point defects were introduced by removing one or two selected carbon atoms from the models and the schematic form of these initial models is illustrated in section 7.2.2 figure 7.3. In the following calculations, the Brillouin zone was sampled using the Monkhorst and Pack scheme with a sampling of $7 \times 7 \times 2$. The basis sets *pdpp* and *dddd* are used for carbon and sulphur atoms respectively and the states are occupied according to the first-order Methfessel-Paxton scheme with $kT = 0.01$ eV.

7.3.3.1 Interstitial sulphur

The unit cell of the perfect crystal employed here is orthorhombic and has two layers with 24 carbon atoms in each. The sulphur concentration, in all the structures studied, is about 2 at.%. When a single interstitial atom is placed at various trial positions between the two planes in a perfect crystal, and then optimised, the lowest energy structure resembles the grafted interstitial found in irradiated graphite [179]. This structure is illustrated in figure 7.8A. The sulphur atom lies opposite the centre of a C-C bond, similar to the carbon ad-atom described in [180]. The sulphur atom is bonded to the layer, forming a triangular arrangement. The two carbon atoms nearest to the sulphur atom are pushed slightly out of the original basal plane. The lengths for the two C-S bonds are 1.54 and 1.64 Å, and the C-S-C bond angle is 55°. The standard heat of formation, ΔH°, when the lattice parameters are kept constant, and using

$$48\mathrm{C}(s) + \frac{1}{8}\mathrm{S}_8(s) \longrightarrow 48\mathrm{C} : \mathrm{S}, \tag{7.1}$$

Number of layers (freedom)	Formation energy (eV)	c-axis expansion (%)
2 (fixed)	5.1	0
2 (free)	2.9	25
4 (free)	3.1	10
6 (free)	3.6	3.7

Table 7.2: Calculated formation energies and c-axis expansions depending on the number of layers, and whether the c-axis is kept fixed or optimised, for an interstitial sulphur atom in graphite.

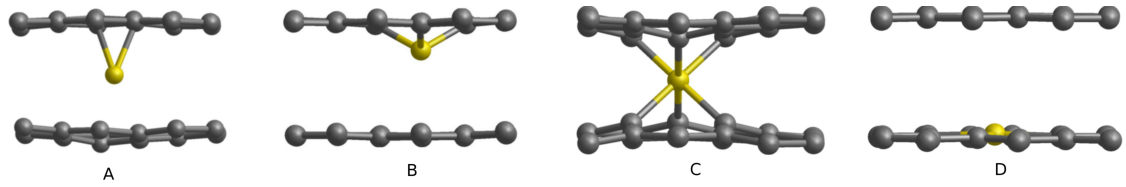

Figure 7.8: Optimised structures for sulphur complexes in graphite and their point group symmetry. (A) Grafted interstitial sulphur atom, C_s; (B) Off-site substitutional sulphur atom, C_{3v}; (C) Interplanar split-vacancy sulphur complex, D_{3d}; (D) Coplanar split-vacancy sulphur complex, C_{2v} (also shown in figure 7.9).

is 5.1 eV. If the lattice vectors are optimised, then the interlayer vector c increases to accommodate the interstitial atom better. This yields a range of d_{002} values depending on the number of layers per unit cell. In a two-layer unit cell, the c value expands by about 25% compared with the original interlayer spacing and give 2.95 eV for ΔH°. Four- and six-layer unit cells are found to expand by about 10% and 3.7%, respectively, and have $\Delta H^\circ \approx 3.1$ eV and ≈ 3.6 eV. The table 7.2 summarises the calculated values.

Some of the calculated expansions appears to be incorrect, and it probably arises from the failures in lattice optimisation method used with AIMPRO. The percentage expansion for the two layers, with the c-axis optimised, is likely to be the closest to reality as sulphur is a large atom. Also, if the 25% expansion is right, then four- and six-layer unit cells should give expansion of about 12.5% and 8.3%

The energies calculated are relatively high for the structure to be formed. The table 7.2 summarises these values. The sulphur atom in this system neither hinders the LMO size nor its flexibility, as no cross-linking atoms are formed. All n trial locations attempted within the graphite lattice gave similar optimised structures and ΔH°.

7.3.3.2 Substitutional sulphur

The next model involves a direct substitution of a carbon atom with a sulphur atom. After optimisation, the sulphur atom stays 'on-site' in the basal plane, and the graphite layer remains flat. The sp^2 bonding is retained, and the sulphur atom is now coordinated to three carbon atoms. All three C-S bonds have the same length (1.61 Å). The structure was found to have a high formation energy $\Delta H^\circ \approx 5.4$ eV, presumably due to weakened σ and π bonding, and compression of the larger sulphur atom. Another structure, where the sulphur atom is placed in a position slightly out of plane, similar to an interstitial (shown in 7.8 B), is found to have lower energy. The difference in energy between the on-site and the off-site structures is about 1.7 eV. The sulphur atom remains coordinated to three carbon atoms, but its bond lengths are slightly longer than when it lies on site (1.69 Å), implying that the compression is smaller. The average interlayer spacing is slightly changed when the unit cell has two layers (~ 3%) or four layers (~ 2.5%). The ΔH° in this case is 3.74 eV using the reaction 7.2,

$$48\mathrm{C}(s) + \frac{1}{8}\mathrm{S}_8(s) \longrightarrow 47\mathrm{C} : \mathrm{S} + 1C(s). \tag{7.2}$$

Strictly, the ΔH° stated previously is for a substitutional sulphur atom on an α site. However, the β site is calculated to have the same heat of formation and same bond lengths to the three nearest neighbouring carbon atoms, to the accuracy of the method. The sulphur atom does not cross-link with the other layers. Interstitial and substitutional sulphur atoms have been investigated, and both of them do not form cross-links. Their energies are also relatively high.

7.3.3.3 Split vacancy complexes

The two other defects studied may be described as sulphur-split-vacancy complexes. Two carbon atoms are missing, which may be taken from either the same plane (coplanar) or from two neighbouring planes (interplanar). The interplanar split-vacancy complex refers to two α atoms missing here (see figure 7.3C). This structure is a trigonal antiprism. For the coplanar split-vacancy complex, a structure

similar to reconstructed lattice vacancy [181] in graphite might have been expected to be the lowest energy state, where two of the carbon atoms form a C-C bond of 1.85 Å on one side of a pentagonal ring, with an eight-sided structure, as illustrated in figure 7.9. Nevertheless, the most stable structure, with 3.1 eV lower energy than the one previously described, is when the sulphur atom is located in the middle of the small void. The sulphur atom possesses four nearly equal bonds, 1.83 ± 0.02 Å long, with the neighbouring carbon atoms. It appears to be similar to the rearrangement found for metals in graphene, where the metal atom is a planar, D_{2h} symmetry centre [182]. Sulphur in diamond adopts a similar split-vacancy structure as a way of accommodating the size of the sulphur atom [183]. As expected, the in-plane sulphur-split-vacancy complex did not cross-link with the neighbouring planes, and the calculated ΔH° for this reaction was found to be 4.5 eV.

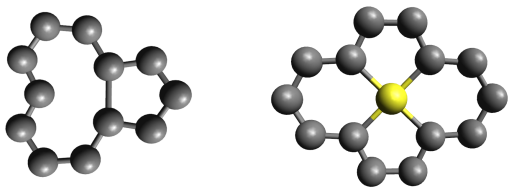

Figure 7.9: Optimised structures of the monovacancy in graphite when formed with carbon atoms (left) and with a neighbouring sulphur atom (right)(a split-vacancy structure).

The last structure investigated, to determine whether a single sulphur atom can cross-link two layers, involves the interplanar split-vacancy complex. The model is constructed so that it can form a cross-link between a pair of neighbouring sheets, each containing an α vacancy. After optimisation, the structure found to have the lowest energy is one with the sulphur atom midway between the two planes. The three nearest carbon atoms on each plane are bound to the sulphur atom to form six S-C bonds. The six bonds have the same length (1.90 Å). The structure is very similar to a single SF_6 molecule, but O_h-symmetry is not compatible with graphite symmetry, and it has D_{3h}. A cross-link is formed, which is illustrated in figure 7.8C. There is a small contraction of the *c*-axis parameter by about 3%. ΔH° for the interplanar split-vacancy complex is 9.7 eV. If the sulphur atom is moved slightly away from its initial position before optimisation, the cross-link is not formed after optimisation, and the sulphur atoms moves toward the nearest plane. The optimised structure gives

one layer with the substituted off-site configuration, and the other plane contains a reconstructed lattice vacancy. This structure is found to have an energy about 0.6 eV less stable than the D_{3h}-symmetry configuration.

7.3.3.4 Remarks on cross-link via sulphur

These results demonstrate that vacancies are necessary in two neighbouring layers in order for cross-links to be formed between them. The one model where sulphur links two layers is found to have a high formation energy: unlikely to appear near thermal equilibrium, but possibly during radiation damage. The idea that sulphur is present in the form of defect complexes cross-linking layers in carbon in the late stages of graphitisation appear unfounded.

7.3.3.5 Cross-linking via S_2 species

Interstitial S_2 molecules within the interlayer spaces, were also investigated in order examine their possible role in the formation of sulphur bridges, similar to what is known to occur in the vulcanisation process of rubber [184]. These simulations followed a similar approach to that used for single sulphur atoms. Optimisation of different trial structures, both with and without vacancies, yielded no results where cross-links form between layers. The lowest energy structure contains a S_2 molecule bridging two β atoms on only one layer. The structure is similar to the β-β arch bridge formed with two interstitial carbon atoms [181]. When one atom of carbon is removed, the molecule rearranges itself around the vacancy but does not make a cross-link. When two carbon atoms are removed, the two sulphur atoms repel each other, and form a pair of off-site substitutional sulphur complexes, one on each plane, similar to the defect described previously. These configurations, similar to others, have high ΔH° values, with the lowest being around 6.5 eV. The results for S_2-complexes reinforce the first conclusion that sulphur atoms do not cross-link graphite planes together when intercalated.

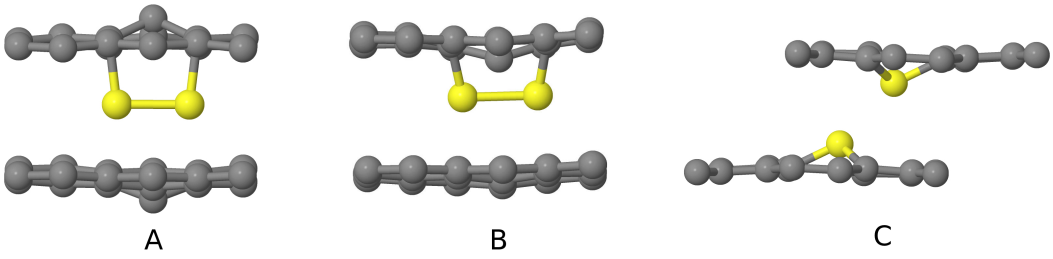

Figure 7.10: Optimised structures for S_2 complexes in graphite: (A) with no defect; (B) with a monovacancy ; (C) With an interplanar divacancy.

7.3.4 Sulphur on the graphite edges

In order to investigate the hypothesis that sulphur can stabilise zigzag and armchair graphite edges, the following ribbons structures have been constructed, and optimised using the AIMPRO method. An orthorhombic cell with two layers, containing sixteen atoms of carbon each, is only repeated in one direction of the basal plane, with one side of the ribbon terminated with four hydrogen atoms. The hydrogen atoms are held fixed to emulate the boundary condition imposed by the rest of the crystal. Both types of edge can be created, although the zigzag edge is the main focus due to its higher reactivity. Each unit cell is represented by at least four graphene edges. Using a similar approach to that of section 7.3.3, the standard heat of formation is calculated. Since the size of the unit cell is variable, and hence the number of edges and the number of sulphur atoms involved are also variable, all the following ΔH° are expressed in electron volts per carbon edge (eV/C_{edge}). In the following calculations, the Brillouin zone was sampled using the Monkhorst and Pack scheme with a sampling of $7 \times 7 \times 2$. The basis sets *pdpp*, *dddd* and *ppp* are used for carbon, sulphur and hydrogen atoms respectively and the states are occupied according to the first-order Methfessel-Paxton scheme with kT = 0.01 eV. Our calculations found a difference of 0.30 eV/Å between the formation energy of a zigzag edge and an armchair edge which is in aggreement with Zobelli *et al.* results [166].

7.3.4.1 Substitution

As Bourrat *et al.* recognised that promoting sulphur (type II) comes from thiophenic-like molecules [158], our first model is a direct substitution of a carbon

atom with a sulphur atom, placed on either a zigzag or an armchair edge. In these cases, it resembles a thiine ring. The equation for this reaction is,

$$32\mathrm{C}(s) + \frac{1}{8}\mathrm{S}_8(s) \longrightarrow 31\mathrm{C} : \mathrm{S} + \mathrm{C}(s).$$

The standard heat of formation for a sulphur atom on a zigzag edge is -0.76 eV/C_{edge}. ΔH° is now negative, meaning that the reaction becomes exothermic. This result gives a first indication that sulphur might be likely to be stable on the edge rather than between or within planes. ΔH°, for a sulphur atom on an armchair edge is also negative; however, the energy is slightly higher, -0.39 eV/C_{edge}.

These two particular structures, with a single substitutional sulphur atom, only correspond to a partially saturated edge, leaving many dangling bonds on other carbon atoms of the other edges. Thus, the final structures are not as stable as they might be. In order to get a better undesrtanding of the effect of sulphur, another model has all edges saturated with sulphur atoms. The previous equation becomes,

$$32\mathrm{C}(s) + \frac{4}{8}\mathrm{S}_8(s) \longrightarrow 28\mathrm{C} : 4\mathrm{S} + 4\mathrm{C}(s).$$

This yields the result $\Delta H^\circ = -1.33$ eV/C_{edge}, which is lower than for a single substitutional atom, and it reinforces the initial conclusion that sulphur atoms are more likely to be found on the edges, favouring the zigzag shape. A unit cell, with substitutional sulphur atoms on a zigzag edge, is illustrated in figure 7.11A.

7.3.4.2 Addition

The shape of the zigzag edge offers many other sites for sulphur atoms. In general, sites at edges provide more opportunities for impurity atoms to bind without generating stress in the structure. In order to investigate the available sites for additional sulphur atoms, several model ribbon structures have been constructed, shown in figure 7.11, where sulphur atoms are attached as ad-atoms to the zigzag edge. The edges of interest are saturated with sulphur so no dangling bonds remain. Structures B–D are very similar, and only the stacking of the layers and sulphur differs. Structure E, with a dithiolane like molecule, appears to be plausible; however, following optimisation

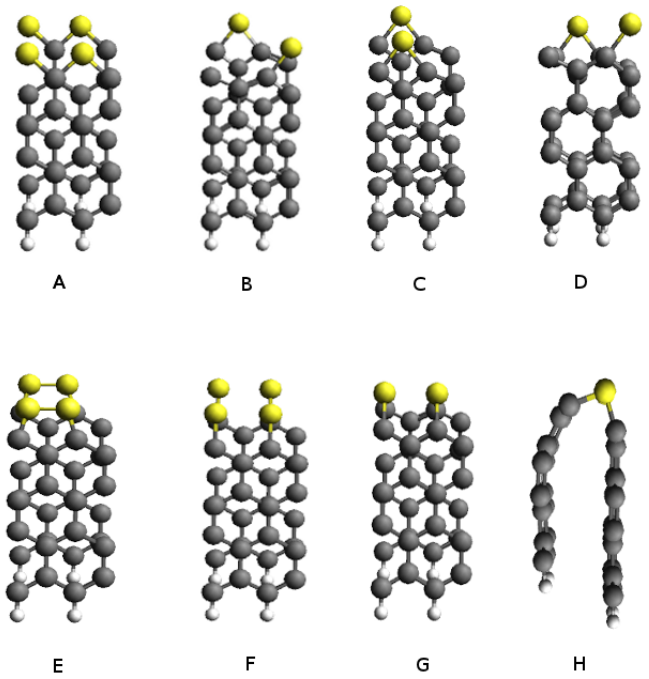

Figure 7.11: A–G: View in the prismatic direction of possible positions for sulphur (yellow) atoms on the carbon (grey) zigzag edge of graphite; H is G viewed along the edge. Carbon atoms are represented in grey, sulphur atoms in yellow and hydrogen atoms in white.

yields structure F, where the inner pair of S-S bonds are broken. Structure G differs from the others in the sense that sulphur links the two carbon sheets together. This forces one sheet to curve, as shown in H, which is the same as G viewed along the edge. Table 7.3 summarizes the results.

All the reactions investigated yield negative values for $\Delta H°$. The highest value is found for structure G and it is the only one where $\Delta H°$ is higher than for substitutional sulphur. Structure F is found to be the most energetically favourable, of all the configurations investigated, being lower in $\Delta H°$ by about 1.3 eV/C_{edge} relative to the next lowest configurations B and C. Interestingly, in structure G, the cross-link remains

Structure	Description	$\Delta H°$ (eV/C_{edge})
A	Substitutional sulphur	−1.34
B	AB stacking, Sulphur away	−1.73
C	AB stacking, Sulphur above each other	−1.73
D	AA stacking, Sulphur above each other	−1.70
F	AB stacking, 1,3 sulphur	−3.07
G	AB stacking, Cross-linking sulphur	−1.04

Table 7.3: Calculated heats of formation $\Delta H°$ for the structures illustrated in figure 7.11.

even after optimisation, even though it has a relatively high $\Delta H°$, compared with the other structures.

In order to investigate the formation of cross-link at the edge, two sulphur atoms were used to bind the two layers together, instead of one sulphur atom as for structure G. However, after optimisation, the cross-links disappear and the structure becomes similar to F. These calculations demonstrate that additional sulphur atoms on a graphite edge is more favourable than as substitutional atoms, and they can also stabilise the edges.

7.3.4.3 Remarks on armchair edges for additional sulphur

Many other configurations have been investigated for the armchair edge in the present work. The configurations with the lowest $\Delta H°$ are illustrated in figure 7.12.

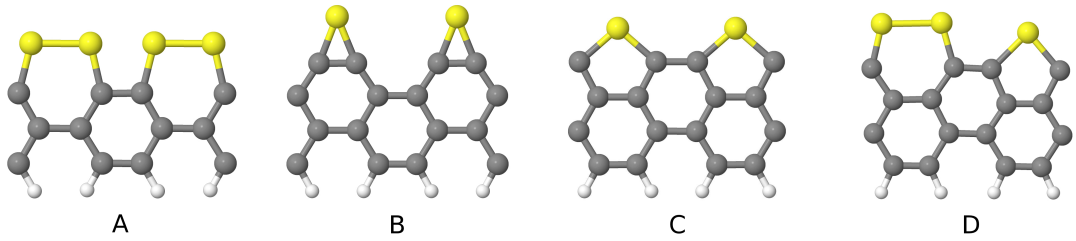

Figure 7.12: Structure with the lowest $\Delta H°$ on an armchair edge.

The four structures gives negative $\Delta H°$. The highest value is found for substitutional sulphur. Structure C is found to be the most energetically favourable of all the configurations studied. The $\Delta H°$ is -1.52 eV/C_{edge}. The energies for the remaining structures are presented in table 7.4.

Structure	Description	$\Delta H°$ (eV/C_{edge})
A	Substitutional sulphur	-1.03
B	'Epoxy-like' sulphur	-0.33
C	One sulphur atom bridge	-1.52
D	One and two sulphur atoms bridge	-1.62

Table 7.4: Calculated heats of formation $\Delta H°$ for the structures illustrated in figure 7.12.

Although the $\Delta H°$ calculated for these structures are negative, these reactions are relatively less favourable than the additional sulphur structure F calculated in the previous section.

7.3.5 Sulphur reaction with reconstructed edges, and the opening of folds in graphite

The following ribbons structures have been constructed, and optimised using the AIMPRO method. An orthorhombic cell with two layers, containing 64 atoms of carbon each, is only repeated in one direction of the basal plane, with one side of the ribbon terminated with eight hydrogen atoms. In the following calculations the Brillouin zone was sampled using the Monkhorst and Pack scheme with a sampling of $4\times4\times2$. The basis sets *pdpp*, *dddd* and *ppp* are used for carbon, sulphur and hydrogen atoms respectively. The states are occupied according to the first-order Methfessel-Paxton scheme with $kT = 0.01$ eV .

According to the present AIMPRO calculations, the formation energy for the reconstructed bilayer edge with respect to two unbound zigzag graphite edges is about -0.62 eV. The stacking following the fold is found to be AB instead of AA which was suggested previously by other theoretical work [185]. However, the difference could arise from the folding axes used [171].

Only the most favourable sites for sulphur inside and on the edges of graphite have been investigated so far. The aim of this section is to find a role for sulphur which could enhance the graphitisation process (type II). The hypothesis that sulphur, when it is released, can help folds to open is investigated. It might then be able to stabilise the edges before it is removed at higher temperatures, and this would allow the layers to reorient themselves.

The results given in table 7.5 represent the heat of formation ΔH for the model structures illustrated in figure 7.11, but are now calculated with respect to reconstructed edges rather than open edges. Only structures F and G have negative ΔH, with the 1,3-sulphur being the lowest. These values seem to support the proposal that sulphur atoms can help folds to open.

In order to verify this hypothesis, further calculations are necessary. Mechanisms, which involve the reconstructed edge and S_2 molecules, are investigated by employing the nudged elastic band (NEB) method to find reaction paths, transition states, and any energy barriers related to the process.

Structure from 7.11	ΔH from reconstructed edge(eV)
A	0.59
B and C	0.40
D	0.63
F	-1.13
G	-0.31

Table 7.5: Calculated heats of formation $\Delta H°$ for the structures illustrated in figure 7.11 calculated with respect to a reconstructed edge.

7.3.5.1 The first S_2 molecule

The main steps are illustrated in figure 7.13, and any references to images in this subsection refer to this figure. Each step is shown from different directions. The path for the reaction begins with a S_2 molecule in a location far away from the fold. As the molecule approaches the fold, it starts to interact with the folded edge. One sulphur atom attaches to one carbon atom present inside the fold. No bonds are broken, but the molecule is now linked to the fold (shown in 1), and the triplet state of S_2 vanishes. The next step is a rearrangement of the second sulphur atom, and its reaction with its nearest carbon atom (shown in 2). Between the structure 1 and 2 there is a small barrier about 0.30 eV in height. At temperatures above 1500 °C, as used in a graphitization furnace, this small barrier is insignificant. Once structure 2 is formed, the carbon-carbon bond, forming the fold is broken, as shown in 3. This process represents the first step for the fold to open. If the extent of the fold is large, then a single S_2 molecule is insufficient to break the other C-C bond inside the fold, and the S-S bond remains. The final image in figure 7.13 shows the energy curve for a single S_2 reacting with the reconstructed edge.

It is remarkable to see that the C-C bond inside the fold breaks easily once sulphur has reacted, considering that the dissociation energy for a C-C bond in graphite is around 7 eV [186].

The next step is to investigate the addition of a second sulphur molecule to the folded edge.

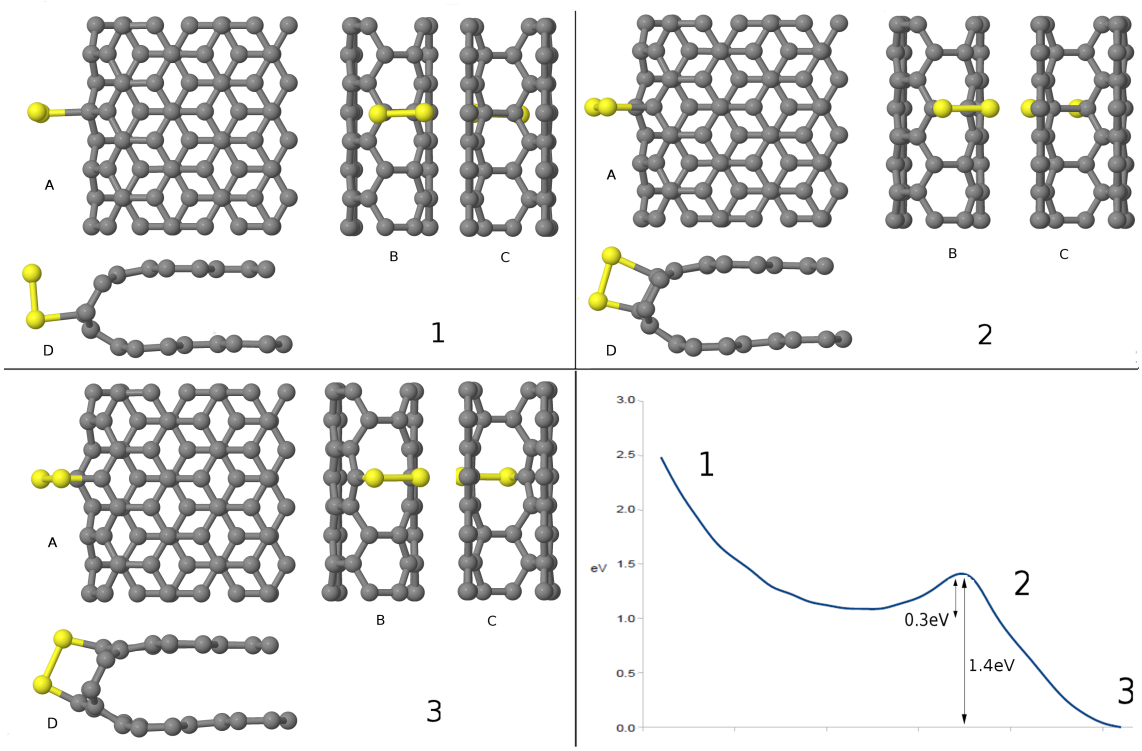

Figure 7.13: Reaction of S_2 with a fold. Four different views of each structure are shown: A is along the prismatic direction, B is from outside the fold along the armchair direction, C is from the opposite direction to B, and D is along the zigzag direction. The bottom right panel is a graph of the energy versus NEB reaction coordinate.

7.3.5.2 The second S_2 molecule

The path for the reaction begins with a S_2 molecule in a location far away from the fold from figure 7.13–3. As the molecule approaches the fold, it starts to interact. Two different sites of the folded edge can be investigated in this case. The S_2 molecule can either interact with the folded edge on a site next to the inserted S_2 molecule, or on a site away from the molecule. The most energetically favoured reaction is shown first. This is illustrated in three images in figure 7.14. While the first S_2 molecule is part of the fold and does not move, the second molecule interacts by following a similar path to the reaction descibed in section 7.3.5.1, as shown in figure 7.14–2. Once it is fully attached, the coplanar S-S bonds are broken to form new interplanar S-S bonds (shown in 3).

The fold has now started to open. This reaction has also a small barrier of about 0.53 eV in height, which is slightly more than the first S_2 reaction. The higher energy barrier could arise from a sulphur-sulphur repulsion created between the two

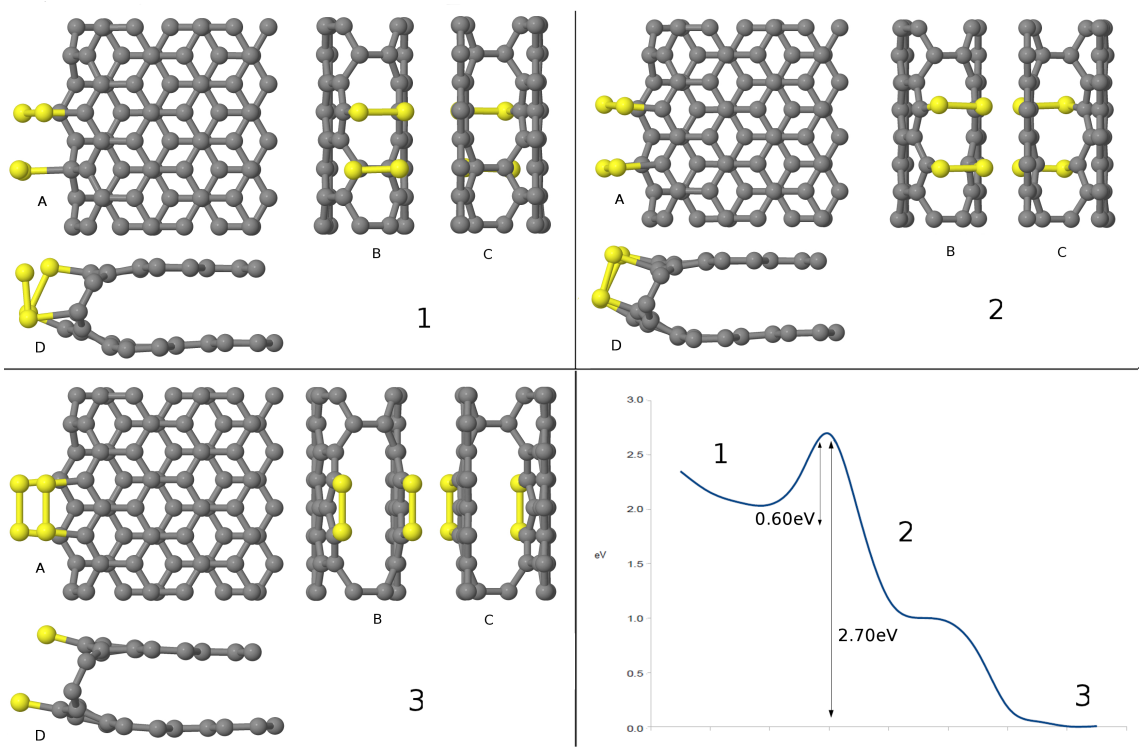

Figure 7.14: Reaction of the second S_2 molecule with a fold. Four different views of each structure are shown: A is along the prismatic direction, B is from outside the fold along the armchair direction, C is from the opposite direction to B, and D is along the zigzag direction. The bottom right panel is a graph of the energy versus NEB reaction coordinate.

S_2 units, which occurs on the path (shown in image 2). Following this, a reversal of the pairing for the sulphur atoms occurs, breaking the S-S bonds in both of the original two S_2 units, and creating two pentagonal rings, at the end of the reaction. Pentagon formation did not occur when sulphur was an ad-atom on the zigzag edge, as described in section 7.3.4.

The second possible route, where the incoming S_2 molecule binds at the next neighbouring site along the edge, has an energy barrier of about 0.30 eV in height. The final structure takes the same form as for the first S_2 molecule. However, this structure is almost 2 eV higher in energy to the pentagon-pair form. Thus, at high temperatures, it can be concluded that the first route is likely to be predominant.

7.3.5.3 The following S_2 molecules

With the addition of two S_2 molecules, the fold is now partially open. The next logical step is to investigate the addition of a third, then fourth sulphur molecule to

the folded edge. Two different sites on the folded edge can be investigated for the third S_2 molecule, in a similar way to the second S_2. Only the most energetically favoured reaction is shown here. This occurs when the molecule interacts with the C-C bond next to sulphur atoms on the edge. The third molecule follows a similar path to the reaction described for the first two S_2 molecules. The energy barrier for the third molecule is estimated to be only about 0.05 eV. Figure 7.15–A illustrates the final structure. The length between two carbon atoms on the zigzag edge is about 2.45 Å. It might be expected that the distance between two sulphur atoms is similar; however, it is found they are separated by about 2.34 Å. In figure 7.15–A, it can be seen that each group of three sulphur atoms on each sheet are attracted to each other.

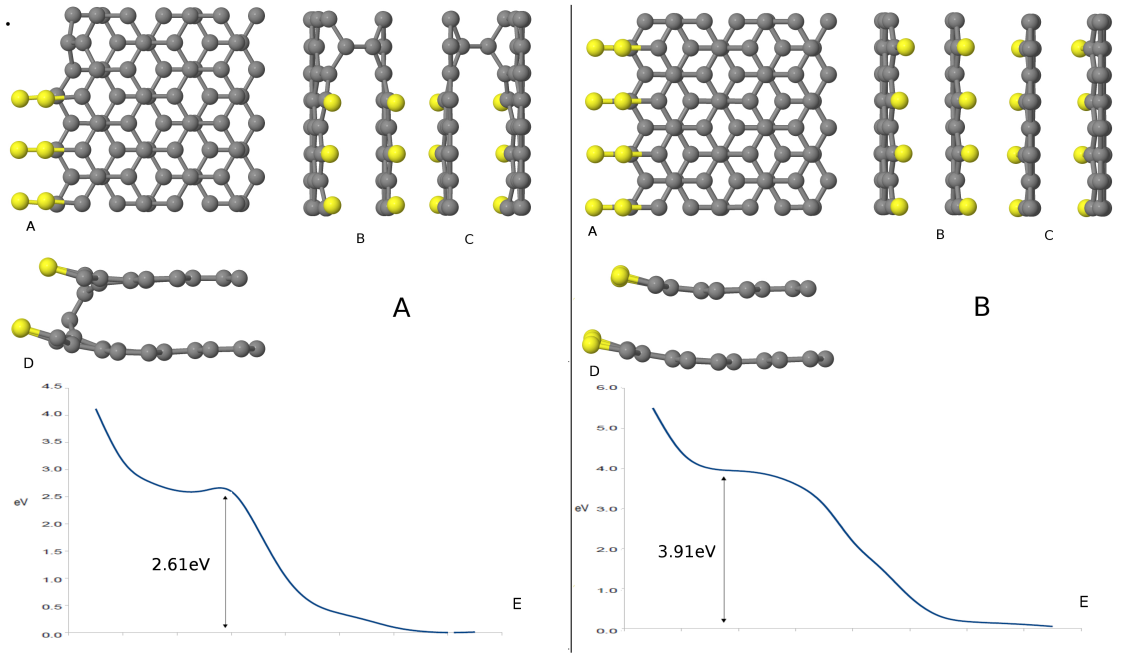

Figure 7.15: Reaction of third and fouth S_2 molecules with a fold. (A) Final structure following the reaction of the third S_2 molecule: A is viewed along the prismatic direction, B is from outside the fold along the armchair direction, C is from the opposite direction to B, and D is along the zigzag direction. E is a graph of the energy versus NEB reaction coordinate. (B) Final structure following the reaction of the fourth S_2 molecule: A is viewed along the prismatic direction, B is from outside the fold along the armchair direction, C is from the opposite direction to B, and D is along the zigzag direction. E is a graph of the energy versus NEB reaction coordinate.

The final structure with four S_2 units is shown in figure 7.15–B. It is very similar to the structure F in figure 7.11. This reaction has no energy barrier. The sulphur atoms on each plane are now separated by 2.45 Å. The fold is now fully open: no

C-C bonds remain between the two sheets.

To conclude, this section has shown a new role for sulphur. Unfolding layers is a crucial step for the reorganisation of the layers, and sulphur is able to enhance it.

7.3.6 Sulphur and prismatic edge dislocation

A fold embedded in graphite is a perfect prismatic dislocation. It has Burgers (slip) vector, b, equal to the lattice vector c since it comprises two added half planes (an A and a B plane). The elastic energy per unit length of a dislocation is proportional to the square of the Burgers vector, b. If it is possible to form a low energy stacking fault in the glide plane of the dislocation; it is usually thermodynamically desirable for it to split into two dislocations ('dissociation') whose Burgers vectors sum to the original one, b. A single extra half plane is a 'partial' dislocation with Burgers vector $c/2$ and hence apart from the cost of the stacking fault and repulsion between the partials, the energy saving upon dissociation is proportional to $b^2-(b/2)^2-(b/2)^2$ which is substantial and positive. The hypothesis that sulphur, once it has opened a fold when, can help two neighbouring prismatic dislocation to move apart is investigated. An illustration of this mechanism is shown in figure 7.16.

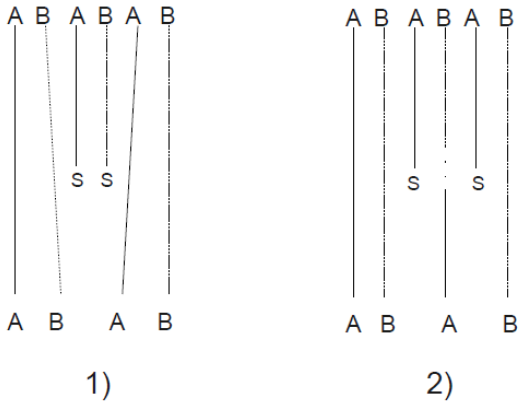

Figure 7.16: Schematic representations of: 1) an opened fold via sulphur; 2) more stable structure with two partial disclocations. The stacking fault between two half plane is represented by the long dotted lines.

A graphene sheet, terminated by sulphur at the end of a zigzag edge, as it has been described in structure F of figure 7.11, is placed between layers of graphite.

The structure is optimised. The complexities of dissociation of a perfect prismatic dislocation have not been worked out yet, especially in the case of HOPG where each graphite layer is a patchwork of crystallites. Further calculations are required. However, if sulfur does help prismatic dislocations move, similar transitional structures shown in figure 7.7 are expected to occur, as seen in the literature for undecorated edges [187].

7.3.7 The release of hydrogen sulphide during graphitisation

The aim of this section is to investigate a possible mechanism which involves the release of hydrogen sulphide. The results of calculations show that there is a relatively low energy barrier for this process. A model based on the dissociation of a molecular fragment, which contains a pair of sulphur atoms, is used here. Equation 7.3 defines the reaction, in which an H_2S molecule is released, leaving the remaining sulphur atom on the fragment.

$$C_6H_6SSH \longrightarrow C_6H_5S + H_2S. \tag{7.3}$$

The energy curve for the release of H_2S, calculated using the NEB method, is shown in figure 7.17. The initial, final, and transition state structures are also illustrated. The reaction begins with a relatively stable molecule. As the reaction progresses, the S-S bond in the molecule is broken. The activation energy required for this is about 0.65 eV. At this point, the departing S-H radical binds to an H atom from the original molecule, breaking a C-H bond in the process, and subsequently forms H_2S.

7.3.8 Conclusion

This chapter reviews the impurity sulphur in the process of graphitisation. The literature provides significant information on the different role played by sulphur during graphitisation. One possible role is the formation of sulphur cross-links between layers of graphite. The present study appears to be inconsistent with the idea that sulphur is present in the form of defect complexes cross-linking layers in well-graphitised carbon, owing to the high value found for ΔH° by the calculations.

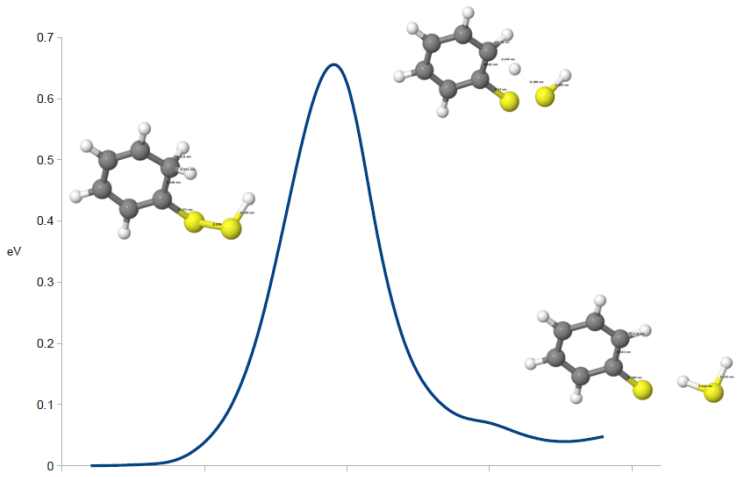

Figure 7.17: Graph of the energy versus NEB reaction coordinate for release of H_2S from a molecular fragment representing the edge of a larger molecule in the precursor material.

Furthermore, calculations have shown that the edges of graphite are a more favourable site for sulphur, owing to the lower value found for $\Delta H°$. According to the literature, substitutional sulphur atoms, or thiophenic like molecules, found in petroleum, have been described as molecules which can promote the process of graphitisation. The calculations presented in this chapter also suggest that sulphur can easily react with zigzag and armchair edges when being released during the graphitisation process. Our calculations do not refute that sulfur can form cross-linkers, which can be present in cokes of smaller LMO, in the early stages of the process. However, the remaining sulfur in the late stage, according to calculations, does not come from cross-linkers but from another type of sulfur. New roles for sulphur are also proposed. The first one concerns the ability of sulphur to open folds. Only a small activation energy is needed for the chain reaction to occur. The second role, is the possibility that prismatic dislocations may move more easily when sulphur is attached to their edge. When sulphur is found on the edge, it could be described as the type III state, defined by Bourrat [158], instead of within cross-links. Sulphur is not expected, in these situations to leave at low temperatures.

Chapter 8

The role of Boron

Sulphur is the main impurity atom considered so far. The subject of this chapter is boron. It occupies the fifth position (atomic number 5) in the periodic table, and is a group III element, having properties of both metals and non-metals. Boron has two stable isotopes: ^{11}B (80.1%) and ^{10}B (19.9%), which gives it an mean atomic weight of 10.811 $g\,mol^{-1}$. Its electron configuration, $1s^2 2s^2 2p^1$, means it can form covalent bonds with its three available valence electrons. The energy released by the formation of three bonds is much higher than the energy of formation of a single bond. Naturally occurring single crystals of graphite contain ~10 *ppm* of boron [188]. Many other types of atoms or molecules can be forced in the graphite lattice, but they are mostly found as interstitial impurities [189]. Boron, however, is an unusual species, since it can dope graphite as a substitutional atom [190]. This chapter discusses the role of boron in graphitisation and radiation damage by reviewing its stability, its preferential sites, and its electronic effect inside the hexagonal structure of graphite. Its ability to form strong bonds with its three neighbouring carbon atoms when substitutional, and also its effect on the elastic constant C_{44} are described. A paragraph on the role of boron inside a nuclear reactor is presented first.

8.1 The history of boron

8.1.1 In nuclear reactor

Graphitisation gives a relatively pure material; however, when used in nuclear reactors, even a small concentration of impurities, especially the ones with high cross-section for neutron capture, can have an undesired effect [137]. Boron is one of the unfavourable, and most difficult impurities to remove from the graphite lattice; hence, the purification step following the final graphitisation is crucial [137]. Nevertheless, boron also plays a major role in a fission reactor for controlling the reactivity. When uranium is used as a fuel, it releases typically two or three neutrons. Only one is needed to sustain the chain reaction, while the excess are absorbed in non-fission reactions. The boron isotope, ^{10}B, is used in neutron absorbing control rods due to its high cross-section for neutron capture [191, 192]. Thus, when the rods are slightly removed from their original position, the number of neutrons available increases and hence the power level increases. Once a desired power is reached, the control rods are returned to their position and the power stabilises. For some types of reactors, a small amount of boron may be added intentionally to the cooling water. For emergency situations, rapidly adding an excessive quantity of boron to the water can also be done. In graphite-cored nuclear reactors, however, the control rods are normally the only intentional neutron-absorbing material present. Boron has never been found in irradiated graphite used in fission reactors [191].

8.1.2 In graphitisation

A few reports can been found in the literature of experiments on the role of boron during the graphitisation process [193, 194, 195]. A catalytic effect on the rate of graphitisation was observed in some of the experiments [193]. Murty *et al.* were the first to report this catalytic effect at various concentrations of boron, but also as a function of heat treatment, time and temperature [194]. It was found that, when boron is present at a concentration of about 0.5–1 wt.%, the normal d_{002} interlayer spacing of graphite is reached at lower temperature (by about 400 °–500 °C) than for a graphitic carbon without boron. Furthermore, according to Murty *et al.* at higher

concentrations to up to about 5 wt.%, the catalytic effect saturates, meaning no further lowering of the temperature necessary for graphitisation to occur is observed. In these experiments, it is only the rate of graphitisation that changes, and not the activation energy. Kotlensky found similar results to these for low concentrations, but he also concluded that concentrations higher than 1 wt.% can, to some extent, even inhibit graphitisation [195]. It was demonstrated that the equilibrium solid solubility, of 2.12 wt.% at 2350 °C (see section 8.2), is not dependent on the initial carbon coke, whereas the extent and rate of catalysis at a given boron level depends on the initial structure [194]. Oya *et al.* came to the conclusion that the presence of boron, mainly as a substitutional impurity, augments the rate of graphitisation [194].

Oya *et al.* [193] classified the catalytic effect of boron according to its concentration, and described that when less than 1 wt.% of boron is added to carbon, it becomes substitutional, and it results in a well-graphitised carbon. When 1 to 5 wt.% of boron is present, in a non-graphitising carbon, the formation of a more 'ordered' turbostratic structure is observed on heating to temperature of about 2200 °C. When 10 wt.% of boron is present in a phenolic resin carbon, a well ordered structure is observed at temperature of about 2400 °C. They also reported the catalytic action of boron or boron oxide for other carbons [193]. According to Trask, the addition of at least 3 wt.% of boron into synthetic graphite from petroleum coke and coal-tar pitch binder, enhanced the crystallinity of graphite, improved its oxidation resistance, and decreased the coefficient of thermal expansion (CTE) without causing any deterioration in the flexural strength [196]. This was also found by Hagio *et al.*, and they explained that the effect on CTE was mainly caused by a distortion of the graphite lattice due to boron [197]. Addition of 1 wt.% of boron to pyrolytic graphite formed at about 1500 °C also considerably improved the oxidation resistance. This doped pyrolytic graphite had a high density, $p = 2.19\ g\,cm^{-3}$, a value of the order parameter $L_c = 15.8\ nm$, and a highly preferred orientation of crystallites.

8.1.3 In radiation damage

In the last section of Chapter 1, 1.3, it was explained that prismatic interstitial dislocation loops are formed after radiation. An early experiment reported the possible

influence of boron in the formation of loops [198]. Later experiments demonstrated that when irradiated graphite single crystals are doped with boron and heated to temperature as high as 2100 °C, then large interstitial loops are formed [199]. An example is shown in figure 8.1.

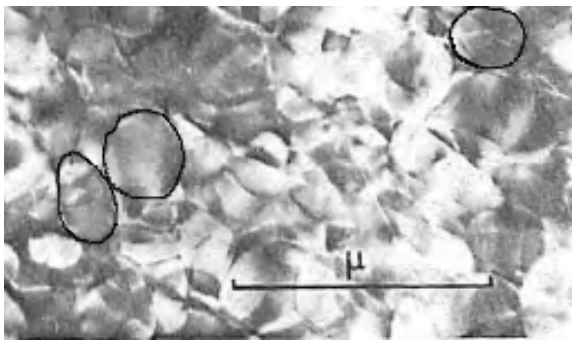

Figure 8.1: Electron microscope image of interstitial-type loops produced in boron-doped graphite annealed to high temperature, taken from [200]. Some of the loops are highlighted with a black circle.

And even at different neutron doses, the density of the loops increases when more boron is present. There is also a dependence of their radius with the boron content; mathematical equations related to this can be found in Kelly and Mayer's paper [201]. A theory was established by Brown *et al.* which explains the role of boron in irradiated samples [202]. According to their calculations, the nucleation and growth of interstitial loops in highly oriented pyrolytic graphite (HOPG) shows Arrhenius dependence of ~ 1.2 eV. Brown *et al.* concluded that boron, ^{11}B, can enhance the effect of radiation damage due to its very high cross-section for elastic collisions, an effect which was explored to accelerate damage in material test reactors [192]. Unfortunately, it was not easy to interpret the results of these experiments and the idea was dropped.

Another interesting feature of boron in graphite is its effect on the elastic constant C_{44} [203]. There is a curious similarity between B-doping and radiation damage: both push up the measured value of the shear modulus, C_{44}, to the values generally accepted for a perfect AB stacked graphite crystal (i.e. 4–5 GPa) [204, 205].

Generally, without either doping or damage, C_{44} is found to be very small for a well graphitised synthetic sample or for natural graphite (i.e. 0.25–1.2 GPa) [206]. The reason is often attributed to extra compliance arising from reversible motion of basal dislocations. Since the Peierls stress for these is zero [207], reversible motion

is possible. Another interpretation is that these natural and good synthetic samples have [002] twist boundaries and these have very flat gamma surfaces and hence very low C_{44} [208, 209]. This is pushed up to the perfect crystal C_{44} value (4–5 GPa) by pinning these boundaries, meaning that the gamma surface is not flat in these cases. It appears to be inhibited by radiation damage [210] and by boron [203]. The origin of the radiation damage effect has been generally associated with cross-linking defects (e.g. interstitials) preventing slip, but it is difficult to understand this for boron doping, since it is a substitutional impurity and not cross-linking. Our calculations later will show how substitutional boron atom causes pinning without cross-linking.

8.2 Review of the stability, effect, and diffusion of boron in the graphite lattice

The solubility of solid boron in graphite has been determined by Lowell from the boron-carbon phase diagram [211]. Lowell found that boron is substitutional with a maximum solubility of 2.12 wt.% at 2350 °C, and its effects on the lattice constants can be described by the two following equations:

$$a_0 \ (\text{Å}) = 2.46023 + 0.0031 K_B$$

for the a lattice parameter and

$$c_0 \ (\text{Å}) = 6.71163 - 0.00594 K_B$$

for the c lattice parameter, with K_B the atomic fraction of dissolved boron in both equations.

The minimum lattice constant occurs at 2350 °C. Turnbull *et al.* also studied amorphous boron diffusing into a reactor-grade graphite [188]. They produced single crystals of graphite containing up to 4 wt.% boron, and claimed that at this concentration boron must occupy both interstitial and substitutional sites. They concluded that interstitial atoms generate expansion in the prismatic direction with no apparent effect on the basal direction, whereas substitutional boron creates a c-axis contraction and an a-axis

expansion. The interstitial boron atoms escape from the crystal at temperatures around 1400 °C, while the substitutional boron atoms remain stable. The high value for the *c*-parameter due to the interstitial atoms now decreases. Only substitutional atoms remain, and the d_{002} is now smaller than the normal graphite value. When the temperature is above 2000 °C, the substitutional boron is able to diffuse, and the lattice parameters return to their normal values for graphite [188]. Wagner and Dickinson also observed a decrease of the interlayer spacing with concentration of boron of up to 0.79 wt.% with the crystallites size (L_c) unaffected [212].

Another group found similar results: doping graphite, with 0.6 wt.% and 1.5 wt.% boron, changed the lattice parameters [213]. They also took Raman spectra of boron-doped graphite, and observed an increase in intensity of the 1360 cm^{-1} D-mode, implying that defects are present (chapter 5, section 5.2.1), or at least, that substitutional boron atoms manage to break the symmetry mode enough for it to be Raman-allowed.

Hennig measured the mobility of substitutional boron atoms in a single crystal [214]. He found that the activation energies for the migration of boron in the prismatic and basal directions are similar, and are about 6.7 eV. He employed the following equation to determine the diffusion coefficient, D^B, in the two directions:

$$D^B = D_0 exp(-E_a/k_B T)$$

where D_0 is the self-diffusion constant, E_a is the activation energy for migration, and T is the temperature. The values of D_0 and E_a measured by Hennig are shown in table 8.1. Using this equation, at 1800 °C, the diffusion coefficient is a factor 350 greater in the basal plane. Suarez-Martinez *et al.* studied the boron interaction with point defects in graphite and its possible diffusion route [215]. They concluded that a kick-out mechanism is responsible for the diffusion of boron, in both the prismatic and basal directions. In addition, their calculations showed that the activation energy for its diffusion was controlled by the formation and migration of interstitial carbon atoms.

The diffusion constants for carbon atoms are calculated to be significantly lower than

Diffusion	$D_0(\mathrm{cm^2\,s^{-1}})$	E_a (eV)
Boron along *a*-axis	6320	6.78
Boron along *c*-axis	7.1	6.61
Carbon self-diffusion along *a*-axis	0.4–14	6.99

Table 8.1: Experimental values for the self-diffusion constants and activation energies of boron in graphite, taken from [215]

for boron atoms [215]. The parameters for carbon atom self-diffusion in graphite in the basal direction were first measured by Kanter (table 8.1) [216]. Later experiments found good agreement with those values (1.81 $\mathrm{cm^2\,s^{-1}}$) and also measured a value of 82.8 $\mathrm{cm^2\,s^{-1}}$ in the prismatic direction [217]. If boron and carbon atoms diffuse via a similar mechanism, then boron atoms could increase the rate of graphitisation due the relatively higher diffusivity of boron over carbon in the graphite lattice.

The literature provides significant information on the various effects that boron has when present as an impurity in graphite. This has stimulated research into new boronated carbon compounds. A material with the composition BC_3 has been synthesised by reacting benzene and boron trichloride at about 800 °C [218]. LDA calculations predict that BC_3 is a stable, semiconducting compound with a hexagonal lattice, arranged in layers, similar to graphite, and where the primitive unit cell contains eight atoms [219]. However, this concentration cannot be expected after graphitisation, as most of the boron would be removed. Nevertheless, the synthesis of BC_3, supported by theory, represents further evidence of the ability of boron to be incorporated as a substitutional atom within graphite.

8.2.1 As a substitutional

When boron is added to graphite during heat treatment, it can diffuse in the lattice and find a vacancy site to occupy, with a preference for less ordered regions [220, 221]. Another group confirmed that a boron atom becomes substitutional more easily when it undergoes graphitisation, since it can form new B-C bonds at the defective sites removal by diffusion of other impurities [222]. It is believed to be difficult for boron atoms to enter the graphite lattice at temperature below 2000 °C due its high activation energy, unless the host material has been irradiated first [200]. Previous LDA calculations give the formation energy of substitutional boron atoms to be

1.4 eV [215].

8.2.2 As an interstitial

When boron is added to carbon, either as elemental boron or as boric acid, boron atoms may become interstitial before they react with available vacancy sites [222, 223]. The same occurs when substitutional boron atoms trap interstitial carbon atoms, and become interstitial boron atoms in the process [215]. It is also believed that boron atoms, at a higher concentration than described by Lowell, might exist as interstitials [188]. Unfortunately, the exact concentration and the mechanisms involved for interstitial boron atoms are unclear. Previous LDA calculations give the formation energy of interstitial boron atoms to be 4.5 eV [215]. This high formation energy rules out interstitial boron atom as an equilibrium defect of any importance. However, it has been suggested that their effect on the lattice parameter c cannot be ignored [188]. It should be noted that carbon spiro-interstitial defects give very little c-axis expansion [224], but there are mechanisms (e.g. pinning basal dislocations and buckling [225]) by which c can be increased.

8.3 Calculation

8.3.1 As a substitutional

The aim of this section is to investigate, using the AIMPRO package, models for substitutional boron atom in graphite. This includes varying the concentration of boron to examine what effect this has. The size of boron is smaller than carbon or sulphur atoms; thus, it is expected that substitutional boron forms a high-symmetry on-site defect centre, rather than off-site. The unit cells used in the following calculation contain either 4×4×1 or 7×7×1 orthorhombic supercells. This means that for these two models, the concentration is either 0.6 or 1.5 at.%, respectively. In the following work, the Brillouin zone was sampled using the Monkhorst and Pack scheme with a sampling of $6 \times 6 \times 4$. The basis sets pdpp and pdpp are used for carbon and boron atoms respectively. The states are occupied according to the first-order Methfessel-Paxton

scheme with kT = 0.01 eV. The calculations confirm that the on-site configuration is the one favoured for substitutional boron. This illustrated in figure 8.2. Thus, the impurity atom is found to be threefold coordinated with D_3h symmetry.

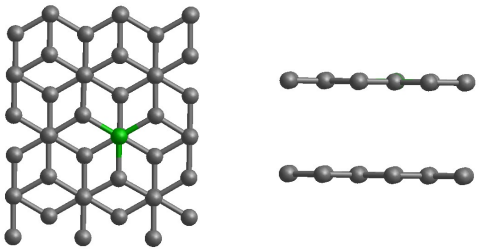

Figure 8.2: Structure of a substitutional boron atom within a graphite layer on a β site, optimised by the AIMPRO program package.

A substitutional boron atom has an influence on its neighbouring carbon atoms. The three B-C bonds are longer (1.468 Å) than a normal C-C bond (1.411 Å), while the next neighbouring C-C bonds are slightly shorter (1.395 Å), according to the calculations. The predicted B-C bond lengths are in good agreement with their values determined by Raman scattering experiments on boron-doped graphite (1.48 Å) [226].

The difference in energy for a single boron atom placed on an α or a β site is negligible (20–30 meV, see 8.2). However, the formation energy shows that boron is more easily inserted at lower concentration, according to the calculations. A summary of the results is shown in table 8.2.

The next models investigate the possible segregation of boron atoms by placing two substitutional atoms in a 64-atom supercell, arranged in eight different ways. The impurity concentration for this model system is 3 at.%. Four different models can be generated for boron atoms in the same graphene sheet on different α and β sites. The formation energy for the nearest neighbouring α-β pair is higher by nearly 1 eV compared with any other models investigated. This means that the formation of boron dimers in graphite is unlikely. When two boron atoms are separated by at least a few C-C bonds, no differences in formation energies between α and β are predicted. When the boron atoms occupy different sheets, the calculations predict that there is negligible interaction, meaning that the formation energy is simply double the formation energy of a single substitutional boron atom in the same cell. However, the calculations find that pairs of substitutional boron atoms in different sheets are slightly more stable, by

about 0.25 eV, than when they are coplanar. This effect can be understood in terms of the increase of the density of states arising from the shift in the Fermi level when boron is added. Further details are given later in section 8.4.2.6.

A summary of the results for substitutional boron is provided in table 8.2. All the formation energies are calculated with respect to the rhombohedral crystalline form of icosahedral-B_{12}, and hexagonal graphite.

Description	at.%B	carbon site(s)	formation energy (eV)
Single boron atom only	0.6	α	0.73
		β	0.76
	1.5	α	0.89
		β	0.87
Two coplanar boron atoms	3.0	$\alpha\beta$ neighbours	2.99
		$\alpha\beta$ separate	2.07
		$\alpha\alpha$ separate	2.07
		$\beta\beta$ separate	2.06
Two boron atoms in different sheets	3.0	$\alpha\alpha$ neighbour	1.80
		$\alpha\alpha$ separate	1.84
		$\alpha\beta$ separate	1.81
		$\beta\beta$ separate	1.78

Table 8.2: Formation energies calculated using the AIMPRO package for substitutional boron in graphite at different concentrations, in different configurations. For two boron atoms in a supercell, 'separate' means that they are not on neighbouring sites and there is a distance of at least 6 Å between them.

Thus, for models containing 3 at.% B, no preferential sites, and no clustering is predicted, in good agreement with experiments using B-NMR, which show that isolated boron atoms are dominant at low boron concentration. However, increasing numbers of B-B near neighbours are detected as the boron content increases [227]. The effect of boron on the lattice parameters with the same model has also been also investigated. The results confirm an increase in the a lattice parameter and a decrease in the c lattice parameters. However, the calculated values are relatively small: 0.52% increase in the basal direction and 1.03% decrease in the prismatic directions at 3 at.% B. These values sensibly change as the concentration decreases. They follow Vegard's law [228], which is an approximate empirical formula which explains that there is a linear relationship between the crystal lattice constant of an alloy and the concentrations of the constituent elements at constant temperature. This is also in reasonable agreement with experiment [213]; the a-axis parameter is increased by 0.1% and the c-axis parameter is decreased by 0.12% at 0.6 wt.%

8.3.2 As an interstitial

The following model has been constructed in a supercell and calculations were performed using the same input parameters as the previous section. A single boron atom is placed midway between the two graphene sheets in AB graphite with 32 carbon atoms each. After optimisation, two structures are found to be relatively stable: a threefold interstitial boron atom with the layers in ABAB stacking, and a fourfold 'spiro' interstitial boron atom with a shear of one of the layers in the basal direction. The 'spiro' interstitial model is slightly lower in energy, by 0.2 eV, compared to the threefold model. The formation energy for the spiro model is 4.5 eV; hence is higher than the formation energy of a substitutional boron atom (0.87 eV). An illustration of the spiro-configuration is shown in figure 8.3. A significant distortion can be observed in this figure but the increase of the lattice parameter c is only 0.35% with respect to normal graphite. The four B-C bonds are 1.585 Å, the two C-C bonds forming two triangles with the boron atom are 1.508 Å, and both C-B-C angles are 58°. The interstitial boron atom causes a spontaneous relative translation of the graphene sheets along a $[10\bar{1}0]$ direction by about half a C-C bond length (left image in 8.3). This behaviour is similar to that for the spiro form of self-interstitial atoms in graphite [163].

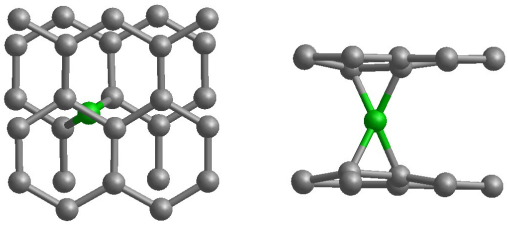

Figure 8.3: Structure of a interstitial boron atom between graphene sheets in hexagonal graphite, optimised by the AIMPRO program package.

8.3.3 As substitutional and interstitial pairs

The following models examine the stability of boron atom pairs, where one is substitutional and the other is a nearby interstitial. The unit cells contain 64 carbon atoms arranged as two graphene sheets in graphite. Two different configurations have been optimised by moving boron atoms from their interstitial and substitutional

positions. The first configuration has an interstitial boron atom located about 7 Å away from a substitutional atom, while the second case is sufficiently close for a B-B bond to exist between the pair. The bonded configuration is found to be lower energy by about 1.2 eV compared with the separate pair. The formation energy for this model is found to be approximately 3.69 eV, which is 0.8 eV lower in energy compared with the formation energy of a single interstitial. In this model, the B-B bond is 1.704 Å, the B-C bonds between the interstitial boron atom and the carbon atoms are 1.601 Å and the B-C bonds between the substitutional boron atom the carbon atoms are 1.504 Å. Also, unlike the isolated boron interstitial, no relative translation of the adjacent graphene sheets occurs: the stacking remains AB. The structure of a boron pair defect complex is illustrated in figure 8.4. Comparing formation energies of isolated interstitial boron atom and substitutional boron atom (4.5 eV and 0.9 eV), the binding energy is 5.4 eV-3.7 eV, and is equal to 1.7 eV. This complex does not appear to have been reported previously; however, its relatively low energy suggests that it may be possible for these defects to form, especially when the concentration of boron is high, or following suitable heat treatment.

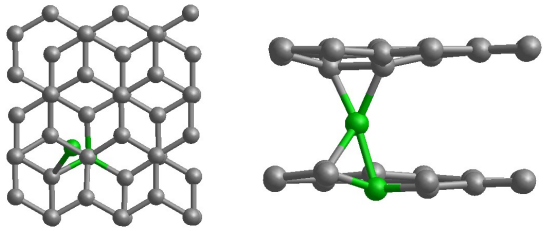

Figure 8.4: Illustration showing the structure of a split interstitial-substitutional boron defect complex in graphite, optimised by the AIMPRO program package.

8.3.4 Remarks

Model structures for defects containing boron as an impurity in graphite have been examined in this section, using the AIMPRO program package. The results of the calculations are in good agreement with previous work by others for isolated interstitial and substitutional boron atoms. A defect complex comprising a pair of boron atoms is also found. This structure, which does not seem to have been described in previous work, is predicted to have a relatively low energy, suggesting that it is likely to exist

when the circumstances are favourable.

8.4 Band structure of graphite with boron

The effect of doping on the electronic properties of a material can only be predicted provided that the dopant species perturbs the lattice and band structure of the host by a negligible amount. Boron in graphite is a good example since, at low concentrations, it has relatively little effect on the lattice parameters of graphite, suggesting that the band structure of the host is nearly unaffected by the presence of the impurity. In this section, the band structure of normal hexagonal graphite is calculated using the AIMPRO package, then compared with the band structure of model supercells when boron atoms are in substitutional states. The boron band structures were calculated from the optimised cells previously described.

8.4.1 Review of the electronic band structure

8.4.1.1 Graphite

The band structure of hexagonal graphite was first calculated in 1947 by Wallace and Coulson using a tight-binding approximation [229, 230]. Many later band structure calculations are in broad agreement; nevertheless, they do not necessarily interpret the results in the same way [137].

The Brillouin zone (BZ) zone of hexagonal graphite is a hexagonal prism, and its vectors can be determined from the primitive lattice vectors, where the real-space and reciprocal space basal lattice vectors are rotated by 60° with respect to each other. The BZ boundaries can be described with specific points. The standard parametrisation is due to Slonczewsky, Weiss and McCure [231, 232]. Further details are given in the appendix A, which includes an illustration of the full BZ.

8.4.1.2 Substitutional boron

The ability of graphite to accept boron as a substitutional atom was discussed previously. The main purpose of doping carbons is to change the position of the Fermi level, and introduce a possible charge transfer. This can either be electropositive, meaning an electron is added to one of the unoccupied π bands, which moves the Fermi level higher, or electronegative, having the opposite effect. Nitrogen atoms might reasonably be expected to be the only possible substitutional electron donors in carbon [233]; however, at temperatures of about 1700 °C, most substitutional nitrogen atoms in carbon materials have been lost by diffusion [234]. Nitrogen in carbon materials was also reviewed by Ewels and Glerup [235]. The electropositive effect usually occurs when atoms or molecules are intercalated between layers [233]. However, boron atoms are normally considered to be the only possible substitutional electron acceptors in carbon materials [233].

8.4.2 Band structures calculations

8.4.2.1 Graphite

Band structures shown in the present work follow a specific path around the BZ, i.e: $K \rightarrow \Gamma \rightarrow M \rightarrow K \rightarrow H \rightarrow A \rightarrow L$. Some of the low energy bands are omitted for clarity; only bands near the Fermi level are shown. For example, the band structure of a 64-atom graphite supercell is illustrated in figure 8.5.

The band structure calculated in the present work is similar to the results from previous theoretical studies [236]. Their band structure calculation for graphite is illustrated in figure 8.6.

Although 64 atoms have been used to match the later calculations, the energy bands can be more easily described with a primitive unit cell of four atoms. In the case of a four-atom cell, each carbon atom has four valence electrons, therefore there are sixteen energy levels, provided the spin is ignored (singlet). Twelve of these levels describe σ bands, and four other levels the π bands. Six of the σ bands are bonding orbitals, and the remaining six are anti-bonding orbitals. There are also two π-bonding

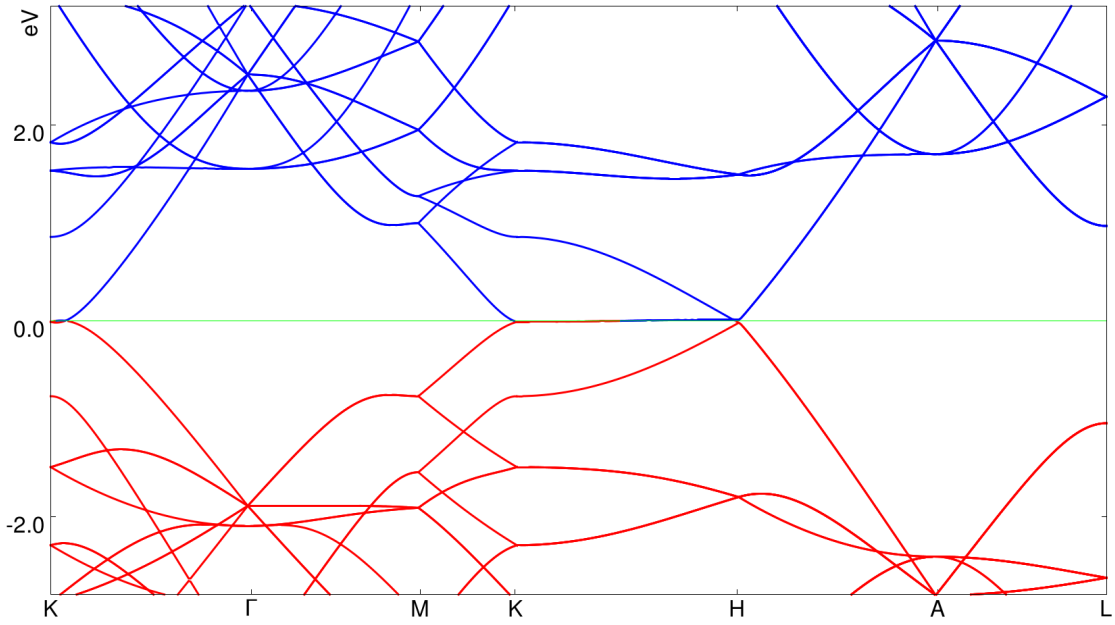

Figure 8.5: Band structure of a 64-atom graphite supercell containing two graphene sheets with AB stacking, optimised by the AIMPRO program package. The occupied bands are represented in red, and the unoccupied bands in dark blue. The Fermi level is depicted in green.

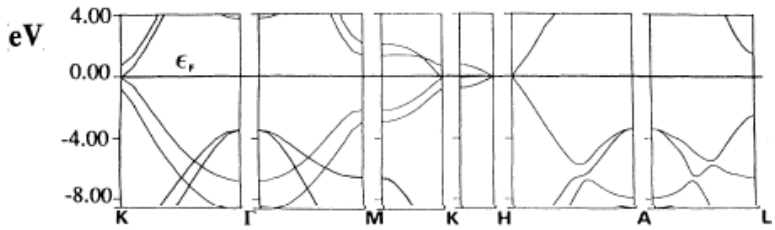

Figure 8.6: *Ab – initio* band structure of graphite along different lines in the Brillouin zone, taken from [236].

and two π-anti-bonding bands. The anti-bonding orbitals have higher energies than the bonding orbitals. Graphite has sixteen valence electrons available in its primitive unit cell, thus only eight energy bands are filled with two electrons (six σ and two π).

In figure 8.5, a large gap between the π-bonding band and the π-anti-bonding band can be seen at the Γ-point, a smaller gap at the *M*-point, and notably, no gap at the *K*-point. All these points lie in the basal plane crossing the centre of the BZ; however, a similar behaviour is observed at the *H*-, *A*-, and *L*-points, lying on the hexagonal faces of the BZ. The small overlap of the bands at *K* means that the two states at the Fermi level are degenerate. Graphite has many other degenerate bands. Another example can be seen at the *M*-point for the bands slightly above and below the Fermi

level. These two pairs of bands are split elsewhere in the BZ.

The bands at the *K*-point arise from combinations of the celebrated graphene states at the *K*-point, the Dirac point [2]. These two states are delocalised non-bonding wavefunctions, each sitting on one and only one of the two sublattices (see figure 8.7).

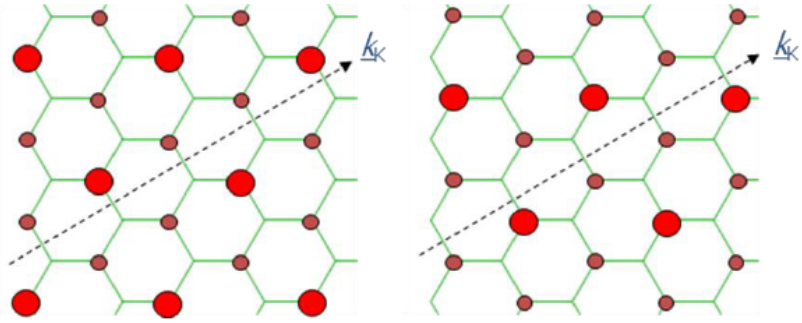

Figure 8.7: The two wavefunctions at the *K*-point on different sublattice. We label these α (left) and β (right). Large circles correspond to coefficient of +1 and small circles -$\frac{1}{2}$.

When graphene layers are stacked in AB fashion, the sublattices which are directly above one another in the *c*-direction (labelled α) are allowed to interact, by symmetry, but the β sublattices are not. Thus the graphene *K*-states on β sublattices remain non-bonding and degenerate along *K* to *H*, while the α states show dispersion along that direction as illustrated in figure 8.8.

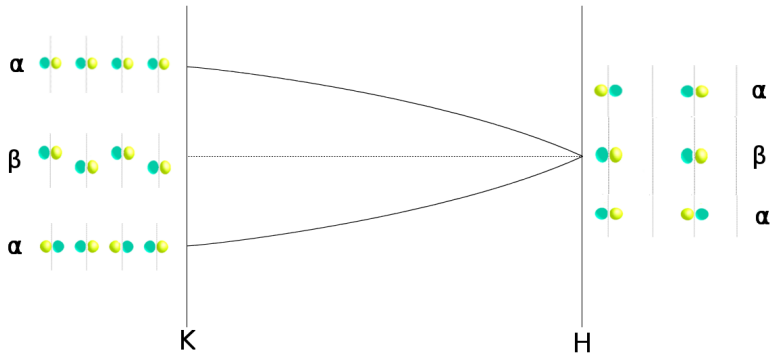

Figure 8.8: Schematic representation of the bonding, non-bonding, and anti-bonding orbitals, and their respective energy band between *H* and *K* in the BZ.

The electronic effect of substitutional boron atoms are investigated in the following sections by calculating their effect on the electronic band structure. A concentration of 1.5 at.% is used for the models, since this value is close to maximum substitutional

boron concentration described by Lowell [211]. This has the added advantage of needing only a relatively small unit cell. A lower concentration of 0.6 at.% B has also been investigated; however no noticeable difference is found between the band structures. The band structure at this concentration is given in the appendix B.

8.4.2.2 Substitutional α site

The band structure of a substitutional boron atom on an α site is shown in figure 8.9, together with the band structure of AB graphite. The two band structures are broadly similar; however, many important differences can be observed, especially near the Fermi level of AB graphite.

The Fermi level, represented by the green line for the boron-doped model, is lowered as expected. According to the calculations, the difference in the Fermi level between 1.5 at.% B-doped graphite and AB graphite is about 0.56 eV.

As already explained in chapter 3, these plots are Kohn-Sham band structures (i.e. Kohn-Sham energies). DFT gives the ground-state energy only, and not energies of excited states. These band structures are not the true bands, and the two may differ. In our calculations, the band gap is the difference between the eigenvalues of the lowest unoccupied orbital (conduction band) and the highest occupied orbital (valence band); the difference with a real band gap may arise from the discontinuity of the functional derivative of the exchange and correlation energy in LDA, even after theoretical correction [237]. This could affect the Fermi-level value as well, since this is determined from the highest valence band and the lowest conduction band. It should also be noted that higher eigenstates are not involved in the calculation of ground state properties, and it is likely that the shift of the non-bonding band in figure 8.9 will be estimated very poorly.

At the Γ-point, the lowest partially-occupied band (marked with $*$) for the π-orbitals is significantly higher in energy when boron is present as an impurity, than for the corresponding bond in pure graphite, and is decoupled from the other bands. The boron atom splits α–β degeneracy and the interlayer degeneracy.

At the M-point, the same band crosses the Fermi level, but it remains decoupled

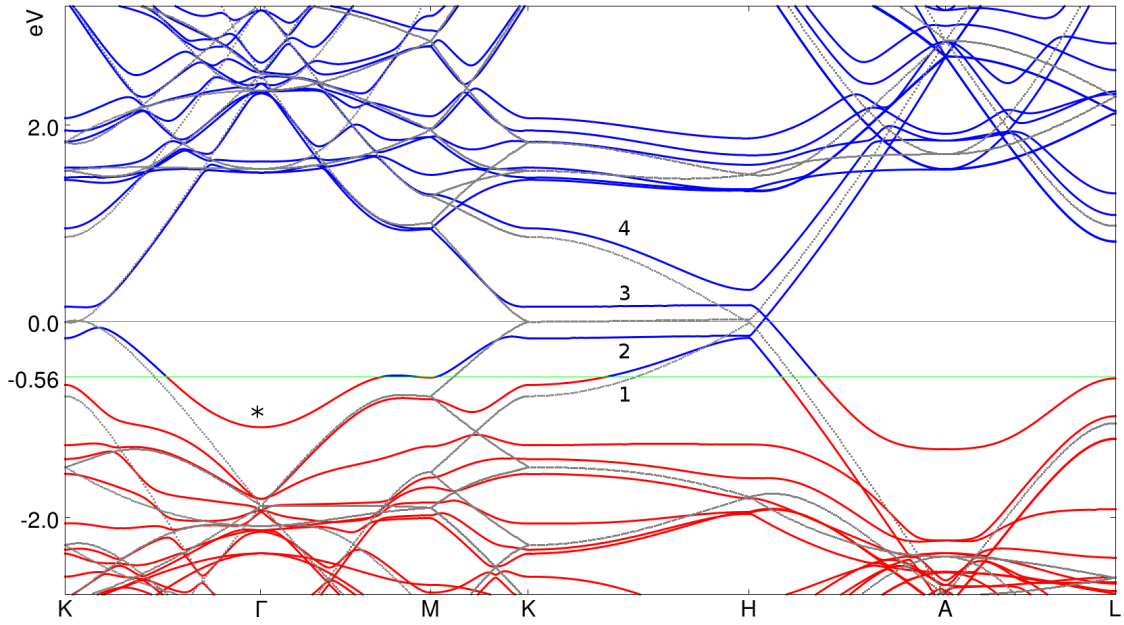

Figure 8.9: Band structure of a 64-atom graphite supercell containing one substitutional boron atom on an α site, and two graphene sheets with AB stacking, optimised by the AIMPRO program package, overlayed on the band structure of pure graphite. The occupied bands are represented in red, the unoccupied bands in dark blue for the boron-doped model and the Fermi level in green, while grey lines are used for the pure graphite supercell.

from all the other π-bands. Between the Γ- and M-point, most of the bonding and anti-bonding bands are very similar between the B-doped graphite and AB graphite. Many changes appear between the M- and the K-points, especially in the bonding region. In AB graphite, symmetry requires degeneracies and at certain k-points, some bands merge, cross and split around these points, whereas, in B-doped graphite, symmetry is broken and these bands do not cross (as shown in figure 8.9 with bands labelled 2 and 3).

It can be seen in figure 8.9 that the two lowest partially-occupied bands are split between K- and H, while in pure, hexagonal graphite, the corresponding bands are nearly degenerate. This splitting is found to be about 0.4 eV, according to the AIMPRO method. The next nearest bonding and anti-bonding bands do not exhibit this behaviour.

Between the K- and H-point, the non-bonding bands remain flat and only cross later in the path. When compared with the two non-bonding bands in AB graphite, we can see that one band shifts to a lower level, while the other band shifts to a higher

level. The gap between the upper shift is similar to the gap of the lower shift. The next nearest bonding and anti-bonding bands follow different paths compared with the corresponding band in AB graphite.

At the *K*-point, the next nearest bonding and anti-bonding α bands, cross in AB graphite; however, in B-doped graphite, a gap of about 0.5 eV opens.

The layer which contains a boron atom has a lower average nuclear potential and a negative charge. Thus α and β states at the *K*-point are raised in energy and split. The other layer is positively charged and lowered in energy, with no α–β splitting.

8.4.2.3 Substitutional β site

When a substitutional boron atom occupies a β site instead of α, as described previously, then the band structure is calculated to be as shown in figure 8.10. Once again, the two band structures are broadly similar; however, many significant differences can be observed near the Fermi level of pure, hexagonal graphite.

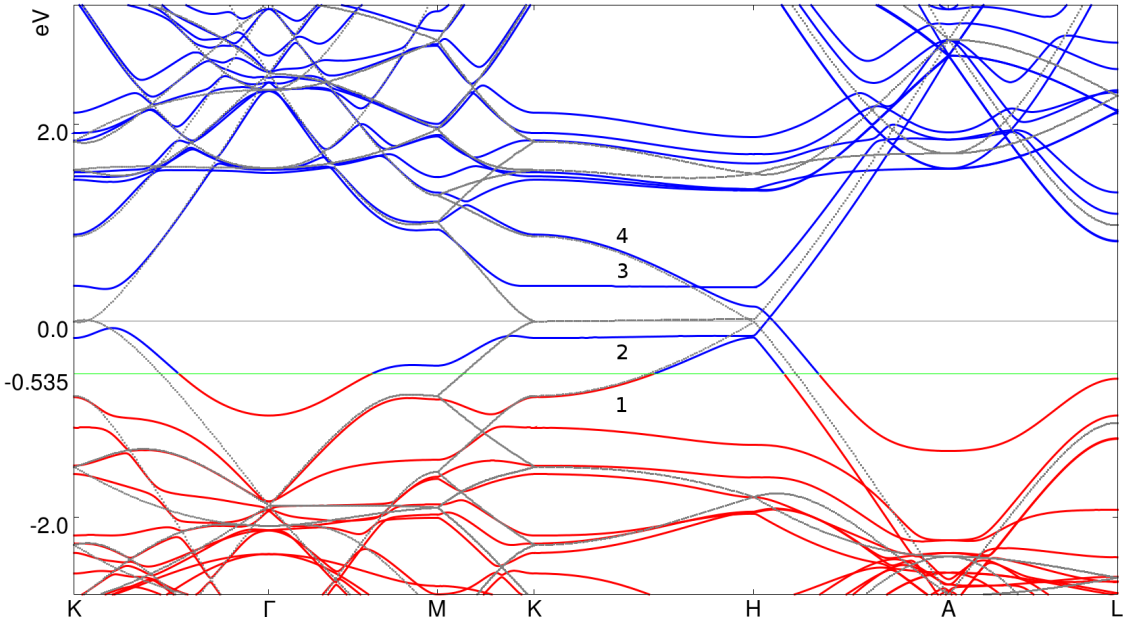

Figure 8.10: Band structure of a 64-atom graphite supercell containing, one substitutional boron atom on a β site, and two graphene sheets with AB stacking, optimised by the AIMPRO program package. The occupied bands are represented in red, the unoccupied bands in dark blue, and the Fermi level in green.

Similar interpretations of the bands' shape can be drawn for a β site and an α site. Nevertheless, they do differ in some particular respects. The lowest partially-occupied

band has slightly higher energy at Γ. In addition, the highest non-bonding band (labelled 3), from the β sublattice, crosses with the anti-bonding band (labelled 4) from the α sublattice.

As before, the lower nuclear potential of a boron atom pushes up the energy of the β band from the boron layer (3), while the α band from this layer is not much affected. This gives a crossing of the two along *K*–*H*. The α and β bands from the unboronated layer are unsplit and are lowered by positive charge.

8.4.2.4 Remarks

Regardless of whether boron occupies an α or β substitutional site, the calculated band structures show several differences with the calculated band structure for AB graphite. The Fermi level is lowered as expected. Nevertheless, it is difficult to compare the present results with experimental works, for the reasons explained earlier. Another factor hindering comparison with experiment is that the concentration of boron in the models (1.5 at.%) is larger than in the specimens used for measurements (< 0.1 at.%) [238]. Calculations with a concentration of boron less than 0.1 at.% requires a very large cell and this was not inverstigated here. The changes in the energy bands are not fully understood; however it seems that the smaller nuclear potential of a boron atom might be responsible for some of the changes. This problem is examined further, using linear perturbation theory, in subsection 8.4.2.8.

8.4.2.5 Substitutional α versus β

In order highlight differences between boron at α and β sites on the band structure, figure 8.11 shows both plotted on the same graph. The two Fermi levels can be considered as being equal within the accuracy of the calculation. Although broadly similar in overall form, many differences between the two sites for boron can be seen, with most of them appearing between the *K*-point and the *H*-point. In this region, the three main observations are as follows:

- The upper non-bonding β band is slightly higher in energy than the upper non-bonding α band, whereas the lower non-bonding α and β bands have the

same energy.

- When a boron atom occupies an α site, the bands close to the non-bonding bands, representing the bonding and anti-bonding orbitals of an α sublattice, are slightly shifted to higher energies between K and H, compared with a boron atom on a β site.

- At the H-point, the changes between the two plots vanish, then the two bands remain nearly identical up to the L-point. At the H-point, there is no interlayer interaction and all that remains is the in-layer splitting which is identical for α and β cases.

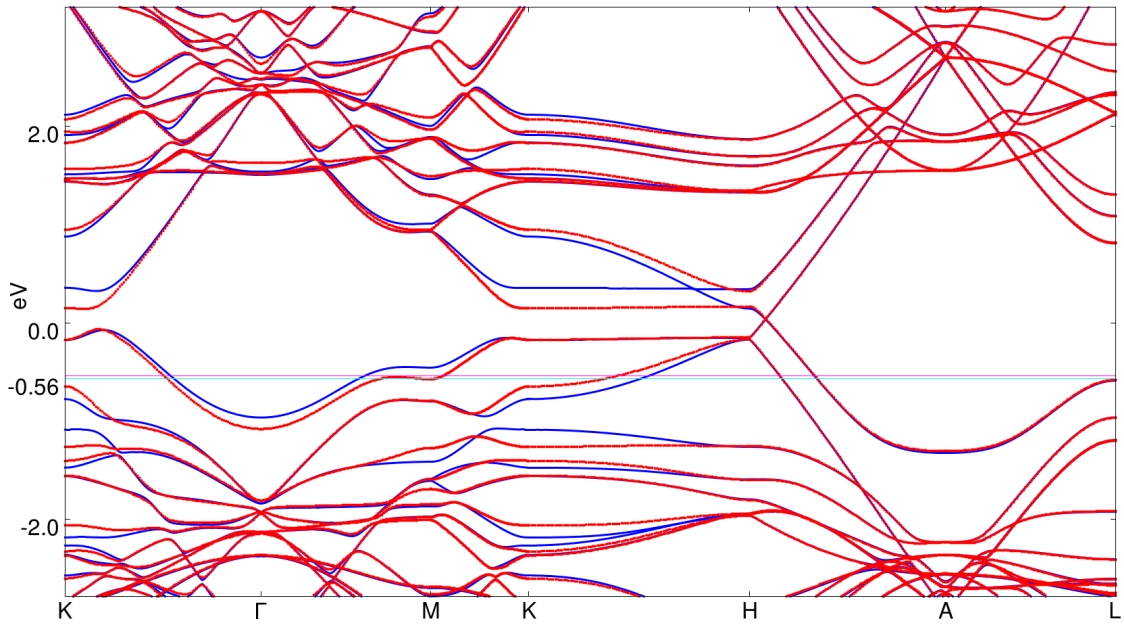

Figure 8.11: Comparison of the two band structures described in section 8.4.2.2 and section 8.4.2.3. Solid red lines represent the band structure when boron occupies an α site, while blue lines represent the β site band structures.

The coincidence of the bands near the H-point shows that the effect of the boron nuclear potential on one sublattice is the same, irrespective of whether a substitutional boron atom occupies an α or β location.

8.4.2.6 The effect increasing substitutional boron concentration

The band structures of the models described in table 8.2 with 3 at.% B, are examined next. The aim is to find the extent to which increasing the concentration of substitutional boron atoms in graphite affects the energy bands. For the sake of

brevity, only the effects observed between the *K*- and *H*-point, are discussed in this section for two cases: boron atoms in the same sheet, and in two neighbouring sheets. The band structures of the remaining models of table 8.2 are shown in appendix B. Finally, the two concentrations 1.5 and 3 at.% B are compared.

First, we consider two of the four models of two boron atoms placed in the same sheet, namely the $\alpha\alpha$ and $\beta\beta$ combinations. Their calculated band structures are shown in figure 8.12.

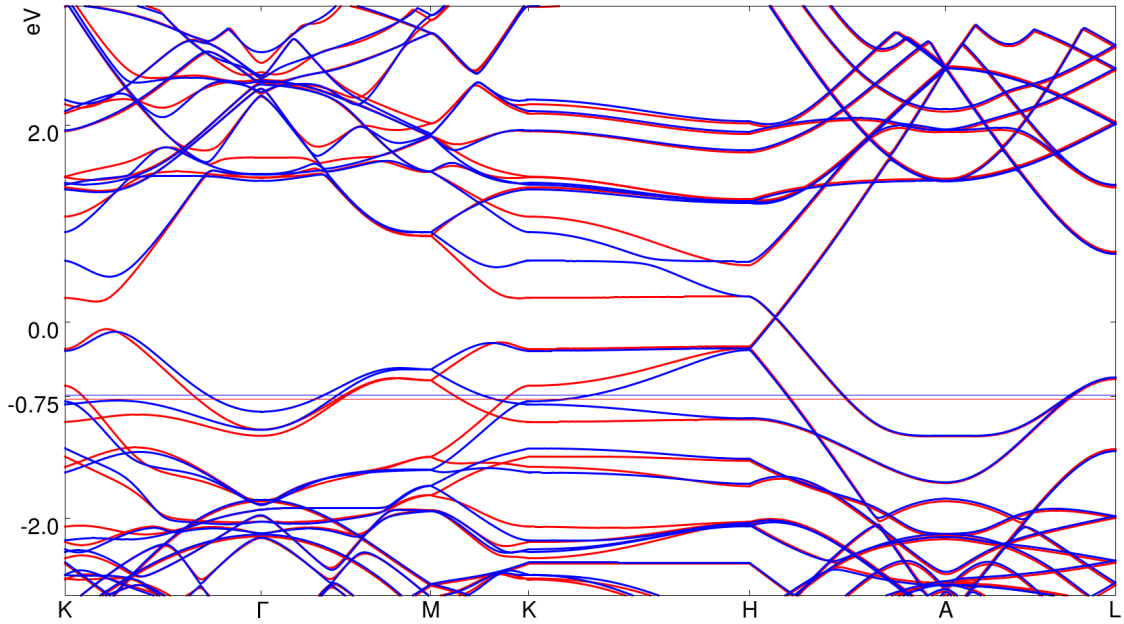

Figure 8.12: Band structures of a 64-atom graphite supercells containing two substitutional boron atoms in the same sheet. The band structure of two boron atoms both on α sites is represented in blue. The band structure of two boron atoms both on β sites is represented in red. The Fermi level is now at -0.75eV.

Similar outcomes are found for two boron atoms on $\beta\beta$ sites versus $\alpha\alpha$ sites, as seen previously for isolated boron atoms on either a β or an α site (figure 8.11), with one crucial difference: the gaps beween bands are approximately doubled. For example, the calculated band gap between the two non-bonding bands is about 0.5 eV at 1.5 at.% B, compared with about 0.95 eV at 3 at.% B.

Next, we examine what happens when two boron atoms are placed in two neighbouring sheets. On this occasion, the band structures for $\alpha\alpha$ and $\alpha\beta$ pairs are chosen. There are two possibilities for $\alpha\alpha$; we chose the α position to be away from each other. The results are shown in figure 8.13.

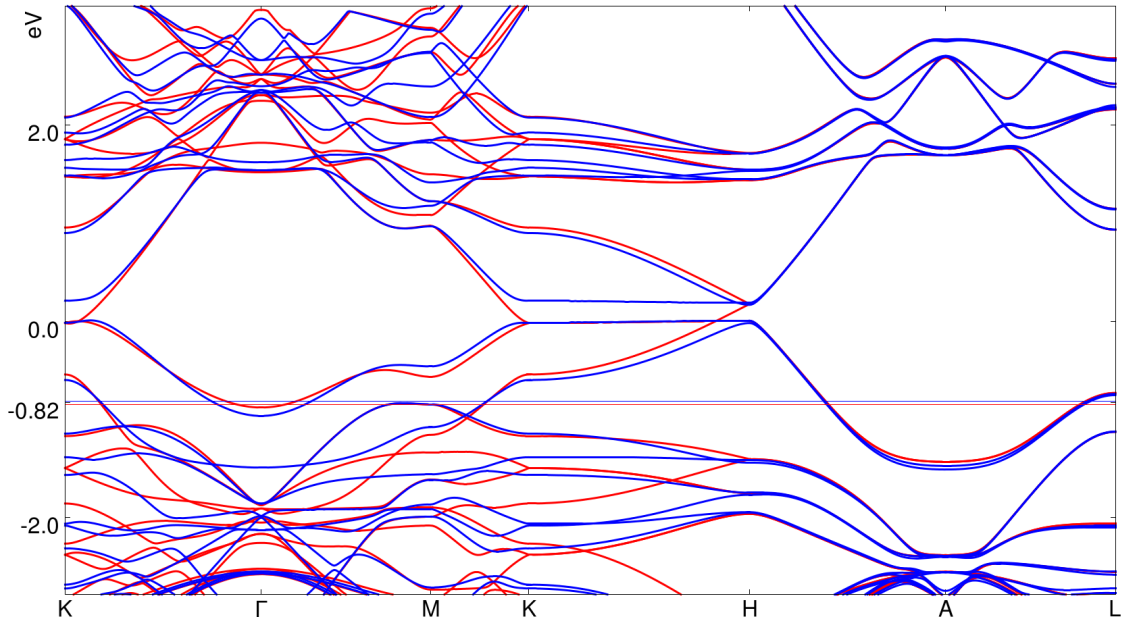

Figure 8.13: Band structures of 64-atom graphite supercells containing two substitutional boron atoms in different sheets. The cross-layer $\alpha\alpha$ pair is represented in red, while the $\alpha\beta$ pair is represented in blue.

In common with all the band structures described previously, differences are between the two cases occur mainly between K and H; however, they take a different form from before. Specifically, unique to the $\alpha\alpha$ pairing, the two lowest unoccupied bands are degenerate between K and H, which is the same as in pure hexagonal graphite. This contrasts with the $\alpha\beta$ cross-layer pairing, where there is a gap between the bands of about 0.2 eV, or about half the size of the corresponding gap for a single substitutional atom. Thus, this case is, at least as far as LDA calculations go, a narrow gap semiconductor.

8.4.2.7 Note

The band structures for many different models have been calculated to understand the effect of boron as an impurity. In these models, various concentrations were investigated as well as the effect of the α and β site. It is difficult to draw many conclusions from these bands but it appears that the higher the concentration of boron, the lower the Fermi level, as expected. Perturbation theory is used in the next section to interpret the possible effect of boron atom on the energy bands.

8.4.2.8 Linear perturbation theory (LPT)

The general use of this theory is to simplify a complicated quantum system. LPT is often applied in order to determine a solution to the Schrödinger equation for complicated Hamiltonians by using the Hamiltonians where the exact solution is known (e.g. hydrogen). Then from the known solution, the perturbation is added to the system. If there are not many changes (e.g. energy levels and eigenstates), it can be considered that the perturbation is defined as corrections to the initial model. In our case, we use LPT to explain the changes in the band structures. The energy bands for graphite are known and have been described previously. When one or two carbon atoms are substituted with boron atoms, the band structures look very similar apart from some minor shifts. We focus on the graphene wave-functions at the K-point which reside on either the α or β sublattices.

If the wave-functions are considered to be unchanged, then four wave-functions are to be considered on the two layers of the supercell (1 and 2): $\psi_{K_{\alpha_1}}$, $\psi_{K_{\beta_1}}$, $\psi_{K_{\alpha_2}}$ and $\psi_{K_{\beta_2}}$. If it is assumed that the change in potential is uniform throughout the layer, then the following expression can be written:

$$\begin{aligned}\Delta E &= \int \psi^*_{K_{\alpha_1}} \Delta V_B \psi_{K_{\alpha_1}} d\tau = \Delta V_B \int \psi^*_{K_{\alpha_1}} \psi_{K_{\alpha_1}} d\tau \\ &= \int \psi^*_{K_{\beta_1}} \Delta V_B \psi_{K_{\beta_1}} d\tau = \Delta V_B \int \psi^*_{K_{\beta_1}} \psi_{K_{\beta_1}} d\tau,\end{aligned}$$

and for normalised wavefunctions, it equals the change in potentials. ΔE is the difference in energy between two bands. This most likely due to charge transfer between layers. Now if we consider the non-uniform effect of boron, largely due to the weaker nuclear potential, we can write the following expressions for boron on an α site:

$$\begin{aligned}\Delta E_{\alpha\alpha} &= \int \psi^*_{K_{\alpha_1}} \Delta V_{B_\alpha} \psi_{K_{\alpha_1}} d\tau \\ \Delta E_{\alpha\beta} &= \int \psi^*_{K_{\beta_1}} \Delta V_{B_\alpha} \psi_{K_{\beta_1}} d\tau\end{aligned}$$

and for boron on a β site:

$$\Delta E_{\beta\alpha} = \int \psi^*_{K_{\alpha_1}} \Delta V_{B_\beta} \psi_{K_{\alpha_1}} d\tau$$
$$\Delta E_{\beta\beta} = \int \psi^*_{K_{\beta_1}} \Delta V_{B_\beta} \psi_{K_{\beta_1}} d\tau$$

The notation ΔV_{B_i} is the boron potential where i represents the boron site. The shift in energy, ΔE_{ij}, between graphite and boron doped graphite, where j labels the sublattice where the band resides, can be measured from the difference between the bands as illustrated in figure 8.14.

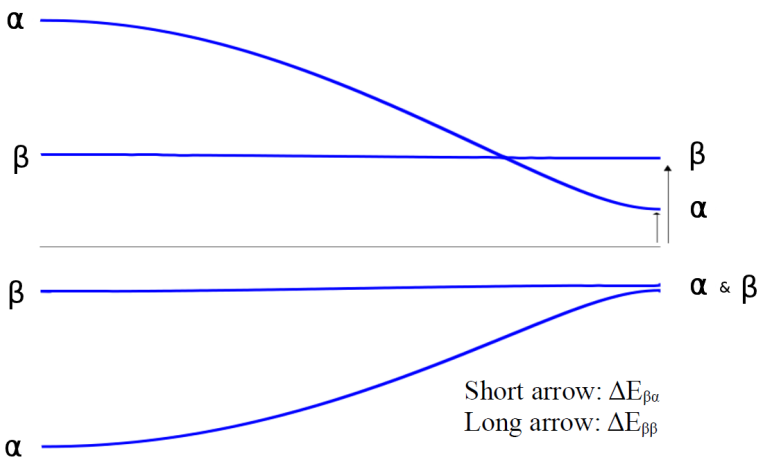

Figure 8.14: Enlarged view between the K- and the H-point of the band structure from figure 8.10. The short and long arrow represent the shift in energy, for the α and β sublattices when boron is on a β site, compared to normal graphite (black line).

If we compare the ΔE_{ij} of the two band structures plotted in figure 8.11 at the K-point, we observe that for a boron atom on an α and a β sites we have:

$$\Delta E_{\alpha\alpha} > \Delta E_{\alpha\beta}$$
$$\Delta E_{\beta\alpha} > \Delta E_{\beta\beta}$$

and if we compare the shift for α versus β, we have:

$$\Delta E_{\alpha\alpha} > \Delta E_{\beta\alpha}$$
$$\Delta E_{\beta\beta} > \Delta E_{\alpha\beta}$$

These changes in energy can also be written for the H-point. In this case we have:

$$\Delta E_{\alpha\alpha} > \Delta E_{\alpha\beta}$$

$$\Delta E_{\beta\beta} > \Delta E_{\beta\alpha}$$

and for α versus β, we have:

$$\Delta E_{\alpha\alpha} = \Delta E_{\beta\beta}$$

$$\Delta E_{\alpha\beta} = \Delta E_{\beta\alpha}$$

These observations, both for the K- and H-point can be made for boron at different concentrations; the same equations are found. These results indicate that the weaker nuclear potential of boron is the prime reason for the splitting of bands from the same layers when boron atoms are present as substitutional atoms, and charge transfer for the splitting of bands in different layers.

In order to confirm the origin of these shifts, the offset calculation option in AIMPRO is invoked. The offset analysis option calculates potentials along one dimension, averaged over the other two dimensions. In our case it is the c-direction. Figure 8.15 illustrates offset calculations for structures with and without substitutional atoms. Image 2 shows the graph for a pure graphite structure. The potentials of each layer are the same. However, in image 3, the graph represents the potentials when a substitutional boron atom is present in layer A. It can be observed that the potential in layer B is lower than the potential in layer A by 0.67 eV. This indicates that the nuclear potential of a boron atom is lower than a carbon atom. Image 4, shows the graph for the potentials when two substitutional boron atoms are present in layer A. The difference in potentials between the two layers is even larger in this case and ΔE=1.34 eV.

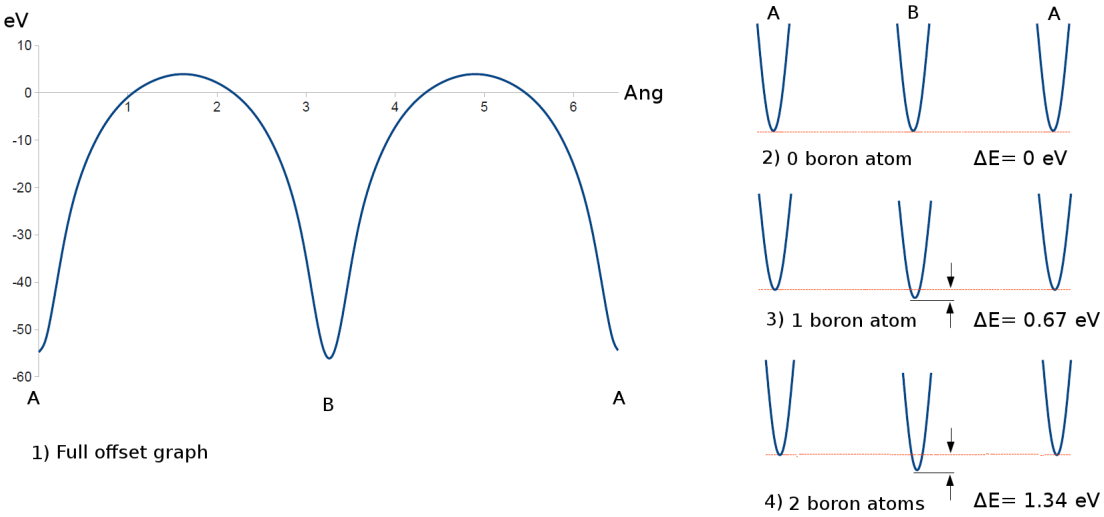

Figure 8.15: 'Offset' calculation of graphite with and without substitutional boron atoms. 1) Graph representing the full path of an offset calculation, with x-axis representing the c lattice vector of graphite in angstrom and with the y-axis representing the potential in eV; 2) Enlarged view of an offset calculation graph for pure graphite; 3) Enlarged view of an offset calculation graph for graphite with one substitutional boron atom; 4) Enlarged view an of offset calculation graph for graphite with two substitutional boron atoms in the same layer. The red dotted line represents the highest potential of the structures. A and B indicates the layers

8.5 Calculation on substitutional boron atom in turbostratic graphite

In this section, one of the aims is to understand how boron as a substitutional impurity can promote the graphitisation process. Another aim is to describe the increase in the shear constant C_{44} with substitutional boron. Turbostratic structures in graphite have been discussed in a previous chapter and more information about their formation and properties has been given, and only the effect of boron on these structures is investigated here.

8.5.1 The effect of boron in graphitisation

The unit cells used in the following calculations contain either 28, 52 or 82 atoms hexagonal unit cells with relative rotational angles of 38.2°, 27.8° and 21.8° respectively. This means that for these two models, the concentration of boron atom is either 3.5, 1.9 or 1.2 at.%. In the following work, the Brillouin zone was sampled using the Monkhorst and Pack scheme with a sampling of 5×5×2. The basis sets

pdpp and pdpp are used for carbon and boron atoms respectively. The states are occupied according to the first-order Methfessel-Paxton scheme with $kT = 0.01$ eV. In order to understand the effect of boron during graphitisation, the binding energy of boron to twist boundaries, $\Delta E_{B_{binding}}$, is calculated. To determine $\Delta E_{B_{binding}}$, equation 8.1 is used.

$$\Delta E_{B_{binding}} = -[(\Delta H_{subt})_{twist} - (\Delta H_{subt})_{AB}] \tag{8.1}$$

with $(\Delta H_{subt})_{twist}$ and $(\Delta H_{subt})_{AB}$ equal to:

$$(\Delta H_{subt})_{twist} = E_{B_{twist}} - E_{twist}$$
$$(\Delta H_{subt})_{AB} = E_{B_{graph}} - E_{graph}$$

The definition of these notations is summarised in table 8.3.

Notation	Description
$\Delta E_{B_{binding}}$	Boron binding energy to twist boundaries
$(\Delta H_{subt})_{twist}$	Heat of formation of boron at twist boundaries
$(\Delta H_{subt})_{AB}$	Heat of formation of boron at AB graphite
$E_{B_{twist}}$ and E_{twist}	Calculated energy with or without boron in twist boundaries
$E_{B_{graph}}$ and E_{graph}	Calculated energy with or without boron in AB graphite

Table 8.3: Description of the notations used in equation 8.1.

The calculated energies are shown in table 8.4. Given that both boron doping and radiation damage restore the lattice value of C_{44}, and that boron might be doing this by an electronic interaction without cross-linking bonds, we repeated the calculations with vacancies. The calculated energies are also shown in table 8.4

Defect	Concentration	$\Delta E_{B_{binding}}$ (eV)
Boron	1.2 at.%	-0.235
	1.9 at.%	-0.233
	3.5 at.%	-0.313
Vacancy	1.2 at.%	-0.237
	1.9 at.%	-0.189
	3.5 at.%	-0.481

Table 8.4: Calculated binding energy for boron and monovacancy to twist boundaries using equation 8.1

It is interesting to see that binding energies are very similar for many systems

at different concentrations. The negative binding energies at all the concentrations studied shows that boron atoms should be repulsive to twist boundaries. In other words, when boron is present during the turbostratic stage of the graphitisation, the boron destabilises the turbostratic layers. This means that one of the role of boron in graphitisation is the aid the removal of twist boundaries to arrive to the final AB stacking. Although vacancies would be unlikely at these very high temperatures, it is interesting to see that they have a similar effect that boron on twist boundaries.

8.5.2 The effect of boron on C_{44}

The unit cells used in the following calculations contain 28 atoms hexagonal unit cells with a relative rotational angles of 38.2°. This means that for these models, the concentration of boron atom is about 3.5 at.%. In the following work, the Brillouin zone was sampled using the Monkhorst and Pack scheme with a sampling of 7×7×2. The basis sets pdpp and pdpp are used for carbon and boron atoms respectively. The states are occupied according to the first-order Methfessel-Paxton scheme with kT = 0.01 eV. The increase in C_{44} with doped boron in graphite is believed to be related, in the same that radiation damage, to interstitial atoms pinning two neighbouring layers together [203]. The present calculations suggest another possibility:

- Small angle twist boundaries can be described as hexagonal networks of basal screw dislocations.
- Basal screw dislocations move with zero Peierls stress
- This gives a flat energy landscape for basal slip.
- If boron interacts with dislocations this landscape is no longer flat and pinning occurs.
- The same behaviour is happening for vacancies.

Thus we performed gamma surfaces calculations, along the x-axis and the y-axis, for one twist boundaries with a relative rotational angle of 38.2°. The results are shown in figure 8.16. The first important feature arises from the straight line shown by the blue curve, representing pure graphite in both x and y directions. Our calculations

show that the gamma surface is flat in [002] twist boundaries in pure graphite and this is in good agreement with earlier work [209]. We can thus expect a very low C_{44} value for [002] twist boundaries in pure graphite. Another feature arises from the red curves in the two graphs, representing substitutional boron atom. We can see that the curves are not flat and small undulations are observed. The difference between the highest and lowest binding energy is about 3.36 meV and 2.89 meV in the x and y directions respectively. This phenomenon is even more important for vacancies, as shown by the yellow curves. The difference between the highest and lowest binding energy is about 4.82 meV and 5.35 meV in the x and y directions respectively.

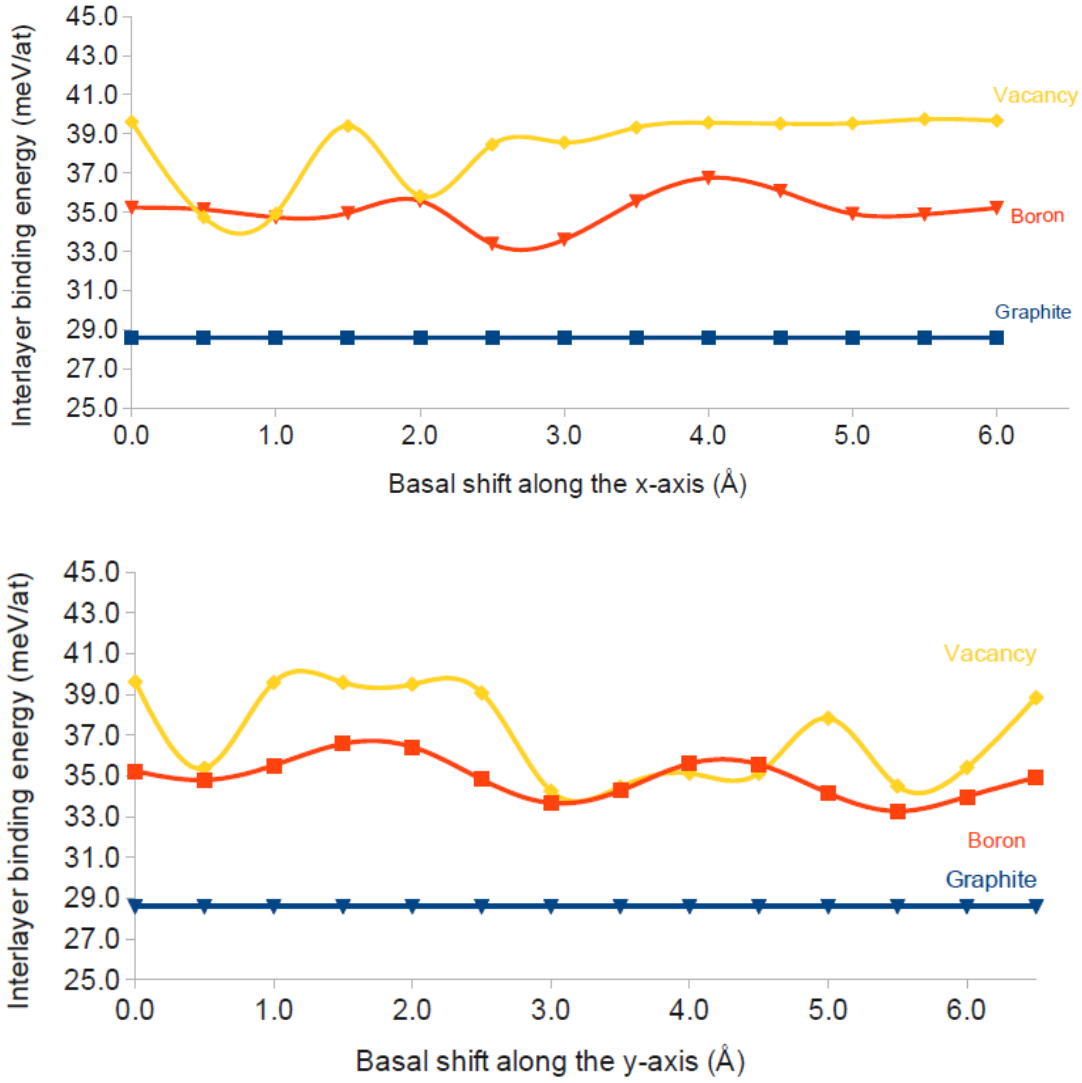

Figure 8.16: Gamma surface calculations for turbostratic graphite (blue), turbostratic graphite with one substitutional boron atom (red) and turbostratic graphite with a monovacancy (yellow) along: top) the x-axis, bottom) the y-axis.

There is a clear evidence for undulations in the energy landscape for substitutional boron and vacancy. The gamma surfaces are not flat and thus C_{44} values are expected to increase. This means that the pinning of basal dislocations via substitutional boron atoms and via vacancies could be the reason for the increase in C_{44}. The results demonstrate a substantial advance in understanding shear modulus changes, without them, it is difficult to square a rationale for pinning by radiation induced defects through interplanar cross-links, with a similar effect arising from a substitutional atom like boron, which does not appear to chemically bond between layers. It would appear that both interstitials and vacancies contribute to basal dislocation pinning.

8.6 Conclusion

This chapter reviews the impurity boron in graphite by investigating its doping effect through the band structure and its role during the process of graphitisation. Information on the different catalytic roles played by boron during graphitisation has been well observed. It has been suggested that its catalytic effect arises from its ability to become a substitutional impurity, and to fill carbon vacancy sites. Our calculations show another possible catalytic effect; substitutional boron can destabilise twist boundaries and help their removal. Another interesting feature described in the literature is the boron effect on the shear constant C_{44}. It has been suggested that the increase of the C_{44} value comes from the interstitial boron atoms which hinder the layers to shear. Our calculations suggest that the increase in C_{44} can come from the pinning of basal dislocations via substitutional boron atoms. Similarly, radiation damage could also pin via vacancies.

Chapter 9

Conclusion

Conclusions and remarks have been drawn at the end of each chapter. A summary of these points is given here, together with some general conclusions.

In the introduction, graphite is described as a unique material with many properties, which give it an important role for industrial purposes. Its single crystal structure was established almost a century ago, and since then, it has been a central topic for research. In more recent times, research into carbon has lead to the discovery of new forms.

Over the years, the process of synthesising graphite has been developed by many manufacturers. Experimental work has shown that certain materials have the ability to graphitise while others cannot. For many precursors, experiments have established that impurities are responsible for non-graphitising carbons; however, some questions remain about their behaviour. In this thesis, I have begun by giving a broad review of some of the chemistry involved in the graphitisation process with some of the techniques available to measure the evolution of carbon materials with heat treatment. I have then used current first principle techniques to review the evolution of turbostratic graphite into AB graphite, as well as to find new possible roles of two impurities; sulphur and boron, during the late stage of the graphitisation process. Heat of formation for these impurities in pure and defected graphitic materials, have been calculated to investigate their preferential sites and determine their roles.

For turbostratic graphite, we have investigated the changes in the interlayer spacing,

d_{002} between a 2D structure and a 3D structure. Our calculations are in good agreement for the interlayer spacing of pure turbostratic graphite, with the value described in the literature. Then, the two intermediate interlayer spacings described by Franklin have been calculated using AIMPRO. Despite the fact that LDA always underestimates interlayer separation, our calculations are in congruence with experimental studies (± 1%). It is believed to be the first time such computational calculations have been performed.

For the impurity sulphur, the literature suggests that a sulphur atom cross-links between layers of graphite. The calculations appear to be incompatible with the idea that sulphur forms defect complexes cross-linking layers in well-graphitised carbon. However, calculations have shown that more favourable sites for sulphur in graphite are at the edges. Some authors in the literature have described thiophenic-like molecules as molecules which can promote the process of graphitisation. The calculations also suggest that sulphur can easily react with zigzag and armchair edges which could also ease the graphitisation process. Furthermore, new roles for sulphur were also proposed. Calculations have shown that sulphur atoms have the ability to open folds with a small activation energy. The second role is, once a fold is open via sulphur, prismatic dislocations with a Burgers vector equal to c, may be moved more easily when sulphur is attached to their edge, in order to give a more stable structure with two partial dislocations.

For boron, experimental works have described the catalytic effect that this impurity can have on the formation of layers. We reviewed the preferential sites for boron within the graphite lattice as well as its effect on the graphite electronic band structures. The results indicate that the weaker nuclear potential of boron is the prime reason for the splitting of bands from the same layers when boron atoms are present as substitutional atoms, and charge transfer for the splitting of bands in different layers. Our calculations also described a new role for substitutional boron: it can make twist boundaries even less stable, which can help with their removal. The effect of substitutional boron on the shear constant C_{44} was also studied. It appears that the increase in C_{44} comes from the pinning of basal dislocations via substitutional boron atoms, and the same phenomenon is observed with vacancies.

As a final remark, DFT is a powerful tool which can help to better understand the graphitisation process. The work presented in this thesis has concentrated on the late stages of graphitisation. It was shown that two impurities, which are not released early in the process, can promote the graphitisation process. However, some questions remain to be answered regarding the role of sulphur on prismatic dislocations and this work is ongoing. DFT can also help understanding grain boundaries, as well as dislocations and defects in poly-crystal graphite. Calculations on the previous stages can also be considered but the increase of disordering makes it a difficult task.

Appendix A

Graphite's first Brillouin zone

The reciprocal lattice (full lines) and the first Brillouin zone (dashed lines) of the graphite hexagonal lattice is illustrated in figure A.1.

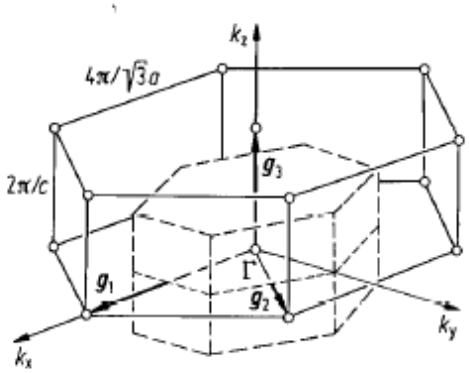

Figure A.1: Schematic representation of the reciprocal space and the first Brillouin zone in a hexagonal lattice.

The reciprocal basis vectors g_j (j=1,2 and 3). k_x, k_y and k_z indicate the Cartesian coordinate system in reciprocal space parallel to x, y and z in real space. The g_j vectors can be determined with by the following coordinates:

$$\vec{g}_1 = \left(\frac{4\pi}{\sqrt{3}a}, 0, 0\right)$$
$$\vec{g}_2 = \left(\frac{2\pi}{\sqrt{3}a}, \frac{2\pi}{a}, 0\right)$$
$$\vec{g}_3 = \left(0, 0, \frac{2\pi}{c}\right)$$

The first Brillouin zone is illustrated in more details in figure A.2

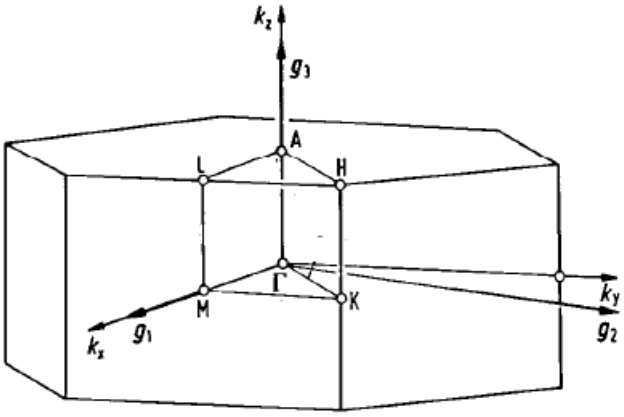

Figure A.2: Schematic representation of the points describing the first Brillouin zone.

Each point inside the Brillouin zone have the following coordinates with respect to the vectors g_j:

$$\begin{aligned}
\Gamma = &\quad (0,0,0) \\
M = &\quad \left(\frac{1}{2},0,0\right) \\
K = &\quad \left(\frac{1}{3},\frac{1}{3},0\right) \\
A = &\quad \left(0,0,\frac{1}{2}\right) \\
L = &\quad \left(\frac{1}{2},0,\frac{1}{2}\right) \\
H = &\quad \left(\frac{1}{3},\frac{1}{3},\frac{1}{2}\right)
\end{aligned}$$

Appendix B

Band structures of graphite with substitutional boron atoms

The band structure of a substitutional boron atom is illustrated in figure B.1. The concentration is 1.5 at.% B.

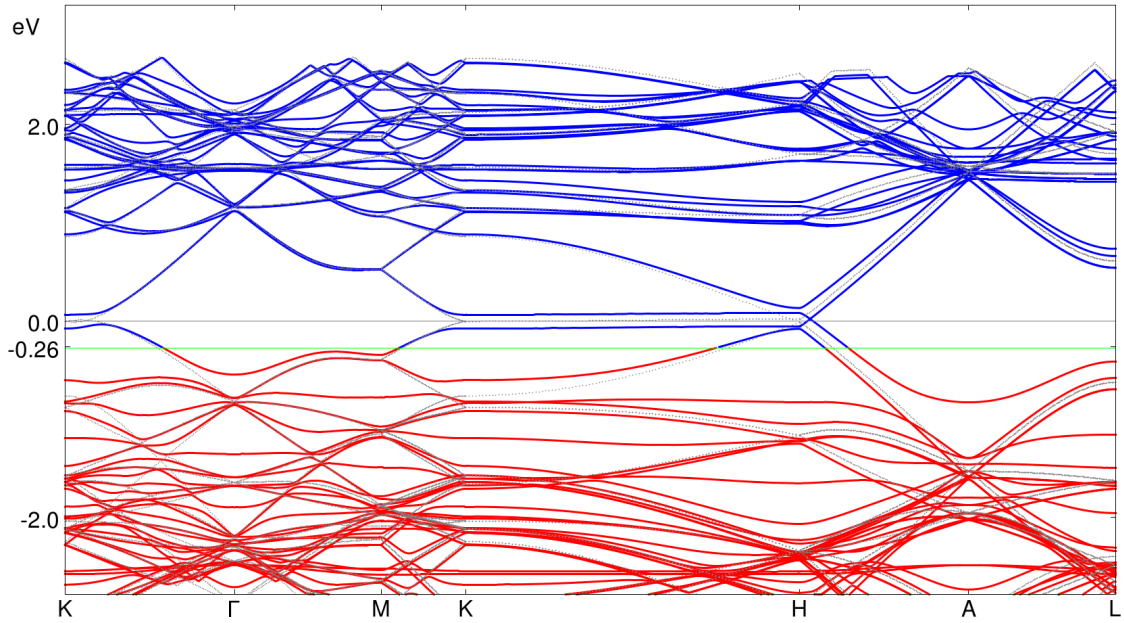

Figure B.1: Band structure of a 196-atom graphite supercell containing one substitutional boron atom on an α site, and two graphene sheets with AB stacking, optimised by the AIMPRO program package, overlayed on the band structure of pure graphite. The occupied bands are represented in red, and the unoccupied bands in dark blue for the boron-doped model, while grey lines are used for the pure graphite supercell.

The band structure of two substitutional boron atoms, on an α site and a β site in

the same sheet, is illustrated in figure B.2. The concentration is 3.0 at.% B.

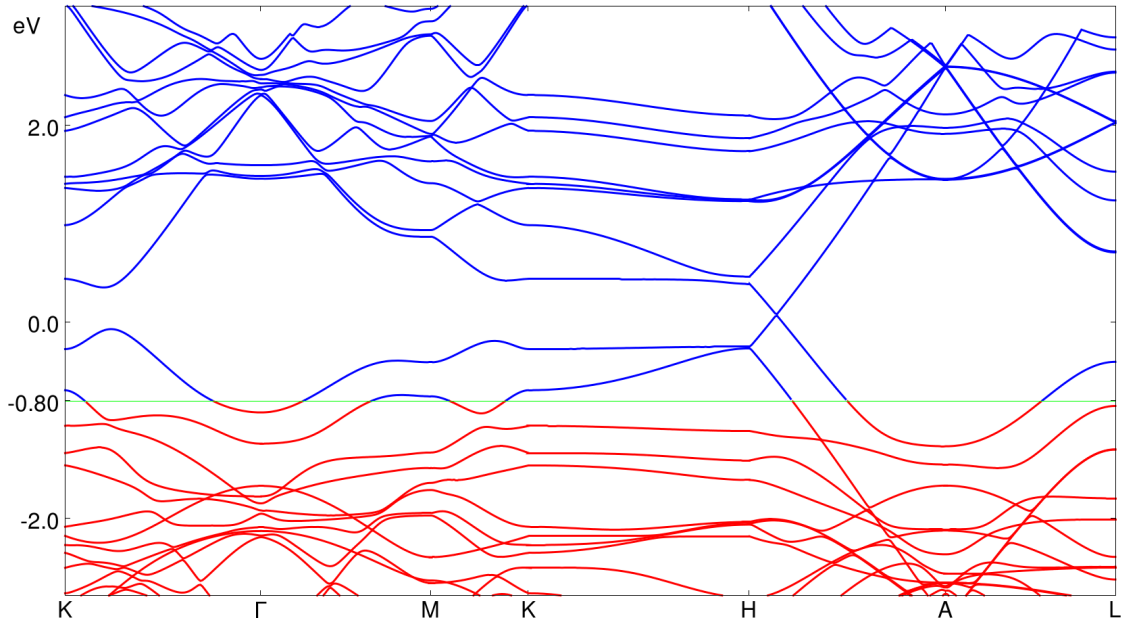

Figure B.2: Band structure of a 64-atom graphite supercell containing two substitutional boron atoms in the same sheet. One boron atom is on an α site and the other on a β site.

The band structure of two substitutional boron atoms, on two neighbouring α and β sites in the same sheet, is illustrated in figure B.3. The concentration is 3.0 at.% B.

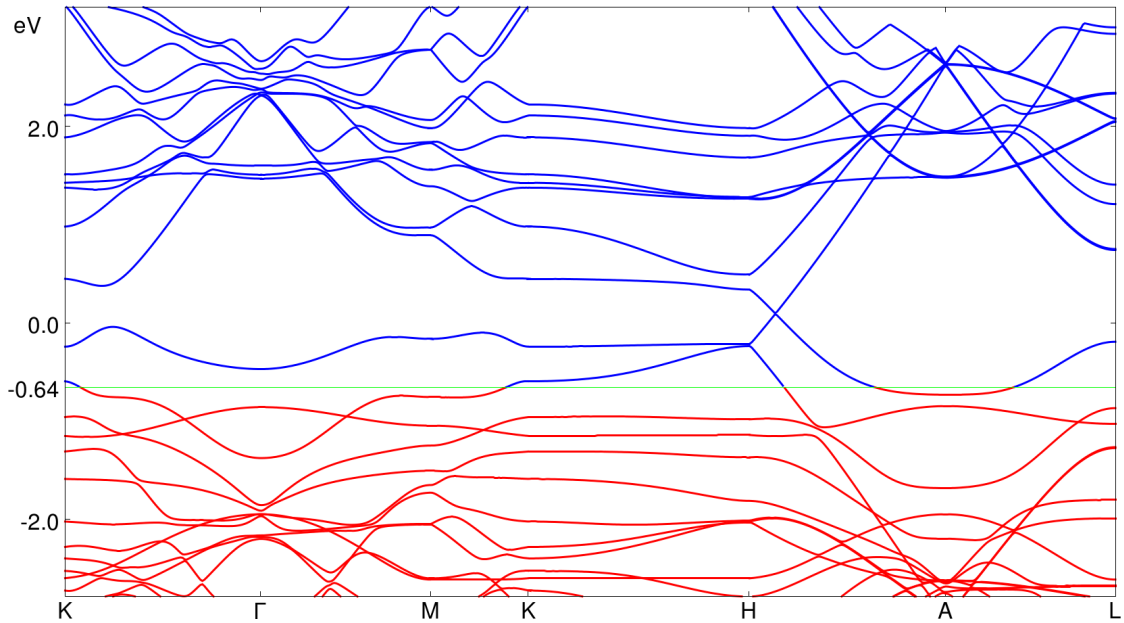

Figure B.3: Band structure of a 64-atom graphite supercell containing two substitutional boron atoms in the same sheet. One boron atom is on an α site and the other on a the neighbouring β site.

The band structure of two substitutional boron atoms, on two β sites and in two neighbouring sheets, is illustrated in figure B.4. The concentration is 3.0 at.% B.

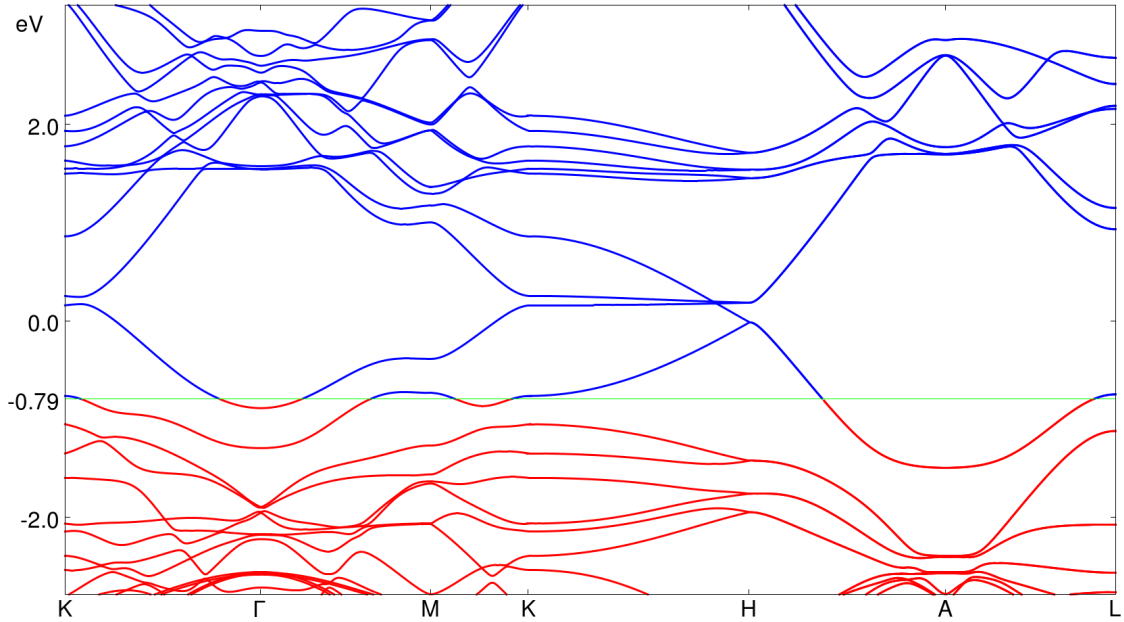

Figure B.4: Band structure of a 64-atom graphite supercell containing two substitutional boron atoms in two different sheets. Both boron atoms are on β sites.

List of Figures

List of Tables

Bibliography

[1] H.W. Kroto, J.R. Heath, S.C. O'Brien, R.F. Curl, and R.E. Smalley. C_{60}: Buckminsterfullerene. *Nature*, 318:162, 1985.

[2] K.S. Novoselov, A.K. Geim, S.V. Morozov, D. Jiang, Y. Zhang, S.V. Dubonos, I.V. Grigorieva, and A.A. Firsov. Electric field effect in atomically thin carbon films. *Science*, 606:666, 2004.

[3] M.E. Wieser. Atomic weights of the elements 2005: Iupac technical report. *Pure and applied chemistry*, 78:2051, 2006.

[4] C.E. Housecroft and E.C. Canstable. *Chemistry, an integrated approach*. Prentice Hall, 1997.

[5] P. Delhaes. *Design and control of structure of advanced Carbon Materials for enhanced performance*. Nato Science Series, Kluwer Academic Publishers, 2001.

[6] A. W. Hull. A new method of x-ray crystal analysis. *Physical Review*, 10:661, 1917.

[7] J.D. Bernal. The structure of graphite. *Proceeding of the royal society A*, 106:749, 1924.

[8] H. Lipson and A.R. Stokes. The structure of graphite. *Proceedings of the Royal Society of London. Series A*, 181:101, 1942.

[9] H.P Boehm and U. Hofmann. Die rhomboedrisched des graphits. *Zeitschrift für anorganische und allgemeine Chemie*, 278:58, 1955.

[10] J. Biscoe and B.E. Warren. An x-ray study of carbon black. *Journal of Applied Physics*, 13:364, 1942.

[11] J.-C. Charlier, T. W. Ebbesen, and P. Lambin. Structural and electronic properties of pentagon-heptagon pair defects in carbon nanotubes. *Physical Review B*, 53:11108, 1996.

[12] M. Irvine. *Nuclear power: A very short introduction*. Oxford, 2011.

[13] H.L. Anderson, E. Fermi, and L. Szilard. Neutron production and absorption in uranium. *Physical Review*, 56:284, 1939.

[14] *Proceeding of the international conference on the peaceful uses of atomic energy*, 1955.

[15] V.F. Sears. Neutron scattering lengths and cross section. *Neutron News*, 3:26, 1992.

[16] A.N. Jones and B.J. Marsden. Nuclear graphite manufacture, microstructure and unirradiated properties. Technical report, Nuclear Graphite Research Group, 2009.

[17] R.M. Brugger. Total neutron cross section of chlorine and carbon. *Physical Review*, 104:1054, 1956.

[18] G.E. Evans. Selection of materials for reactors. *Nucleonics*, 11:18, 1953.

[19] B.T. Kelly. Graphite - the most fascinating nuclear material. *Carbon*, 20:3, 1982.

[20] P.A. Thrower. Interstitial and vacancy loops in graphite irradiated at high temperatures. *British journal of applied physics*, 15:1153, 1964.

[21] W.N. Reynolds and P.A. Thrower. The nucleation of radiation damage in graphite. *Philosophical Magazine*, 12:573, 1965.

[22] A. Oberlin. Carbonization and graphitization. *Carbon*, 22:521, 1984.

[23] A. Asthana, Y. Matsui, M. Yasuda, K. Kimoto, T. Iwatac, and Ken ichi Ohshimaa. Investigations on the structural disordering of neutron-irradiated highly oriented pyrolytic graphite by x-ray diffraction and electron microscopy. *Journal of Applied Crystallography*, 38:361, 2005.

[24] W.T. Eeles. Diffuse diffraction phenomena from neutron-irradiated graphite single crystals. *Acta Crystallographica A*, 24:688, 1968.

[25] A. Oberlin, S. Bonnamy, and K. Oshida. Landmarks for graphitization. *Tanso*, 224:281, 2006.

[26] J. Lachter and R.H. Bragg. Interstitials in graphite and disordered carbons. *Physical review B*, 33:8903, 1986.

[27] J. P. Goss. *A first principle study of defects in semiconductors*. PhD thesis, University of Exeter, 1997.

[28] A. A. El-Barbary. *First principles characterisation of defects in irradiated graphitic materials*. PhD thesis, University of Sussex, 2005.

[29] C. P. Ewels. *Density functional modelling of point defects in semiconductors*. PhD thesis, University of Exeter, 1997.

[30] D. R. Hartree. The wave mechanics of an atom with a non-coulomb central field. part i. theory and methods. *Proceedings of the Cambridge Philosophical Society*, 24:89, 1928.

[31] J. C. Slater. Note on hartree's method. *Physical Review*, 35:210, 1930.

[32] C. Møller and M.S. Plesset. Note on an approximation treatment for many-electron systems. *Physical Review*, 46:618, 1934.

[33] P. Hohenberg and W. Kohn. Inhomogeneous electron gas. *Physical Review*, 136:B864, 1964.

[34] W. Kohn and L. J. Sham. Self-consistent equations including exchange and correlation effects. *Physical Review*, 140:A1133, 1965.

[35] D. M. Ceperley and B. J. Alder. Ground state of the electron gas by a stochastic method. *Physical Review Letters*, 45:566, 1980.

[36] S. J. Vosko, L. Wilk, and M. Nusair. Accurate spin-dependent electron liquid correletion energies for local spin density calculations: A critical analysis. *Canadian Journal of Physics*, 58:1200, 1980.

[37] J. P. Perdew and A. Zunger. Self-interaction correction to density-functional approximations for many electron systems. *Physical Review B*, 23:5048, 1981.

[38] J. P. Perdew and Y. Wang. Accurate and simple analytic representation of the electron gas correlation energy. *Physical Review B*, 45:13244, 1992.

[39] C.D. Latham, M.I. Heggie, M. Alatalo, S. Oberg, and P.R. Briddon. The contribution made by lattice vacancies to the wigner effect in radiation-damaged graphite. *In preparation*, 2012.

[40] J. P. Perdew. Density-functional approximation for the correletion energy of the inhomogeneous electron gas. *Physical Review B*, 33:8822, 1986.

[41] J. P. Perdew. *Electronics structure of solids*. Akademie Verlag, 1991.

[42] C. Lee, W. Yang, and R. G. Parr. Development of the colle-salvetti correlation energy formula into a functional of the electron density. *Physical Review B*, 37:785, 1988.

[43] M. Dion, H. Rydberg, E. Schroder, D.C. Langreth, and B.I. Lundqvist. Van der waals density functional for general geometries. *Physical review letters*, 92:246401, 2004.

[44] D. Sholl and J. A. Steckel. *Density Functional Theory: A Practical Introduction*. John Wiley & Sons, 2011.

[45] H. Hellmann. A new approximation method in the problem of many electrons. *Journal of chemicals physics*, 3:61, 1935.

[46] G. B. Bachelet, D. R. Hamann, and M. Schlüter. Pseudopotentials that work: From H to Pu. *Physical Review B*, 26:4199, 1982.

[47] C. Hartwigsen, S. Goedecker, and J. Hutter. Relativistic separable dual-space gaussian pseudopotentials from H to Rn. *Physical Review B*, 58:3641, 1998.

[48] http://aimpro.ncl.ac.uk/.

[49] P.R. Briddon and R. Jones. LDA calculations using a basis of gaussian orbitals. *Physica Statu Solidi B*, 217:131, 2000.

[50] M. Methfessel and A. T. Paxton. High-precision sampling for brillouin-zone integration in metals. *Physical Review B*, 40:3616, 1989.

[51] Hans Hellmann. *Einführung in die Quantenchemie*. Leipzig, 1937.

[52] R.P. Feynman. Forces in molecules. *Physical Review*, 56:340, 1939.

[53] W.H. Press, B.P Flannery, S.A. Teukolsky, and W.T. Vetterling. *Numerical recipes*. Cambridge university press, 1987.

[54] J. R. Shewchuk. An introduction to the conjugate gradient method without the agonizing pain. Unpublished, 1994.

[55] G. Henkelman, B.P. Uberuaga, and H. Jonsson. A climbing image nudged elastic band method for finding saddle points and minimum energy paths. *Journal of chemicals physics*, 113:9901, 2000.

[56] G. Henkelman and H. Jonsson. Improved tangent estimate in the nudged elastic band method for finding minimum energy paths and saddle points. *Journal of chemicals physics*, 113:9978, 2000.

[57] R.S. Mulliken. Electronic population analysis on LCAOxMO molecular wave functions I. *Journal of Chemical Physics*, 23:1833, 1955.

[58] Felix Bloch. Über die quantenmechanik der elektronen in kristallgittern. *Physics and astronomy*, 52:555, 1928.

[59] J.P. Perdew, K. Burke, and Matthias Ernzerhof. Generalized gradient approximation made simple. *Physical Review Letters*, 77:3865, 1996.

[60] S.R. White. Density-matrix algorithms for quantum renormalization groups. *Physical review B*, 48:10345, 1993.

[61] H.J. Monkhorst and J.D. Pack. Special points for brillouin-zone integrations. *Physical review B*, 13:5188, 1976.

[62] M.J. Puska, S. Pöykkö, M. Pesola, and R. M. Nieminen. Convergence of supercell calculations for point defects in semiconductors: Vacancy in silicon. *Physical review B*, 58:1318, 1998.

[63] H. Marsh and I. A. Edwards. *Introduction to carbon science*. Butterworth Publishers, 1989.

[64] E. Fitzer, K. H. Kochling, H. P. Boehm, and H. Marsh. Recommended terminology for the description of carbon as a solid. *Pure and applied chemistry*, 67:473, 1995.

[65] R. E. Franklin. The structure of graphitic carbons. *Acta Cristallographica*, 4:253, 1951.

[66] R.E. Franklin. Crystallite growth in graphitizing and non-graphitizing carbons. *Proceeding of the royal society london A*, 209:196, 1951.

[67] P.J.F. Harris, A. Burian, and S. Duber. High-resolution electron microscopy of a microporous carbon. *Philosophical Magazine Letters*, 80:381, 2000.

[68] R.E. Franklin. A study of the fine structure of carbonaceous solids by measurements of true and apparent densities. part I. coals. *Transactions of the Faraday Society*, 45:274, 1949.

[69] C. Carroll, D. Berry, and C. Greenman. Colorado coal: energy security for the future. *Rocktalk*, 8:1, 2005.

[70] A. Oberlin. *Chemistry and physics of carbon vol. 22 p. 1*, volume 22. P.A. Thrower, 1989.

[71] L.L. Ban, D. Crawford, and H. Marsh. Lattice-resolution electron microscopy in structural studies of non-graphitising carbons from polyvinylidene chloride (PVDC). *Journal of Applied Crystallography*, 8:415, 1975.

[72] P.J. Harris. Structure of non-graphitising carbons. *International Materials Reviews*, 42:206, 1997.

[73] P.J.F. Harris and S.C. Tsang. High-resolution electron microscopy studies of non-graphitizing carbons. *Philosophical Magazine A*, 76:667, 1997.

[74] Z. Zhang, R. Brydson, Z. Aslam, S Reddy, A. Brown, A Westwood, and B. Rand. Investigating the structure of non-graphitising carbons using electron energy loss spectroscopy in the transmission electron microscope. *Carbon*, 49:5049, 2011.

[75] H. Marsh and F. Rodriguez-Reinoso. *Activated Carbon*. Oxford: Elsevier, 2006.

[76] H. Richter and J.B. Howard. Formation of polycyclic aromatic hydrocarbons and their growth to soot-a review of chemical reaction pathways. *Progress in Energy and Combustion Science*, 26:565, 2000.

[77] J.D. Brooks and G.H. Taylor. Formation of graphitizing carbon from the liquid phase. *Nature*, 206:297, 1965.

[78] M. Inhatowicz, P. Chiche, J. Deduit, S. Pregermain, and R. Tournant. Formation de la texture des cokes de houilles et de brais etudiee par solubilite et par microscopie. *Carbon*, 4:41, 1966.

[79] T. Edstrom and I.C. Lewis. Chemiscal structure and graphitization: x-ray diffraction studies of graphite derived from polynuclear aromatics. *Carbon*, 7:85, 1969.

[80] I.C. Lewis and L.S. Singer. Electron spin resonance of stable aromatic radical intermediates in pyrolysis. *Carbon*, 7:93, 1969.

[81] I.C. Lewis. Chemistry of carbonisation. *Carbon*, 20:519, 1982.

[82] S.E. Stein. Thermochemical kinetics of anthracene pyrolysis. *Carbon*, 19:621, 1981.

[83] A. Oberlin, G. Terriere, and J. L. Boulmier. Carbonification, carbonization and graphitization as studied by high resolution electron microscopy part i. *Tanso*, 80:29, 1975.

[84] A. Oberlin, G. Terriere, and J. L. Boulmier. Carbonification, carbonization and graphitization as studied by high resolution electron microscopy part ii. *Tanso*, 83:153, 1975.

[85] E.R. Vorpagel and J.G. Lawn. Most stable configurations of polynuclear aromatic hydrocarbon molecules in pitches via molecular modelling. *Carbon*, 30:1033, 1992.

[86] D. Auguie, M. Oberlin, A. Oberlin, and P. Hyvernat. Microtexture of mesophase spheres as studied by high resolution conventional transmission electron microscopy (ctem). *Carbon*, 18:337, 1980.

[87] N.H. Tinh, C. Destrade, and H. Gasparoux. Nematic disc-like liquid crystals. *Physics letters A*, 72:251, 1979.

[88] F.G. Emmerich. Evolutions with heat treatment of crystanillity in carbons. *Carbon*, 33:1709, 1995.

[89] S. Mrozowski. ESR of carbons in the transition range: Part I. *Carbon*, 17:227, 1979.

[90] C. R. Houska and B. E. Warren. X-ray study of the graphitization of carbon black. *Journal of Applied Physics*, 25:1503, 1954.

[91] J. Maire and J. Mering. S.c.i. conference carbon and graphite. In *p. 204*, 1957.

[92] P.A. Thrower. Editorial. *Carbon*, 44:699, 2006.

[93] D.B. Fischbach. *Chemistry and physics of carbon vol. 7 p. 1*. Marcel Dekker, New York, 1971.

[94] A. Ōya and S. Ōtani. Catalytic graphitization of carbons by various metals. *Carbon*, 17:131, 1979.

[95] A. Ōya and H. Marsh. Phenomena of catalytic graphitization. *Journal of material science*, 17:309, 1982.

[96] R.M. Bustin, J.N. Rouzaud, and J.V. Ross. Natural graphitization of anthracite: experimental considerations. *Carbon*, 33:679, 1995.

[97] T. Noda and M. Inagaki. Heat treatment of carbon under high pressure. *Nature*, 196:772, 1962.

[98] T. Noda and H. Kato. Heat treatment of carbon under high pressure. *Carbon*, 3:289, 1965.

[99] S. De Fonton, A. Oberlin, and M. Inagaki. Characterization by electron microscopy of carbon phases (intermediate turbostratic phase and graphite) in hard carbons when heat-treated under pressure. *Journal of material science*, 15:909, 1980.

[100] W.N. Reynolds. *Physical properties of graphite*. Elsevier, 1968.

[101] W. Friedrich, P. Knipping, and M. Laue. Interferenzerscheinungen bei röntgenstrahlen. *Annalen der Physik*, 346:971, 1913.

[102] W.H. Bragg and W.L. Bragg. The reflection of x-rays by crystals. *Proceeding of the royal society A*, 88:428, 1913.

[103] P. Scherrer. Bestimmung der größe und der inneren struktur von kolloidteilchen mittels röntgenstrahlen. *Göttinger Nachrichten*, 2:98, 1918.

[104] P.A. Thrower and D.C. Nagle. The importance of strain in crystallite size determinations in graphite. *Carbon*, 11:663, 1973.

[105] B.E. Warren and N.S. Gingrich. Fourier integral analysis of x-ray powder patterns. *Physical Review*, 46:368, 1934.

[106] B.E. Warren. X-ray diffraction study of carbon black. *The journal of chemical physics*, 2:551, 1934.

[107] R.E. Franklin. The interpretation of diffuse x-ray diagrams of carbon. *Acta crystallographica*, 3:107, 1950.

[108] B.E. Warren and P. Bodenstein. The diffraction pattern of fine particle carbon blacks. *Acta Cristallographica*, 18:282, 1965.

[109] A. R. Stokes and A. J. C. Wilson. A method of calculating the integral of the integral breadths of debye-scherrer lines. *Proceedings of the Cambridge philosophical society*, 38:313, 1942.

[110] G. E. Bacon. Unit-cell dimensions of graphite. *Acta Crystallography*, 3:137, 1950.

[111] A.R. Stokes. A numerical fourier-analysis method for the correction of widths and shapes of lines on x-ray powder photographs. *Proceeding of the physical society London*, 61:382, 1948.

[112] D.T. Keating and B.E. Warren. The effect of a low absorption coefficient on x-ray spectrometer measurements. *Review of scientific instruments*, 23:519, 1952.

[113] A. Bouraoui. Structures des carbones prégraphitiques: études des défauts et des distortions. *Bulletin de la societé francaise minéralogie et de cristallographie*, 88:633, 1965.

[114] A. Bouraoui and J. Mering. Diametre des couches atomiques élémentaires des carbones tendres traités entre 1000 et 2000°C. *Carbon*, 1:465, 1964.

[115] F. Tuinstra and J.L. Koenig. Raman spectrum of graphite. *Journal of chemicals physics*, 53:1126, 1970.

[116] C. Thomsen and S. Reich. Double resonant raman scattering in graphite. *Physical review letters*, 85:5214, 2000.

[117] R.J. Nemanich and S.A. Solin. Observation of an anomalously sharp feature in the 2nd order raman spectrum of graphite. *Solid State Coninunications*, 23:417, 1977.

[118] R.J. Nemanich and S.A. Solin. First- and second-order raman scattering from finite-size crystals of graphite. *Physical Review B*, 20:392, 1979.

[119] Y. Wand, D.C. Alsmeyer, and R.L. McCreer. Raman spectroscopy of carbon materials: structural basis of observed spectra. *Chemical Materials*, 2:557, 1990.

[120] S. Reich and C. Thomsen. Raman spectroscopy of graphite. *Philosophical Transactions: Mathematical, Physical and Engineering Sciences*, 362:2271, 2004.

[121] R.P. Vidano, D.B. Fischbach, L.J. Willis, and T. M. Loehr. Observation of raman band shifting with excitation wavelength for carbons and graphites. *Solid State Communications*, 39:341, 1981.

[122] M. Nakamizo, R. Kammereck, and P.L. Walker. Laser raman studies on carbons. *Carbon*, 12:259, 1974.

[123] A. Burian, P. Daniel, S. Duber, and J. Dore. Raman scattering studies of the graphitization process in anthracene- and saccharose-based carbons. *Philosophical Magazine B*, 81:525, 2001.

[124] A.C. Ferrari and J. Robertson. Interpretation of raman spectra of disordered and amorphous carbon. *Physical Review B*, 61:14095, 2000.

[125] P.L. Robin P.G. Rouxhet. Infrared study of the evolution of kerogens of different origins during catagenesis and pyrolysis. *Fuel*, 57:533, 1978.

[126] G.A. Zickler, B. Smarsly, N. Gierlinger, H. Peterlik, and O. Paris. A reconsideration of the relationship between the crystallite size L_a of carbons determined by x-ray diffraction and raman spectroscopy. *Carbon*, 44:3239, 2006.

[127] G.R. Millward and D.A. Jefferson. *Chemistry and physics of carbon vol. 14 p. 1*. Marcel Dekker, New York, 1978.

[128] J.N. Rouzaud and A. Oberlin. Structure, microtexture and optical properties of anthracene and saccharose based carbons. *Carbon*, 27:517, 1989.

[129] F. Bensaid and A. Oberlin. Characterization of some cokes from coking coals or blends. *Journal de chimie physique et de physico-chimie biologique*, 84:1457, 1987.

[130] M. Monthioux, M. Oberlin, A. Oberlin, and X. Bourrat. Heavy petroleum products: microtexture and ability to graphitize. *Carbon*, 20:167, 1982.

[131] A. Oberlin. Application to dark-field electron microscopy to carbon study. *Carbon*, 17:7, 1979.

[132] J. Goma and M. Oberlin. Graphitization of thin carbon films. *Thin solid films*, 65:221, 1980.

[133] P.I. Oden, T. Thundat, L.A. Nagahara, S.M. Lindsay, G.B. Adams, and O.F. Sankey. Superperiodic features observed on graphite under solution with scanning tunneling microscopy. *Surface science letters*, 254:L454, 1991.

[134] D.Q. Yang, G.X. Zhang, E. Sacher, M. José-Yacamán, and N. Elizondo. Evidence of the interaction of evaporated pt nanoparticles with variously treated surfaces of highly oriented pyrolytic graphite. *Journal of physical chemistry B*, 110:8348, 2006.

[135] Z.Y. Rong. Extended modifications of electronic structures caused by defects: Scanning tunneling microscopy of graphite. *Physical Review B*, 50:1839, 1994.

[136] J. Xhie, K. Sattler, M. Ge, and N. Venkateswaran. Giant and supergiant lattices on graphite. *Physical review B*, 47:15835, 1993.

[137] B.T. Kelly. *Physics of graphite*. Applied science, 1981.

[138] L.X. Benedict, l. Nasreen, G. Chopra, M.L. Cohen, A. Zettl, S.G. Louie, and V.H. Crespi. Microscopic determination of the interlayer binding energy in graphite. *Chemical Physics Letters*, 286:490, 1998.

[139] M.C. Schabel and J.L. Martins. Energetics of interplanar binding in graphite. *Physical review B*, 46:7185, 1992.

[140] G.E. Bacon. The intedayer spacing of graphite. *Acta crystallographica*, 4:558, 1951.

[141] J. Boone. Fortran program.

[142] B.T. Kelly. Irradiation damage in graphite due to fast neutrons in fision and fusion systems. Technical report, Nuclear power technology development section iternational atomic energy agency, 2000.

[143] J.C. Charlier, X. Gonze, and J.P. Michenaud. Graphite interplanar bonding: electronic delocalization and van der waals interaction. *Europhysics letters*, 28:403, 1994.

[144] J.M. Campanera, G. Savini, I. Suarez-Martinez, and M. I. Heggie. Density functional calculations on the intricacies of moiré patterns on graphite. *Physical review B*, 75:235449, 2007.

[145] L.G. Isaacs. Graphitization of organic compounds-I. enhanced graphitization by copyrolysis with aryne precursors. *Carbon*, 6:765, 1968.

[146] G.S. Waldo, R.M.K. Carison, J.M. Moldowanand K.E. Peters, and J.E. Penner-Hahn. Sulfur speciation in heavy petroleums: Information from x-ray absorption near-edge structure. *Geochimica andd Cosmochimica Acta*, 55:801, 1991.

[147] J. Gillot, B. Lux, P. Cornuault, and P.F Du Chaffaut. Changement de structure lors de la desulfuration de coke de petrole. *Carbon*, 6:389, 1968.

[148] K. Fujimoto, M. Sato, M. Yamada, R. Yamashita, and K. Shibata. Puffing inhibitors for coal tar based needle coke. *Carbon*, 24:397, 1986.

[149] Y. Sugimoto, F.J. Derbyshire, and A.W. Scaroni. The effect of sulfur evolution on the properties of high-temperature carbons-II: The addition of Fe_2O_3. *Carbon*, 23:417, 1985.

[150] M.P. Whittaker and L.I. Grindstaff. The irreversible expansion of carbon bodies during graphitization. *Carbon*, 7:615, 1969.

[151] K. Fujimoto, I. Mochida, Y. Todo, T. Oyama, R. Yamashita, and H. Marsh. Mechanism of puffing and the role of puffing inhibitors in the graphitization of electrodes from needle cokes. *Carbon*, 27:909, 1989.

[152] I. Mochida and H. Marsh. A mechanistic proposal on puffing of coke and its inhibition (in japanese). *Tanso*, 126:89, 1986.

[153] Y. Kawano, T. Fukuda, T. Kawarada, I Mochida, and Y. Korai. Mechanisms for puffing inhibition of coal tar based needle coke with disodium hydrogen phosphate (DHP) and boric acid. *Carbon*, 37:1725, 1999.

[154] J.J. Kipling, P.V. Shooter, and R.N. Young. The effect of sulphur on the graphitization of carbons derived from polyvinyl chloride-sulphur systems. *Carbon*, 4:333, 1966.

[155] N. Christu and E.Fitzer. *Journal de chimie physique*, Special edition, 1969.

[156] E. Fitzer and S. Weisenburger. Evidence of catalytic effect of sulphur on graphitization between 1400 and 2000°C. *Carbon*, 14:195, 1976.

[157] S.R. Brandtzaeg and H.A. Ōye. A possible mechanism of sulphur-induced graphitization. *Carbon*, 26:163, 1988.

[158] X. Bourrat, A. Oberlin, and J.C. Escalier. Sulphur behaviour during asphalt heat treatment. *Fuel*, 66:542, 1987.

[159] B. Meyer. Solid allotropes of sulfur. *Chemical reviews*, 64:429, 1964.

[160] B. Meyer. *Elemental Sulfur: Chemistry and Physics*. Interscience, 1965.

[161] S.J. Retting and J. Trotter. Refinement of the structure orthorhombic sulfur. *Acta Crystallography C*, 43:2260, 1987.

[162] C.A Coulson, M.A. Herraez, M. Leal, E. Santos, and S. Senent. Formation energy of vacancies in graphite. *Proceeding of the royal society London A*, 274:461, 1963.

[163] R.H. Telling, C.P. Ewels, A.A. El-Barbary, and M.I. Heggie. Wigner defects bridge the graphite gap. *Nature materials*, 2:333, 2003.

[164] S. Bonnamy. Carbonization of various precursors. effect of heating rate part ii: Transmission electron microscopy and physicochemical studies. *Carbon*, 37:1707, 1999.

[165] M. Fujita, K. Wakabayashi, K. Nakada, and K. Kusakabe. Peculiar localized state at zigzag graphite edge. *Journal of athe physical society of Japan*, 65:1920, 1996.

[166] A. Zobelli, V. Ivanovskaya, P. Wagner, I. Suarez-Martinez, A. Yaya, and C.P. Ewels. A comparative study of density functional and density functional tight binding calculations of defects in graphene. *Physica Statu Solidi B*, 249:276, 2012.

[167] S.E. Stein and R.L. Brown. π-electron properties of large condensed polyaromatic hydrocarbons. *Journal of American chemical society*, 109:3721, 1987.

[168] L.R. Radovic and B. Bockrath. On the chemical nature of graphene edges: origin of stability and potential for magnetism in carbon materials. *Journal of american chemical society*, 127:5917, 2005.

[169] P. Koskinen, S. Malola, and H. Hakkinen. Self-passivating edge reconstructions of graphene. *Physical review letters*, 101:115502, 2008.

[170] E. Prada, P. San-Jose, and L. Brey. Zero landau level in folded graphene nanoribbons. *Physical Review Letters*, 105:106802, 2010.

[171] H.V. Roy, C. Kallinger, and K. Sattler. Study of single and multiple foldings of graphitic sheets. *Surface science*, 407:1, 1998.

[172] V. Ivanovskaya, A. Zobelli, P. Wagner, M.I. Heggie, P.R. Briddon, M.J. Rayson, and C.P. Ewels. Low-energy termination of graphene edges via the formation of narrow nanotubes. *Physical Review Letters*, 107:065502, 2011.

[173] P.A. Ouseph. Observation of prismatic dislocation loops in graphite by scanning tunneling microscope. *Physica Statu Solidi A*, 169:25, 1998.

[174] I.M. Dawson and E.A.C. Follet. An electron microscope study of synthetic graphite. *Proceedings of the Royal Society of London. Series A*, 253:390, 1959.

[175] E. Fitzer, K. Mtiller, and W. Schafer. The effect of sulphur on the pyrolysis behavior of pitch. *Carbon*, 11:675, 1973.

[176] I.C. Lewis and R.A. Greinke. Polymerization of aromatic hydrocarbons with sulfur. *Journal of polymer science*, 20:1119, 1982.

[177] W.H. Calkins. Investigation of organic sulfur-containing structures in coal by flash pyrolysis experiments. *Energy and fuels*, 1:59, 1987.

[178] L .V. Gurvich, I.V. Veyts, and C.B. Alcock. *Thermodynamic Properties of Individual Substances vol 2*. Hemisphere Publishing Corp.: New York, 1982.

[179] R.H. Telling and M.I. Heggie. Radiation defects in graphite. *Philosophical Magazine*, 87:4797, 2007.

[180] M.I. Heggie, B.R. Eggen, C.P. Ewels, G. Jungnickel, R. Jones, and P.R. Briddon. LDA calculations of points defects in graphites and fullurenes. *Electrochemical Society Proceeding*, 98:60, 1997.

[181] C.D. Latham. Private discussion. 2012.

[182] J.P. Goss, P.R. Briddon, V.K. Nagareddy, N.G. Wright, A.B. Horsfall, J.D. Caldwell, D.K. Gaskill, and G.G. Jernigan. Influence of intercalated silicon on the transport properties of graphene. *Materials Science Forum*, 679:793, 2011.

[183] J.P. Goss, R.J. Eyre, and P.R. Briddon. Bound substitutional impurity pairs in diamond: a density functional study. *Journal of physics: condensed matter*, 20:085217, 2008.

[184] N.J. Morrison and M. Porter. Temperature effects on the stability of intermediate and crosslinks in sulfur vulcanization. *Rubber chemistry and technology*, 57:63, 1984.

[185] Z. Liu, K. Suenaga, P.J.F. Harris, and S. Iijima. Open and closed edges of graphene layers. *Physical review letters*, 102:015501, 2009.

[186] P.W. Atkins. *Physical Chemistry*. Oxford University press, 1978.

[187] I. Suarez-Martinez, G. Savini, G. Haffenden, J.-M. Campanera, and M. I. Heggie. Dislocations of burgers vector c/2 in graphite. *Physica Statu Solidi C*, 4:2958, 2007.

[188] J.A. Turnbull, M.S. Stagg, and W.T. Eeles. Annealing studies of boron-doped graphite by electron microscopy and x-ray diffusion. *Carbon*, 3:387, 1966.

[189] W. Rudorff. Graphite intercalation compounds. *Advances in inorganic chemistry*, 1:223, 1959.

[190] G.R. Hennig. *Progress in inorganic chemistry,*. Interscience, 1959.

[191] http://www.world-nuclear.org.

[192] J.E. Brocklehurst, B.T. Kelly, and K. Gilchrist. *Chemistry and Physics of carbon, Vol. 17, p. 175*. Marcel Decker, 1981.

[193] A. Ōya, R. Yamashita, and S. Otani. Catalytic graphitization of carbons by borons. *Fuel*, 58:495, 1979.

[194] H.N. Murty, D.L. Biederman, and E.A Heintz. Apparent catalysis of graphitization.3. effect of boron. *Fuel*, 56:305, 1977.

[195] W.V. Kotlensky. Effect of boron level on graphitization of BPG. *Carbon*, 5:409, 1967.

[196] R.B. Trask. Effect of boron addition on some properties of synthetic graphites. *Fuel*, 47:397, 1968.

[197] T. Hagio, M. Nakamiso, and K. Kobayashi. Thermal conductivities and raman spectra of boron-doped carbon materials. *Carbon*, 25:637, 1987.

[198] G.R. Hennig. Electron microscopy of graphite containing boron. *Journal of applied physics*, 34:237, 1963.

[199] R.M. Mayer. Large interstitial loops in graphite containing boron. *British journal of applied physics*, 17:431, 1966.

[200] P.A. Thrower. *Chemistry and physics of Carbon Vol. 5 p. 217*. Marcel Dekker, New York, 1969.

[201] A. Kelly and R.M. Mayer. The influence of boron on the clustering of radiation damage in graphite-i. electron microscopic observations. *Philosophical Magazine*, 19:701, 1969.

[202] L.M. Brown, A. Kelly, and R.M. Mayer. The influence of boron on the clustering of radiation damage in graphite-ii. Nucletaion of interstitials loops. *Philosophical Magazine*, 19:721, 1969.

[203] D.E. Soule and C.W. Nezbeda. Direct basal-plane shear in single-crystal graphite. *Journal of applied physics*, 39:5122, 1968.

[204] K. Komatsu. Theory of the specific heat of graphite theory. *Journal of the physical society of Japan*, 10:346, 1955.

[205] R. Nicklow, N. Wakabayashi, and H.G. Smith. Lattice dynamics of pyrolytic graphite. *Physical review B*, 5:4951, 1972.

[206] O.L. Blakslee, D.G. Protoctor, E.J. Seldin, G.B. Spence, and T. Weng. Elastic constants of compression-annealed pyrolytic graphite. *Journal of applied physics*, 41:3373, 1970.

[207] R.H. Telling and M.I. Heggie. Stacking fault and dislocation glide on the basal plane of graphite. *Philosophical Magazine*, 83:411, 2003.

[208] M.I. Heggie. Private communications. 2010.

[209] G. Savini, Y.J. Dappe, S. Oberg, J.C. Charlier, M.I. Katsnelson, and A. Fasolino. Bending modes, elastic constants and mechanical stability of graphitic systems. *Carbon*, 49:62, 2011.

[210] E.J. Seldin and C.W. Nezbeda. Elastic constants and electron-microscope observations of neutron-irradiated compression-annealed pyrolytic and single-crystal graphite. *Journal of applied physics*, 41:3389, 1970.

[211] C.E. Lowell. Solid solution of boron in graphite. *Journal of american ceramic society*, 50:142, 1967.

[212] P. Wagner and J.M Dickinson. Ambient and high temperature expereiment on boron-doped polycrystalline graphites. *Carbon*, 8:313, 1970.

[213] T. Hagio, M. Nakamiso, and K. Kobayashi. Studies on x-ray diffraction and raman spectra of B-doped natural graphite. *Carbon*, 27:259, 1989.

[214] G.R. Hennig. Diffusion of boron in graphite. *The journal of chemical physics*, 42:1167, 1965.

[215] I. Suarez-Martinez, A.A. El-Barbary, G. Savini, and M.I. Heggie. First-principles simulations of boron diffusion in graphite. *Physical review letters*, 98:015501, 2007.

[216] M.A. Kanter. Diffusion of carbon atoms in natural graphite crystals. *Physical Review*, 107:655, 1957.

[217] F.S. Feates. The diffusion of carbon in single crystal graphite. *Journal of nuclear materials*, 27:325, 1968.

[218] J. Kouvetakis, R.B. Kaner, M.L. Sattler, and N. Bartlett. A novel graphite-like material of composition BC_3, and nitrogen-carbon graphites. *Journal of chemicals society, chemical communications*, 24:1758, 1986.

[219] D. Tomanek, R.M. Wentzcovitch, S.G. Louie, and M.L. Cohen. Calculation of electronic and structural properties of BC_3. *Physical review B*, 37:3134, 1988.

[220] L.E. Jones and P.A. Thrower. The influence of structure on substitutional doping: SIMS analysis of boron doped pyrolytic graphites. *Carbon*, 28:239, 1990.

[221] L.E. Jones and P.A. Thrower. Influence of boron on carbon fiber microstructure, physical properties and oxidation behaviour. *Carbon*, 29:251, 1991.

[222] P. Delhaes and A. Marchand. Proprietes electroniques d'un coke de brai dope au bore. *Carbon*, 3:115, 1965.

[223] B.J.C. Van Der Hoeven, P.H. Keesom, J.W. McClurk, and G. Wagoner. Low-temperature specific heat and density of states of boronated graphite. *Physical review*, 152:796, 1966.

[224] C.D. Latham, M.I. Heggie, J.A. Gamez, I. Suarez-MartÄśnez, C.P. Ewels, and P.R. Briddon. The di-interstitial in graphite. *Journal of physics: condensed matter*, 20:395220, 2008.

[225] M.I. Heggie, I. Suarez-Martinez, C. Davidson, and G. Haffenden. Buckle, ruck and tuck: A proposed new model for the response of graphite to neutron irradiation. *Journal of nuclear materials*, 4:0115, 2011.

[226] M. Endo, C. Kim, T. Karaki, T. Tamaki, Y. Nishimura, M.J. Matthews, S.D.M. Brown, and M.S. Dresselhaus. Structural analysis of the B-doped mesophase pitch-based graphite fibers by Raman spectroscopy. *Physical review B*, 58:8991, 1998.

[227] T. Shirasaki, A. Derre, M. Menetrier, A. Tressaud, and S. Flandrois. Synthesis and characterization of boron-substituted carbons. *Carbon*, 38:1461, 2000.

[228] L. Vegard. Die konstitution der mischkristalle und die raumfüllung der atome. *Zeitschrift für Physik*, 5:17, 1921.

[229] P.R. Wallace. The band theory of graphite. *Physical Review*, 71:622, 1947.

[230] C.A. Coulson. Energy bands in graphite. *Nature*, 159:265, 1947.

[231] J.C Slonczewsky and P.R. Weiss. Band structure of graphite. *Physical review*, 109:401, 1958.

[232] J.W. McClure. Theory of diamagnetism in graphite. *Physical review*, 119:606, 1960.

[233] A. Marchand. *Chemistry and physics of carbon vol. 7 p. 155*. Marcel Dekker, New York, 1971.

[234] A. Marchand and J.V. Zanchetta. Proprietes electroniques d'un carbone dope a l'azote. *Carbon*, 3:483, 1966.

[235] C.P. Ewels and M. Glerup. Nitrogen doping in carbon nanotubes. *Journal of nanoscience and nanotechnology*, 5:1345, 2005.

[236] J.C. Charlier, X. Gonze, and J.P. Michenaud. First principle study of the electronic properties of graphite. *Physical Review B*, 43:4579, 1991.

[237] L.J. Sham and M. Schlüter. Density-functional theory of the energy band gap. *Physical review letters*, 51:1888, 1983.

[238] P. Delhaes and A. Marchand. Proprietes electroniques d'un graphite polycristallin dope au bor. *Carbon*, 3:125, 1965.